

Dissertation
submitted to the
Combined Faculties for the Natural Sciences and for Mathematics
of the Ruperto-Carola-University of Heidelberg, Germany
for the degree of
Doctor of Natural Sciences

Put forward by
Shuang Gao
born in: Beijing, China
Oral examination: 26th October, 2011

Empirical Models of the Milky Way at the North Galactic Pole based on SDSS Photometric Data

Referees: Prof. Dr. E. K. Grebel
Priv.-Doz. Dr. A. Just

Abstract

This thesis aims at comparisons between several Galactic models and photometric data from the Sloan Digital Sky Survey (SDSS) at the north galactic cap. The data are selected from the SDSS DR7 catalogue using the de-reddened magnitudes. The mean color-magnitude ridgelines of different globular clusters are used as fiducial isochrones and compared to model stellar population sequences on color-magnitude diagrams (CMDs). The galactic models used in this work are the Just-Jahreiß, TRILEGAL, and Besançon models. These are described in detail and used in order to reproduce the stellar contents with three components which are compared with SDSS star counts in Hess diagrams and luminosity functions.

The Just-Jahreiß model adopts a set of continuous sub-populations of the thin disk to reproduce the best Hess diagram of the observed stellar distribution. The CMDs of the Just-Jahreiß model are based on the empirical main sequence derived from nearby stars. The largest discrepancy is located at the transition between the thin and thick disks. The corresponding star formation rate (SFR) and age-velocity dispersion relation (AVR) are estimated from the best “model A”. And the local calibration is normalized by SDSS star counts. The high latitude ring fields and a low latitude stripe are tested using the Just-Jahreiß model, the discrepancies increase along with the decreasing latitudes. The best scale length pair of the disks is found by the fits in the Hess diagrams of the NGP and 24 smaller ring fields.

With TRILEGAL reproduce the stellar content using the default and three other input sets which are determined from the Just-Jahreiß, Besançon, and Jurić models parameters. An optimization of the four sets is presented as a new input set.

The Besançon model is analyzed using multi-color isochrones, luminosity functions and Hess diagrams. The positions and the numerical fraction of giants produced by the Besançon model are indicated on multi-color Hess diagrams. The isochrones for the thick disk and halo of the TRILEGAL and Besançon models are tested by the observed star cluster fiducial isochrones from SDSS.

The qualities of the fit in the Hess diagrams of the Just-Jahreiß, TRILEGAL, and Besançon models are 5%, 30%, and 50%, respectively.

These comparisons result in three main findings: 1) The essential discrepancies are caused by the structures of disks. 2) The luminosity functions are insensitive to the structures of disks. The discrepancies reflected on Hess diagrams cannot be presented on luminosity functions. 3) The isochrones of the thick disk and halo show the significant color offsets (at least for the Besançon model).

Zusammenfassung

In dieser Doktorarbeit werden verschiedene galaktische Modelle mit photometrischen Daten vom Sloan Digital Sky Survey (SDSS) um den nördlichen galaktischen Pol verglichen. Die genutzten farbkorrigierten Magnituden entstammen dem SDSS DR7 Katalog. Der beste Fit der Farb-Helligkeits-Diagramme (FHD) verschiedener Kugelsternhaufen werden als passende Isochrone genutzt und mit stellaren Populationsmodellen verglichen. Die galaktischen Modelle, welche in dieser Arbeit genutzt werden, sind das Just-Jahreiß, das TRILEGAL und das Besançon Modell. Diese werden im Detail erläutert und genutzt um den stellaren Bestand mit drei Bestandteilen zu reproduzieren sowie mit SDSS Sternzählungen in Hess Diagrammen und Leuchtkraftfunktionen zu vergleichen.

Das Just-Jahreiß Modell nimmt einen Satz von kontinuierlichen Unterpopulationen der dünnen Scheibe an um das beste Hess Diagramm der beobachteten Sternverteilung zu reproduzieren. Die FHDs des Just-Jahreiß Modells basieren auf der empirischen Hauptreihe von nahen Sternen. Dabei findet sich die größte Diskrepanz zwischen Model und Beobachtungen im Übergang von der dünnen zur dicken Scheibe. Die dazu passende Sternentstehungsrate und Alters-Geschwindigkeitsdispersions-Relation

werden im besten "Model A" bestimmt. Die lokale Kalibration wird mit SDSS Sternzählungen normalisiert. Ringförmige Felder in hohen Breitengraden und Streifen in niedriger Breite werden mit dem Just-Jahreiß Modell getestet. Die Unterschiede werden mit abnehmender Breite größer. Das beste Skalenlängenpaar der Scheibe wird gefunden, wenn die Hess Diagramme des nördlichen Pols mit 24 kleineren Ringfeldern gefittet werden.

TRILEGAL reproduziert den stellaren Inhalt mit dem ursprünglichen, sowie mit drei anderen Sätzen von Eingaben, welche aus den Just-Jahreiß, dem Besançon, sowie dem Jurić Modell Parametern bestimmt werden. Die Optimierung der vier verschiedenen Parametersätze wird als neuer Satz genutzt.

Das Besançon Modell wird analysiert mit Hilfe von Isochronen verschiedener Farbe, Helligkeitsfunktionen und mit Hess Diagrammen. Die Position und der numerische Anteil an Riesensternen, welche vom Besancon Model produziert werden, werden in einem mehrfarbigen Hess Diagramm gezeigt. Die Isochronen der dicken Scheibe und des Halo vom TRILEGAL wie auch vom Besancon Modell werden mit den Isochronen von beobachteten Sterenhaufen getestet.

Die Qualität des Fits im Hess Diagramm des Just-Jahreiß, des TRILEGAL, sowie des Besançon Models ist 5%, 30% und 50%.

Aus diesen Vergleichen ergeben sich drei hauptsächliche Resultate: 1) Die wichtigsten Unterschiede werden durch die Struktur der Scheibe verursacht. 2) Die Helligkeitsfunktionen sind insensitive in Bezug auf die Struktur der Scheibe. Die Unterschiede in den Hess Diagrammen werden von den Helligkeitsfunktionen nicht wieder gegeben. 3) Die Isochronen der dicken Scheibe und des Halo zeigen signifikante Farbunterschiede (zumindest für das Besançon Modell).

献给我的妻子李淳女士：

她对未来的理想、对真实的追求、对简单的信奉，弥足珍贵。

Contents

1	Introduction	1
1.1	Why model the Milky Way?	1
1.2	Observational data	2
1.3	Galactic Models	3
1.3.1	Stellar contents	3
1.3.2	Star counts and coordinate frame	5
1.3.3	Stellar population synthesis models	9
1.3.4	A self-consistent local disk model	10
1.4	Comparisons of models	10
1.5	Motivation for this thesis	12
2	Data	15
2.1	Stars	15
2.1.1	Photometry and selection	15
2.1.2	Spatial distribution	16
2.1.3	Hess diagram and luminosity function	17
2.2	Globular clusters	18
2.2.1	Photometry	18
2.2.2	Parameters	18
2.2.3	The isochrones of clusters	20
2.3	DR7 and DR8	21
3	Models	31
3.1	Just-Jahreiß model	31
3.1.1	Isothermal sub-population	31
3.1.2	Constraints of kinematics	34
3.1.3	Density profile and metallicity	34
3.2	TRILEGAL	35
3.2.1	Input sets	36
3.2.2	Interface and procedure	38
3.2.3	Calibration and output	38
3.3	Besançon model	40
3.3.1	Internal properties	40
3.3.2	Options	42
3.4	Jurić model	43
4	The local Just-Jahreiß model at the NGP field	49
4.1	Local models	49
4.1.1	Thin disk	49
4.1.2	Thick disk	50
4.1.3	Halo profile	50

4.2	Simulation of the NGP field	51
4.3	Fitting process	51
4.3.1	Local normalization	51
4.3.2	Algorithm	52
4.4	Comparisons and results	52
4.4.1	SFR and AVR	54
4.4.2	Smoothing and filter conversion	54
5	Simulations of TRILEGAL	61
5.1	Default (Set 1)	64
5.2	Fitting of Set 2, Set 3, and Set 4	65
5.2.1	Just-Jahreiß input (Set 2)	65
5.2.2	Besançon input (Set 3)	66
5.2.3	Jurić input (Set 4)	67
5.3	Optimizing (Set 5)	68
5.3.1	Halo fitting	68
5.3.2	Thick disk fitting	69
5.3.3	Thin disk choice	69
5.3.4	Model properties	70
6	Multi-color tests of the Besançon model	87
6.1	Multi-color simulations	87
6.1.1	Photometric conversions	88
6.2	Isochrones	89
6.3	Luminosity function and Hess diagram analysis	90
6.3.1	Luminosity function	90
6.3.2	Hess diagrams	91
6.4	Giants	92
7	The lower latitude fields	101
7.1	The field selection	101
7.2	The scale lengths	103
7.3	Hess diagrams	103
7.3.1	The ring fields	105
7.3.2	The stripe 110	105
8	Summary and outlook	117
8.1	Methods	117
8.1.1	The data selection	117
8.1.2	Transformations	118
8.1.3	Fits for the TRILEGAL model	118
8.1.4	The isochrones	119
8.1.5	The luminosity functions and Hess diagrams	119

8.2	Main results	120
8.2.1	The Just-Jahreiß model	120
8.2.2	The TRILEGAL model	122
8.2.3	The Besançon model	124
8.2.4	The lower latitude fields	125
8.3	Conclusion and Outlook	126
Bibliography		127
Acknowledgements		133

List of Figures

2.1	The response curves of the five filters of SDSS	17
2.2	The relative spatial distribution of our sample at the NGP field	23
2.3	The extinction map at the NGP field	24
2.4	The scheme of box size in Hess diagrams	25
2.5	Hess diagram of four fields from SDSS DR7	26
2.6	De-reddened g magnitude distribution of the NGP field	27
2.7	The fiducial isochrones of globular clusters	28
2.8	Hess diagrams of DR7 and DR8 at the NGP	29
2.9	The distributions of differences of g and $g - r$ in DR7 and DR8	30
2.10	The photometric error in the g band comparison of DR8 and DR7	30
3.6	Simulated image of the Milky Way	41
3.1	The surface SFRs and AVR of the Just-Jahreiß A, B, C, and D models	45
3.2	Snapshot images of interface and submitted result of the TRILEGAL interface	46
3.3	The magnitude distribution of the CDFS in the V band	46
3.4	The magnitude distribution of the DMS field 21 in the V band	47
3.5	The magnitude distributions of the SGP field in the B, V bands	47
4.1	The comparison between thick disk and halo of the Just-Jahreiß model and fiducial isochrones	55
4.2	A schematic diagram to indicate the radial direction and unit volume	56
4.3	The comparison of the Just-Jahreiß models A, B, C, and D	57
4.4	Hess diagrams and the comparison between SDSS observations and the best- fitting Just-Jahreiß model	58
4.5	The luminosity function of the Just-Jahreiß model	59
4.6	Hess diagrams of different smoothing size in the g band magnitude	60
4.7	The relative differences between models with three different transformations and Hess diagrams	60
5.1	The vertical density profiles of thick disk and halo of TRILEGAL	71
5.2	The isochrones of thick disk and halo of the TRILEGAL model	72
5.3	The magnitude distribution of the TRILEGAL model	73
5.4	Continuation of Figure 5.3	74
5.5	Hess diagrams of the TRILEGAL model for Set 1	75
5.6	Same as Figure 5.5 but for Set 2.	76
5.7	Same as Figure 5.5 but for Set 3.	77
5.8	Same as Figure 5.5 but for Set 4.	78
5.9	The χ^2 diagrams of the Hess diagrams of the models and the SDSS observations	79
5.10	The scale height of each age bin of the Besançon model	80
5.11	A schematic diagram of the CMD illustrating the distinction between thin and thick disk and halo stars	81
5.12	Hess diagram of thick disk and halo of Set 5 of the TRILEGAL model	82

5.13	Hess diagram of Set 5 of the TRILEGAL model	83
5.14	The χ^2 distribution of the Set 5 and the SDSS observations	84
5.15	Same as Figure 5.3 but for Set 5.	85
6.1	The color-absolute magnitude diagrams of thick disk and halo and the fiducial isochrones of globular clusters	94
6.2	The distributions of apparent magnitude of the Besançon model	95
6.3	Hess diagrams of the Besançon model in $(u - g, g)$	96
6.4	Same as Figure 6.3 but as $(g - r, g)$ diagram.	97
6.5	Same as Figure 6.3 but as $(r - i, r)$ diagram.	98
6.6	Same as Figure 6.3 but as $(i - z, i)$ diagram.	99
6.7	Hess diagrams of giants simulated by the Besançon model and the relative ratio to all stars.	100
7.1	The total χ^2 distribution of with the best fit of northern Galactic cap fields . .	104
7.2	The Hess diagrams of the SDSS data for the 12 small fields between $b = 70^\circ$ and 80°	106
7.3	The Hess diagrams of the SDSS data for the 12 small fields between $b = 60^\circ$ and 70°	107
7.4	The Hess diagrams of the Just-Jahreiß model for the 12 small fields between $b = 70^\circ$ and 80°	108
7.5	The Hess diagrams of the Just-Jahreiß model for the 12 small fields between $b = 60^\circ$ and 70°	109
7.6	The Hess diagrams of the relative differences between the data and model for the 24 small fields	110
7.7	The continued Hess diagrams of the relative differences between the data and model for the 24 small fields	111
7.8	The extinction map based on Schlegel et al. (1998) at the low latitude and $l = 110^\circ$ field	112
7.9	The Hess diagrams of the SDSS data, Just-Jahreiß models, and the relative differences between models and the data for the low-latitude fields	115
7.10	The Hess diagrams of three components of stripe 110	116

List of Tables

2.1	The central wavelengths, the full width at half maximum (FWHM) and magnitude limits of five filters used for SDSS photometry	16
2.2	Properties of globular clusters used for fiducial isochrones	19
2.3	Extinction parameters of different bands of the SDSS system.	20
3.1	Parameters of the Just-Jahreiß model A.	33
3.2	Header information of an output file of TRILEGAL.	40
3.3	Header information of an output file of Besançon.	43
4.1	Parameters of the best-fitting Just-Jahreiß model	53
5.1	The central Galactic coordinates of 37 selected fields simulated using TRILEGAL for comparison with SDSS observations.	62
5.2	The sets of input parameters in TRILEGAL and the χ^2 values of the Hess diagram comparisons.	63
5.3	The fit results of the thin disk sub-populations in the Besançon model.	67
6.1	Properties of the observed and simulated CMDs.	88
6.2	The polynomial coefficients of the transformation in the u band	89
6.3	The coefficients of transformation in $griz$ band	89
7.1	The low latitude fields selected for the test of the Just-Jahreiß model	102
8.1	The comparisons between the basic parameters of the Just-Jahreiß, TRILEGAL, and Besançon models	121

“It is always useful to remember that science is not designed to produce absolute knowledge, eternally true once found; for the most part it simply pushes back the frontier of that vast realm called ignorance.”

Jake Page

1

Introduction

1.1 Why model the Milky Way?

The Milky Way is a galaxy that can be studied by the most detailed observations. The Milky Way has been one of the most interesting study targets. Since Herschel’s stellar map had been published, the structure and evolution of the Galaxy had become one of the most important issues in astronomy. While we have meanwhile obtained an unprecedentedly detailed knowledge of our galaxy, we still lack an in-depth understanding of its basic constituents. So far there is no a reliable model of the Milky Way. Neither the contribution of the smooth background of the stellar components in the Galaxy has been grasped very well, nor do we understand satellite galaxies and the stellar accretion streams discovered in the last decades. The formation and evolution of galaxies is one of the great outstanding problems of astrophysics and this problem still seems far from a solution today (Weinberg 1977).

It is a traditional method to study a galaxy by modeling its stellar populations. Star counts (including the density profile and the luminosity function), kinematics, abundance, star formation, and dynamics can be modeled by different empirical laws. It is an important step to describe complex stellar contents using relatively simple mathematical tools in astronomy. Focusing on the Milky Way, we have more observation supports than other galaxies. Star counts have been primary way since William Herschel and John Herschel. After that, Kapteyn & van Rhijn (1920, 1922), Bok & Connolly (1954), Bok (1956), and Oort (1952) studied the Galactic structure using stars counts. Lacks of reliable observations and extinction knowledge led to the failure of modeling. However, the method and the recognition of extinction problems improved in these attempts.

Schmidt (1956) and Caldwell & Ostriker (1981) provided the earliest mass models that predicted and compared the kinematically measurable parameters, such as Oort constants and total surface density at the solar neighborhood. Dehnen & Binney (1998) gave one of the most important mass models of the Milky Way. The Galaxy is divided into halo, bulge, and 3 disks with own density distributions determined by surface photometric law of galaxies. This model is constrained by the Oort constants, local surface density and the Galactic rotational curve. These models gave us the opportunities to study the Galaxy using a comprehensive perspective with all (or most) of the observational constraints.

The validity and accuracy of different models of a galaxy are always controversial, because they describe a smooth material background (field stars, dark matter and gas following smooth

distribution laws) in the halo or the disks. Initially the model building is not to focus on a perfect model that can reproduce a galaxy in every respect. A useful tool is provided to produce stars (or dark matter and gas) to calculate the possible contents of a large data set, therefore, to test the data to answer questions about galaxy structure and evolution and to test some theoretical or empirical laws, such as the initial mass function (IMF), star formation history (SFH), or age-velocity relation (AVR). That means we are expecting to obtain a “star generator” that can be compared with observations and to determine the structural parameters like the vertical and radial scalelengths accurately .

1.2 Observational data

Over the last decade, more and more photometric or spectroscopic surveys have focused on Galactic structure (cf. Weinberg (2004), Newberg et al. (2004), Smith et al. (2006), and Sesar et al. (2011)). These surveys have provided or are providing powerful tools to study our Galaxy by combining observations and theoretical models of stellar densities, kinematics, abundances, and population evolution. These excellent databases make detailed Galactic studies possible today.

The Hipparcos as ESA’s space astrometry mission, launched in 1989 and successfully observed the celestial sphere for 3.5 years. Two tasks were finished by the Hipparcos: the Hipparcos Catalogue of 118,218 stars charted with the higher precision, and the Tycho Catalogue of one million stars with lower precision. After further processing, the Tycho-2 Catalogue of 2.5 million stars was published in 2000, which includes 99% of all stars down to 11 mag. Regarding deep photometric surveys, the Two Micron All Sky Survey (2MASS) was completed almost a decade ago and the full data release took place in 2003. The limiting magnitudes in the J , H and K_s bands of the point-source catalog are 16, 15 and 14.7 mag, respectively, which are almost five magnitudes deeper than any comparable infrared survey (Skrutskie et al. 2006). Covering the wavelength range from the ultraviolet to the near-infrared, the Sloan Digital Sky Survey (SDSS, York et al. 2000; Gunn et al. 1998; Stoughton et al. 2002) has reached even deeper limiting magnitudes in the northern sky in five bands u , g , r , i , z . The Data Release 7 (DR7) of the SDSS provides a database covering 11,663 square degrees of the sky containing over 350 million objects including 127 million stars (Abazajian et al. 2009). The observations by the SDSS make it possible to investigate star distributions across more than one quarter of the sky going down as faint as ~ 22 mag. The Panoramic Survey Telescope and Rapid Response System (Pan-STARRS) is a photometric multi-color imaging survey that will ultimately reach slightly fainter magnitudes than the SDSS and cover three quarters of the sky. Pan-STARRS (Kaiser & Pan-STARRS Team 2002) also adds the time domain through repeated observations and recently started regular scientific observations.

On the other hand, spectroscopic surveys play a more and more important role in Galactic astronomy. The original SDSS obtained 225,000 stellar spectra. The Sloan Extension for Galactic Understanding and Exploration (SEGUE and SEGUE-II), survey projects that are part of SDSS-II and SDSS-III, additionally obtained spectra of 354,000 stars in order to create a more detailed three-dimensional map of the Milky Way. Several pipelines (Lee et al. 2008a,b;

Allende Prieto et al. 2008; Smolinski et al. 2011; Lee et al. 2011) are used to determine stellar parameters, such as effective temperature, surface gravity, metallicity, and radial velocity. Another spectroscopic survey project is the RAdial Velocity Experiment (RAVE) carried out with the 1.2-m UK Schmidt Telescope at the Australian Astronomical Observatory (Steinmetz et al. 2006). The final RAVE database is expected to contain the radial velocities and stellar parameters of 1.0 million stars until the end of 2012. RAVE focusses only on rather bright stars ($9 < I < 13$). The third data release (DR3) was published very recently and includes more than 83,072 stars with radial velocities. About 95% of the line-of-sight velocities have uncertainties better than 5 km s^{-1} (Siebert et al. 2011). The Large Sky Area Multi-Object Fiber Spectroscopy Telescope (LAMOST, Chu & Zhao 1998, named *Guoshoujing* Telescope recently) of China, which is expected to enter into regular operations in 2011, can gather stellar spectra using 4,000 fibers in each exposure. The combination of a 4.0-m Schmidt telescope and 4,000 fibers will ensure maximum efficiency in obtaining stellar spectra and parameters.

Finally, the astrometric, photometric, and spectroscopic satellite Gaia, a cornerstone mission of the European Space Agency (ESA) (Gilmore et al. 2000), will be launched in early 2013. It will provide distances and proper motions of up to one billion stars to a limiting magnitude of $M_V=20$ mag. For 180 million stars brighter than $M_V=17$ mag radial velocities and stellar parameters will be measured (Jordan 2008). Since the proposal was presented in 1993, the Gaia mission has entered the last phase before the launch (Lindgren 2010). The average root mean square (rms) errors of astrometric parameters (parallax, proper motion, and position) are estimated for the future data processing. The overall data volume that will be retrieved from the spacecraft during the 5-year mission. About 200 TB of usable uncompressed data on the ground with astrometric parameters of stars in the Milky Way will be administered and processed by the Data Processing and Analysis Consortium (DPAC).

Gaia is the continuation of a series of past or ongoing galactic survey projects, which are able to obtain large amount of high-quality photometric and spectroscopic data. The SDSS and the LAMOST as the examples to achieve the high efficiency of detection methods, provide us with the opportunity to further explore the nature of the stellar contents of the Milky Way again. Besides these ongoing projects, Gaia is finishing its final preparations for the launch in 2013 and then would stimulate new interest on the Milky Way (Bailer-Jones 2009).

1.3 Galactic Models

1.3.1 Stellar contents

Today the picture of two disks, a halo, and a bulge of the Milky Way is accepted widely. The bulge won't be considered in this work for local structures that point the high Galactic latitudes.

The thin disk has complex density and potential profiles caused by a mixture of sub-populations and their velocity dispersions. In the classical models the vertical form of the thin disk is assumed to be an exponential or hyperbolic secant function of height above the Galactic plane and the Galactocentric distance to approximate the sum of a set of multiplex sub-populations. Bahcall (1984a,b) first mentioned and studied a finite set of the isothermal

disk as the solutions of the Poisson and Jeans equation. A basic picture of formation and evolution of the thin disk is that stars formed at the region near the mid-plane and were heated to the higher levels of the disk. The result is that the scale heights of older stars are larger than those of the younger stars. The TRILEGAL model (Girardi et al. 2005) presents this relationship using a power law function of stellar age. The Besançon model (Robin et al. 2003) uses a set of seven sub-populations with own scale heights, age ranges, and metallicities. The Just-Jahreiß model (Just & Jahreiß 2010; Just et al. 2011) produces a series of continuous sub-populations determined by the combination of Poisson and Jeans equations.

The thick disk was first proposed 28 years ago (Gilmore & Reid 1983). The stellar population in the thick disk is lower metallicity (Gilmore et al. 1995; Wyse & Gilmore 1995) than that in the thin disk. The age of the thick disk is basically larger than those in the thin disk (Fuhrmann 2008; Bensby et al. 2007). These views and observed facts are generally recognized. At least four formation mechanisms of the thick disk had been presented in the last decade. van der Kruit & Freeman (2011) summarized the four formation scenarios. Four possible mechanisms (orbital migration, mergers, accretion, and heating of pre-existing thin disk) have been tested (Dierickx et al. 2010) to account the contributions to the stellar orbital eccentricities of four mechanisms. The metallicity gradient of the thick disk subject to is considerable controversy. Robin et al. (2003) adopted the zero gradient on the abundance of the thick disk. Meanwhile, some studies have shown that this gradient may exist (Ibukiyama & Arimoto 2002). For now it seems, a lot of thick disk formation problems are not clearly explained. Do thick disks in different galaxies have different formation mechanisms? Does more than one mechanism play the role in the thick disk formation at the same time? With the emergence of a large number of new observational data and the introduction of new methods, we obtain a more comprehensive and more accurate understanding of the nature of the thick disk, and on this basis further explore the mechanism of thick disk formation and of the role played by chemical evolution. The TRILEGAL, Besançon, and Just-Jahreiß models adopt a single oldest population as the thick disk which can match the observation very well.

The detection of streams and faint dwarf satellites in the halo was and still is one of the most important fields in Galactic astronomy. Different methods have been tried to distinguish interesting targets from the background: the energy-angle momentum method based on kinematics (Gao et al. 2007), morphology based on color-magnitude diagrams (CMDs) (Liu et al. 2008). Eggen et al. (1962) gave the earliest results of Galactic archaeology based on the metallicity and the dynamics. They found the orbital eccentricity associated with the metal abundance of stars in the halo. The conclusion is the halo stars formed first in collapsing (and cooling) gas, and thus have orbits with random orientations. And the formation of the halo finished in the very early epoch. This picture was challenged by Searle & Zinn (1978): The clusters in the outer halo of a broader age range continued to fall into the inner halo after the collapse of its central regions had been completed. These facts suggest that the collapsing unified picture is not the only mechanism of formation of the halo in the Milky Way. At least, it is possible that some stars exist in the halo (even in the disk) from accretion and merging of satellites. Connecting the prediction of more dwarf galaxies by Λ CDM model, we have reasons to believe that the structure and evolution of the Milky Way cannot be explained thoroughly by a simple picture.

The halo and disks must be considered together for a merger or in-situ origin of the Milky Way and its external environment. For the thin disk, a self-consistent sub-population is adopted in models as the approximation of continuous evolution. The investigation of the giants is not perfect yet. Modeling of thin disk has been developed in last years, such as the “Besançon model” (Robin et al. 2003), “TRI-dimensional model of the GALaxy” (TRILEGAL Girardi et al. 2005), the Jurić model (Jurić et al. 2008) and our recent models (Just & Jahreiß 2010; Just et al. 2011; Gao et al. 2011). These models present a heating law by scale height as the function of sub-population age of the thin disk.

The radial mixing as an alternative model to the local dynamical heating was given by Schönrich & Binney (2009) and Roskar (2010). The mechanisms and effects of radial migration of stars in disks of the Milky Way were studied via the numerical simulation, i.e. smoothed-particle hydrodynamics (SPH). In the isolated disk models, the probabilities of migration depend on the mass profiles of disks and the radius. This mechanism provides the other prospect to study the formation of the disks.

Lu et al. (2000) and Chen et al. (2003) utilized the 2DF spectrograph at the Cerro Tololo Inter-American Observatory (CTIO) and with Hydra at the Wisconsin Indiana Yale & NOAO (WIYN) telescope to obtain the spectrophotometric data for nearly 2000 A, F and G stars towards the South Galactic Pole (SGP). These data include ~ 1300 radial velocities, 2300 *uvbyHb* photometries and ~ 1600 proper motions. The peculiar velocities were derived to determine the galactic gravitation force perpendicular to the Galactic plane, $K(z)$, first described by Oort (1932). Their results were derived from early-type stars (A0-F5) to support the B-S model without a thick disk which implies that dark matter exists in the galactic disk. And those results are also in agreement with the total surface density derived by Kuijken & Gilmore (1989) which implies that there is no need for dark matter in the disk when using late type stars (F6-G8).

1.3.2 Star counts and coordinate frame

The Milky Way is the only galaxy can be modeled by the star count method. This old method is providing a new chance to study our galaxy with the progress of observation instruments and data analysis methods. As a traditional method, star counts were developed over several decades since William Herschel’s first attempt.

The star count model concerns the numerical density $\nu(r, l, b, M, S)$ of stars with different types (intrinsic luminosity M and spectral type S) and different positions \vec{r} (heliocentric distance and Galactic coordinates). Its vector form is $\nu(\vec{r}, M, S)$ with the unit of pc^{-3} , which differs from stellar mass density ρ in unit of $\text{M}_{\odot}\text{pc}^{-3}$. The spectral type S can be presented as stellar effective temperature or color index like $(g - r)_0$.

The star counts of the MS can be used for modeling the stellar populations of the Milky Way. The luminosity function and density profile depend on the ages of the sub-populations, and luminosity function depends on the metallicity. At a given position, luminosity and stellar spectral type, the numerical density $\nu(\vec{r}, M, S)$ of each sub-population can be decomposed into two components as follows:

$$\nu(\vec{r}, M, S) dM dV = \Phi(M, S) dM \cdot D_S(\vec{r}) dV, \quad (1.1)$$

where $\Phi(M, \$)$ is the luminosity function (LF) and $D_{\$}(\vec{r})$ is the relative density function.

According to $dV = \omega r^2 dr$, the 2-D projection of star counts at given apparent magnitude m and spectral type $\$$ is

$$N(m, \$) = \omega \int_0^\infty \Phi(m + 5 - 5 \lg r - A(\vec{r}), \$) \cdot D_{\$}(r) r^2 dr, \quad (1.2)$$

where ω is the solid angle of observed volume, $A(r)$ is the extinction at position \vec{r} and $N(m, \$)$ is the total stellar number or general star count function at given m and $\$$. The $N(m, \$)$ of the model is the stellar numerical distribution along with color index and apparent magnitude which can be compared with a Hess diagram of observational data (on the Hess diagram see Chapter 1.4).

The luminosity function $\Phi(M, \$)$ and the relative density function $D_{\$}(\vec{r})$ is associated with the star type which can expressed as follows:

$$\Phi(M) = \sum_{\$} \Phi(M, \$), \quad (1.3)$$

$$D(\vec{r}) = \sum_{\$} D_{\$}(\vec{r}), \quad (1.4)$$

where the free-type functions $\Phi(M)$ and $D(\vec{r})$ are the general luminosity function and density function, respectively. The star counts are created on the basis of these two functions.

If the Milky Way contains more than one component, the general luminosity function $\Phi(M)$ and density function $D(\vec{r})$ may adopt a different form for each component. Considering that the solar Galactocentric distance is much less than the size of a bulge in the Galactic center, the bulge can be ignored for our purposes. That means there are two or three components of our Galaxy: Disk, halo and maybe an intermediate disk.

The luminosity function $\Phi(M)$ and the density function $D(\vec{r})$ should be normalized as follows:

$$\nu(\odot) = \int \Phi(M) dM \quad (1.5)$$

$$D(\odot) = 1 \quad (1.6)$$

where $\nu(\odot)$ is stellar numerical density at the solar neighborhood and the density function at position \vec{r} is a ratio of stellar numerical density and $\nu(\odot)$.

If star counts do not consider the stellar mass distribution, the result can only described using the numerical density. There is a difference of a factor $\langle m \rangle$ between the numerical density $D(\vec{r})$ and mass density $\rho(\vec{r})$. It is useful to assume that the Galaxy is a rotationally symmetric structure. Cylindrical coordinates are used for the Galactic structure description. Sometimes a spherical coordinate system is used for the spherical component.

According to the Galactic coordinate system, an (x, y, z) system is defined: x points to the direction of the sun along with the Galactic plane; z points to the north Galactic pole; $(0, 0, 0)$

locates on the Galactic center; and the Galactocentric distance r is $\sqrt{x^2 + y^2 + z^2}$.

$$\begin{aligned}x &= R_{\odot} - r \cos l \cos b \\y &= r \sin l \cos b \\z &= r \sin b\end{aligned}$$

(R, z) are the Galactic cylindrical coordinates,¹ which are converted from the cartesian (x, y, z) system:

$$R = \sqrt{x^2 + y^2},$$

The solar cylindrical coordinate (R_{\odot}, z_{\odot}) is from the following relationship:

$$\begin{aligned}R_{\odot} &= x_{\odot} = \sqrt{r_{\odot}^2 - z_{\odot}^2}, \\z &= z_{\odot} + r \sin b.\end{aligned}$$

where r_{\odot} is the Galactocentric distance of the sun².

The simplest density function of the disk is a double exponential decaying form which is described by the Bahcall & Soneira (1980a) model (BS model) and subsequent models. The numerical stellar density decreases along with radial distance from the Galactic center and height above the Galactic plane.

Taking into account a series of different stellar types with different scale heights above the midplane of the disk, the scale height and stellar density are the function of the spectral type. The double exponential decaying form can be written into two parts:

$$D_{dS}(R, z) = f_d \exp\left(-\frac{R - R_{\odot}}{\alpha} - \frac{|z|}{\beta(S)}\right) \quad (1.7)$$

where α and $\beta(S)$ is the scale length and scale height of the disk respectively.

An approximated de Vaucouleurs law was adopted by the BS model which means the spatial distribution of the stellar halo in the Milky Way is a $r^{1/4}$ exponential measured radially from the Galactic center, as follows:

$$D_h = f_h \left(\frac{r}{R_{\odot}}\right)^{-\frac{7}{8}} \exp\left\{-7.669\left[\left(\frac{r}{r_e}\right)^{\frac{1}{4}} - \left(\frac{R_{\odot}}{r_e}\right)^{\frac{1}{4}}\right]\right\} \quad (1.8)$$

where r_e is the effective radial length. If a flat spheroid is considered, the oblateness q is necessary. The normalized radius r can be written:

$$r = \sqrt{R^2 + \frac{z^2}{q^2}} \quad (1.9)$$

¹Note the uppercase R means a cylindrical coordinate and the lowercase r always stands for a spherical coordinate in this thesis.

²These two values r_{\odot} and R_{\odot} are very approximative because z_{\odot} is much less than them. We usually call R_{\odot} “the Galactocentric distance of the sun”, but in fact they have different meanings.

Another density law adopted widely is oblate power law:

$$D_h = f_h \left(\frac{R^2 + z^2/q^2}{R_\odot^2} \right)^{-\alpha_h/2} \quad (1.10)$$

where α_h is the power index and r is the normalized radius like in Equation 1.9. The ratio of halo to total density at solar neighborhood is indicated by f_h .

The de Vaucouleurs' $r^{1/4}$ law follows the photometric profile of disk galaxies by de Vaucouleurs (1948). According to Young (1976) and Gilmore (1984), the oblate spheroid is de-projected with the effective radius and the oblateness.

The power law is the simpler function with the feature of scale invariance. Best fitting results show that the difference between these two different laws is large at a distant position.

We have three free parameters local density, q_h and r_e in the de Vaucouleurs law and three free parameters in the local calibration, q_h and α_h in a power law function. The q_h has the same meanings as before to describe the flatness of the halo. And the r_e or α_h describes the trend of the density decay.

The traditional star counts tried to create an available approximation of the Galactic stellar populations in the few simplest law. However the results and components could be different when the sample changes. The argument for the existence of the thick disk has been going on for decades since the work of Gilmore & Reid (1983). The difference between two and three components may be caused by selecting different types of stars. Bahcall & Soneira (1980a) selected bright blue stars (early type, A and F) in order to utilize the photographic film. But Gilmore & Reid (1983) used late type stars, i.e. K and M. The scale of height of early type stars is much less than late type stars and early type stars are dominated by late type stars on the thick disk. That is why the observation could be matched well by the BS model without the intermediate population.

For luminosity function of the halo, globular clusters with special metallicity are usually used to represent the composition of Population II stars in the halo. The globular clusters M92 (NGC 6341, [Fe/H]=-2.29, (Harris 1996)) and 47 Tuc (NGC 104, [Fe/H]=-0.76, (Harris 1996)) are seen as two extreme cases. Gilmore (Colless et al. 1991) used M5 (NGC 5904, [Fe/H]=-1.29, (Harris 1996)) to represent the halo. Robin & Creze (1986) and Mendez (1995) used M3 (NGC 5272, [Fe/H]=-1.57, (Harris 1996)) as representative.

Since the seminal work by Bahcall & Soneira (1980a,b, 1984), the method of simulating star counts based on analytic Milky Way models has evolved considerably. There is a rapidly increasing set of observations with more accurate and much deeper photometry to constrain the parameters of the models of each population. The structural and evolutionary parameters of the Milky Way components have been defined in multi-population scenarios. The "perfect" results of the detailed form and the parameters of density profiles, star formation history (SFH), age-velocity dispersion relation (AVR), etc., however, have not been provided yet.

On the other hand, observations include more and deeper sky coverage and additional filter systems providing results that may require modifications of detailed Milky Way models. Analytic models are a powerful tool to constrain either evolutionary scenarios or assumptions about the Galactic structure through the comparison between model predictions and a large variety of observational constraints such as star counts and kinematics. Models create probable

distributions in the parameter space of observable or mock catalogues via Monte-Carlo simulations. Parameters and the details of further improvement can be obtained by comparing model predictions with suitable observations, like multi-directional photometric star counts. Within these parameters and functions, the density profile, SFH, and AVR are important inputs.

Over the last decade, more and more surveys of photometric or spectroscopic data have focused on the Galactic structure. These surveys have provided (and are providing) powerful tools to study our Galaxy by combining observations and theoretical models of stellar densities, kinematics, abundances, and population evolution.

1.3.3 Stellar population synthesis models

The theoretical stellar isochrones are needed for stellar population synthesis models, i.e. the loci in the theoretical HR-diagram ($\lg T_{\text{eff}}$, $\log L$) for a stellar population of a given age and chemical composition. Then the theoretical quantities $\lg T_{\text{eff}}$, $\lg L$, and $\lg g$ (with g being the stellar surface gravity) need to be transformed to observable quantities, i.e. magnitudes, color indexes, using the standard stellar atmosphere models. Finally by integrating along the isochrone weighting by the IMF and the flux, the final values are obtained.

For the simplest model, a single-age single-metallicity model can be considered to form all stars at the same time with the mass distribution following a given IMF, and with a uniform abundance. More complicated models adopt a group of single populations to approximate the stellar components in the Galaxy. An IMF and an abundance should be assigned for each sub-component.

PEGASE is presented by Fioc & Rocca-Volmerange (1997) and its second version was released in 1999 (Fioc & Rocca-Volmerange 1999). *PEGASE* is used for evolutionary synthesis by modeling the evolution of the stars, gas and metals which follow a specified stellar IMF. *MILES* (Vazdekis et al. 2010) provides a lot of useful tools to calculate modeling stellar spectra, line-strength predictions, and stellar population parameters.

Presently the Besançon model (Robin et al. 2003) is one of the most elaborate and refined tools to predict star counts. In this model, the Milky Way is divided in four components (thin and thick disks, spheroid, bulge), which are described by their SFHs, initial mass functions (IMFs), sets of evolutionary tracks, kinematics, and metallicity characteristics, and which include giants and a white dwarf population. From Monte-Carlo simulations, mock catalogues including observable parameters as well as theoretical ones are obtained. In the Besançon model the Einasto laws (Einasto 1979) of self-consistent density profiles for the disk sub-populations are used instead.

The TRILEGAL model, which is a Monte Carlo simulation to predict the probability distributions of stars across small sky areas and for special pass-bands systems, is still a work in progress. TRILEGAL is a population synthesis code to simulate photometry of any field in the Milky Way (Girardi et al. 2005). It was developed in order to model population synthesis star counts of the Milky Way. It allows its users to create a pseudo stellar catalogue including positions, multi-color photometry, and other physical parameters according to user-defined structural parameters.

Very recently Sharma et al. (2011) presented *Galaxia*, a new code which combines the

advantages of the Besançon and the TRILEGAL models. The code generates very efficiently synthetic surveys and allows to choose between a much larger variety of input models. Unfortunately, their codes have not been released yet.

All population synthesis models still have problems to predict the luminosities and colors in *ugriz* filters. The TRILEGAL and Besançon models will be discussed deeply in following chapters.

1.3.4 A self-consistent local disk model

Just & Jahreiß (2010) presented a new Galactic disk model (hereafter “Just-Jahreiß model”) with the self-consistent method. The density profile, potential, and the velocity dispersion of each component fulfill the self-consistent relationship as follows:

$$\rho_{s,j}(z) = \frac{g(\tau_j)\text{SFH}(t_j)dt}{2h_d(\tau_j)} \exp\left[\frac{-\Phi(z)}{\sigma_w^2(\tau_j)}\right]$$

where $\rho_{s,j}$ is the density of the thin disk (component s) with the age bin j , the g accounts for mass loss by stellar evolution, the thickness h_d and potential Φ are determined iteratively via kinematics constraints. The thin disk is expressed using a continuous set of isothermal subpopulations with age range from 0 to 12 Gyr and the size of bins 25 Myr. The thick disk has a single population with the oldest component of 12 Gyr. And the density profile of the thick disk can be fitted by a hyperbolic secant function with power index α_t

$$\rho_t(z) = \rho_{t,0} \text{sech}^{\alpha_t}\left(\frac{z}{\alpha_t h_t}\right)$$

where the structural parameters, power index α_t and scale height h_d , depend on the velocity dispersion and on the total potential in the Milky Way. The thick disk has a single isothermal population.

In Just et al. (2011) we compared this model with SDSS data at the Galactic pole field in order to constrain the SFR of the thin disk. The “model A” of Just-Jahreiß model shows excellently matching luminosity functions and Hess diagrams. The typical discrepancy of star counts in the color-magnitude diagram (CMD) is less than 5 per cent. The total local star numbers determined from fitting data are in reasonable agreement with local survey. However some discrepancies should be researched and improved. The details will be discussed in this thesis.

As the self-consistent disk model, the Just-Jahreiß model uses main sequence (MS) stars to construct the isochrones instead of using full CMD with its additional other luminosity classes. In order to improve that, the contribution of the giants should be considered and measured.

1.4 Comparisons of models

Traditionally, ones compared the model to the observed data by only luminosity functions and not full CMDs.

The isochrones reflect the stellar population components in the CMD using the absolute magnitude (or apparent magnitude for a cluster). The model isochrones depend on the ages, abundances, IMFs of stellar populations. The isochrones can be contoured by the relative density on CMDs to compare with the fiducial sequences determined by clusters. An et al. (2008) observed clusters and obtained their mean ridge lines in color-magnitude space, a so-called fiducial sequence that represents an “observational isochrones”. The observed magnitudes can be converted to absolute magnitudes and de-reddened colors via the parameters of Harris (1996) and the extinction law (see Chapter 2). The de-reddened CMDs of clusters with different metallicities are treated as fiducial sequences, which are overplotted on the model isochrones to compare the MS and turn-off positions. The general match of modeling isochrones and fiducial sequences of clusters is one of the basic requirements. The thick disk and halo of a model are first tested by isochrones.

The distributions of apparent magnitudes (in the case of no confusion, it is called as “luminosity function” in this thesis) are the star counts at different apparent magnitudes. As the function of apparent magnitude, the sum of luminosity functions of different components can be compared with data. The star numbers per magnitude and square degree are usually expressed with the logarithmic form. Only sample within a given color limit is considered. The TRILEGAL and Besançon models have been compared with data using the luminosity function (V band usually) (Girardi et al. 2005; Robin et al. 2003). The SDSS filters are used for this aim in this thesis.

A Hess diagram plots the relative density of occurrence of stars at different color-magnitude positions of the Hertzsprung-Russell diagram for a given galaxy. Such a representation is referred to as a Hess Diagram after R. Hess (Hess 1924). The density contour is expressed by the color/spectral-type or grey scale plotting. The x- and y-axis are the color index and the (apparent) magnitude with given limits, respectively. The color coding or gray scale adopts linear or logarithmic scale to sort the density contours. The rainbow and logarithm are common color scales. The different colors on a Hess diagram stand for different relative star counts in the given color and magnitude box of unit area of a certain direction. Observed Hess diagrams for regions in the Milky Way integrate all of the stellar contents including disks and halo (and a bulge if the direction points the Galactic center) within a user-defined volume. Modeling Hess diagrams can display the contributions of different components separately which helps to study the structures of stellar populations. A minor application is to calculate the probability of a star at given magnitude, color and position belonging to one population.

In order to measure the quality of the model and fitting results, the relative difference D_{ij} and χ^2 value of the Hess diagram are defined. Each Hess diagram contains $m \times n$ boxes of magnitudes and colors. The relative difference of each Hess diagram is a matrix D_{ij} with the indexes i of the magnitude and j of the color

$$D_{ij} = \frac{Y_{ij} - N_{ij}}{N_{ij}},$$

where Y_{ij} and N_{ij} are the data and the model respectively. The χ^2 is defined as follows

$$\chi_i^2 = \sum_{gj} \frac{(\lg Y_{ij} - \lg N_{ij})^2}{\sigma_{ij}^2}$$

where the weights are expressed by data $\sigma_{ij}^2 = \frac{1}{Y_{ij}}$. The total χ^2 is the normalized sum of each color bin i

$$\chi^2 = \frac{A_{\text{NGP}}}{1 \text{deg}^2} \frac{d(g-r)}{0.1 \text{mag}} \frac{\Delta g}{1 \text{mag}} \sum_i \frac{\chi_i^2}{n \times \text{dof}_i},$$

the normalized coefficient is the area of the field, box size of the color and the magnitude, the degree of freedom (dof_i) of each color bin i depends on the fits in g .

The relative difference of the Hess diagrams D_{ij} is used to display the discrepancies between models and data in the 2-D spaces of magnitudes and colors. This helps find the places that need to be improved. The χ^2 distributions of Hess diagrams give the final measurements of qualities of the models. This measurements are comparable with others. The total χ^2 values are used to characterize for the total quality of a model. Because the total χ^2 value depends on dof_i and the bin size of color, these values should be compared with each other using the same conditions.

1.5 Motivation for this thesis

A simple and efficient method of comparison between models and data is needed. The photometric data of SDSS (or 2MASS and etc.) can be used for the comparisons directly via stellar sequences, luminosity function, and Hess diagrams.

Based on SDSS photometry of Data Release 6 (DR6, Adelman-McCarthy et al. 2008) Jurić et al. (2008) derived a three-dimensional stellar distribution of the Milky Way by applying universal photometric parallaxes. Then they fitted two disks with exponential profiles in radial and vertical direction. They found vertical scale heights of 300 pc and 900 pc for the thin and thick disk, respectively. The local density normalization of the disks and basic parameters of the stellar halo were also determined. Subtracting the resulting, smooth Milky Way model, over-densities (and under-densities) are revealed that can be investigated in more detail.

Just & Jahreiß (2010) have developed a new local Milky Way model based on local stellar kinematics and star counts in the solar neighborhood (hereafter “Just-Jahreiß model”). Compared to the Besançon and TRILEGAL model, the main improvements of their approach are vertical density profiles consistent with the SFH and AVR in the gravitational field. The vertical density profile is determined by the solution of a combination of Poisson equation and Jean equation. One shortcoming of the Just-Jahreiß model in the current state is that it uses the mean main sequence (MS) only instead of including other evolutionary phases of the full Hertzsprung-Russell diagram with mixed stellar populations. We recently compared the basic disk model (Just & Jahreiß 2010) with SDSS star counts in the North Galactic Pole (NGP) field with $b > 80^\circ$ in order to verify the SFH and AVR prescriptions (Just et al. 2011) and found an optional combination to reproduce the observed Hess diagram.

These models should be simulated and compared with new data on star counts of the Milky Way. And then their (dis)advantages could be studied and presented for testing different SFH, AVR, and IMF.

In this thesis four main tasks were addressed:

- The first one is to use Just-Jahreiß model to reproduce the star count at the NGP fields. This is an important step in the process of the Just-Jahreiß model improvement.
- The second one is focuses on the TRILEGAL model. We test the ability of the TRILEGAL model to reproduce the different Milky Way models mentioned above, since the TRILEGAL model is presently the only code which allows an interactive analysis of the impact of model parameter variations on star count predictions. We restrict the analysis on the SDSS star count data of the NGP field, since these are very high quality data and they give a direct measure of the controversial vertical structure of the thin and thick disks. Additionally we try to determine a best-fit model by a systematic input parameter optimization in TRILEGAL.
- The third task is an analysis of multi-color simulations of the Besançon model. All of those use SDSS DR7 data as our observation sample of star counts. In order to test the vertical structure of the disks, we select the NGP field as our target. So far the scale length can be ignored in these cases.
- The Just-Jahreiß model are compared in several low-latitude fields with the SDSS data. The radial sub-structures, over-density (under-density), and the scale lengths of the thin and thick disks are studied to be the basis of the future works.

The structure of this thesis is organized as the follows: The data mentioned are introduced in Chapter 2. In Chapter 3, we describe the details of the TRILEGAL model, the Besançon model, the Jurić model, and the Just-Jahreiß model respectively. In Chapter 4 we compare Just-Jahreiß with SDSS data using the star counts in the NGP field. In Chapter 5 we present the process to reproduce simulated catalogues including the choice of the input parameters for the four different models of the TRILEGAL model. In Chapter 6 we analyze the Besançon model via multi-color modeling and compare them with the SDSS star counts in the NGP field. The low latitude fields are considered in Chapter 7. In Chapter 8 this thesis is summarized and the next steps for the future are proposed.

“No matter what our society becomes, no matter what kind of pain or happiness we face, there are stars following some rules.”

My wife, 2009

2

Data

The SDSS is the one of largest projects to obtain photometric and spectral data of stars and galaxies. The SDSS data include multi-color imaging (and photometric catalogue from that), 1- and 2-D spectra and catalogues of stellar physical parameters derived from stellar spectra.

The instrument of SDSS is a 2.5-meter telescope at Apache Point Observatory (latitude $32^{\circ}46'49.30''$ N, longitude $105^{\circ}49'13.50''$ W, elevation 2788m), New Mexico, USA. A 3° distortion-free field of view (FOV) and the observing technique — contiguous drift scans for imaging, multi-object spectroscopy — makes the efficiency of this northern survey very high. The 2k by 2k CCDs obtain stellar photometric data via five special filters u, g, r, i and z (Their properties are listed in Table 2.1). Taking account some gaps between the rows of CCDs, the effective exposure time in each filter is 54 seconds with a limiting magnitude of $r \sim 22.6$ mag. The g and r band point source imaging of the SDSS ranges from 14 to 22 mag.

Taking into account the magnitude limits, our selection range for stellar apparent de-reddened magnitudes is from 14 to 20.5 mag.

SDSS carries out its observations during three phases: SDSS-I (2002—2005), SDSS-II (2005—2008) and SDSS-III (2008—2014). SDSS-I includes the early data release (EDR) and the first to the fifth data release (DR1 to DR5). SDSS-II includes DR6 and DR7. Since DR8 had been released in January 2011, SDSS-III began to publish data. DR7 is selected to use for comparison with models because DR7 has covered NGP field and most of the northern hemisphere and has been calibrated using new pipelines for data processing. DR8 has been available since a few months now as the latest data set. The difference between DR7 and DR8 is discussed in Section 2.3.

More than 22% of full sky area has been observed and the photometric data with five bands of 2.6×10^8 stars are obtained. These achievements make creating a substantial Galactic model possible. The SDSS has become one of the most widely used data bases for Galactic and extragalactic astronomy during recent years.

2.1 Stars

2.1.1 Photometry and selection

We selected stars from the Catalog Archive Server (CAS) of DR7 of the SDSS (Abazajian et al. 2009). The SDSS table *Star*, which we utilize, contains the photometric parameters (no

Table 2.1: The central wavelengths, the full width at half maximum (FWHM) and magnitude limits of five filters used for SDSS photometry

Filters	Central wavelengths (nm)	FWHM (nm)	Magnitude limits (mag)
<i>u</i>	355.1	57	22.0
<i>g</i>	468.6	137	22.2
<i>r</i>	616.6	137	22.2
<i>i</i>	748.1	153	21.3
<i>z</i>	893.1	95	20.5

Note: The central wavelengths are the effective average wavelengths of response curves. The FWHM is the full width at half maximum of each response curve from instrument calibration. The magnitude limits are determined by the 95% completeness for point sources.

velocities or spectroscopic parameters) for all primary point-like objects classified as “star” from *PhotoPrimary*. It is possible that there is still some pollution by galaxies (or AGNs) in the sample.

We use the de-reddened magnitude via SDSS point-spread function (PSF) photometry and extinction map (Schlegel et al. 1998) of each field directly. We obtain photometric data *dered_u*, *dered_g*, *dered_r*, *dered_i*, *dered_z*, and *psfMagErr_g* from CAS.

We consider the NGP field (Galactic latitude $b > 80^\circ$, Galactic longitude $0^\circ \leq l < 360^\circ$) in this work and a series of lower latitude fields for the future. The coverage area A of the stellar sample in the NGP field is 313.3626 deg^2 . This direction is used for the vertical structure on the plane of the Milky Way. This sky area includes 2,597,069 “stars” in DR7 star catalogue.

We select all stars in DR7 within a color range of $(g - r) = [-0.2, 1.2]$ and magnitude limits of $g = [14, 20.5]$ and magnitude errors of g band below 0.2 mag. This color range covers most of MS stars on the CMD. The photometric saturation at brighter than 14 mag cannot be neglected (see the magnitude distribution at ~ 14 mag in Figure 2.6) and the credible signal to noise ratio ($\text{SNR} > 50 : 1$) appears at brighter than 20.5 mag (Gunn et al. 1998). Stars fainter than 20.5 mag are excluded because of low SNR and the pollution by galaxies (Lupton et al. 2001). In this range we get a sample with 274,519 stars. There are 9.72 stars per square degree per magnitude and per 0.1 color magnitude interval in NGP field in this sample.

2.1.2 Spatial distribution

The spatial distribution of stars at the NGP field is drawn in Figure 2.2. The average numerical density is $274519/313.3626 = 876$ per square degree. The actual density is smaller than this average value at the direction of Galactic anti-center and it is larger than the average at the direction of lower latitude and Galactic center. A large area (313.3626 deg^2) reduces the random noise and the asymmetry.

The extinction at the NGP field is much smaller than the lower latitude fields. The extinction at g band is displayed in Figure 2.3 with the color coding which is up to 0.11 mag. The

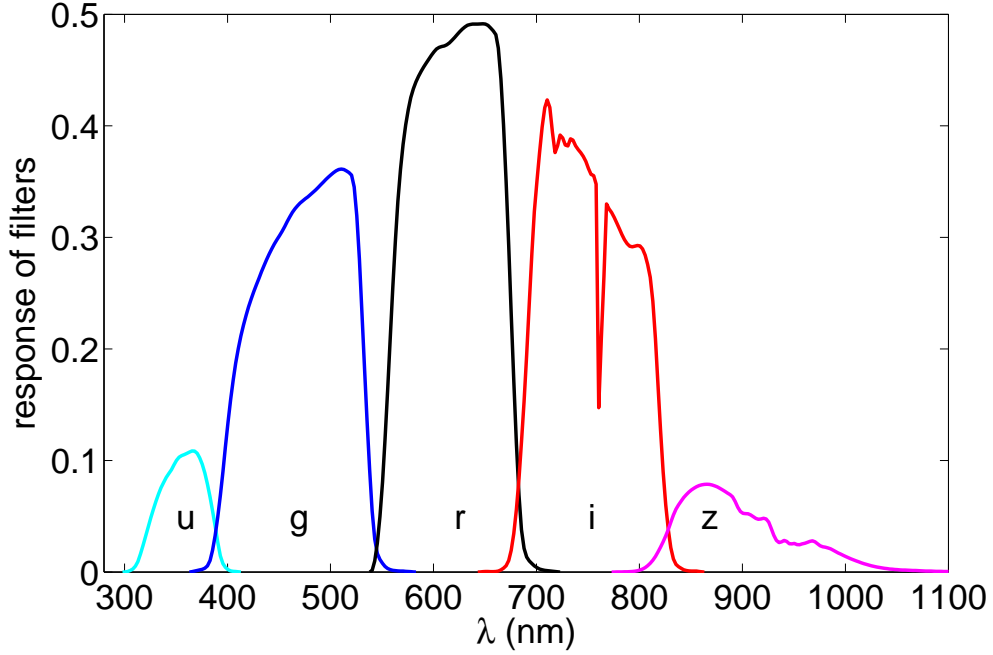


Figure 2.1: The response curves of the five filters of SDSS stand for the throughput defining the survey's photometric system, which includes extinction through an air-mass of 1.3 at Apache Point Observatory.

map displays large asymmetry in spatial distribution. The transition between the 3rd and 4th quadrant of the Galactic coordinate system shows up as a significant pattern. The total effect, however, is limited below ~ 0.1 mag. The de-reddened magnitude determined from Schlegel et al. (1998) is available at the NGP field.

2.1.3 Hess diagram and luminosity function

We plot Hess diagrams of the number density distribution of stars in color-magnitude bins normalized to 1 deg^2 sky area in the CMD. Star counts are stowed in each CMD in boxes of (0.05 mag in color, 0.01 mag in magnitude, see Figure 2.4) and boxcar smoothing in steps of 0.1, 0.2, and 0.5 mag respectively at the magnitude direction. The boxcar smoothing calculates the average values of 10, 20, and 50 bins and slides along with magnitude axis. The 0.5 mag smoothing size is our default setup for the Just-Jahreiß, TRILEGAL, and Besançon models. The other two sizes are used for the Just-Jahreiß model to compare the detailed effects of different bin sizes.

Number counts are given in log-scale covering a range of $1 \dots 100$ per deg^2 , 0.1 mag in color and 1 mag in luminosity. Hess diagrams of selected regions in the Milky Way are a powerful tool to compare observed star counts with model predictions. One obvious deficiency are the unknown stellar distances, hence the vertical axis of the CMDs necessarily shows

apparent magnitudes instead of absolute magnitudes. The combined distribution of (apparent) stellar luminosity and color shows the spatial structure and the population properties for each chosen direction, which can then be compared with model-generated Hess diagrams.

In Figure 2.5 the area from the SDSS DR7 photometric catalogue with 277,123 stars is shown. From the top right (purple/blue) of each panel to the bottom left (red triangle) thin disk, thick disk, and halo dominate, respectively. In the top-left of each panel in Figure 2.5, no stars appear. In the bottom-left of each panel, white dwarfs, blue horizontal branch stars and blue stragglers appear at $g - r < 0.2$.

The magnitude distribution is obtained by projecting the Hess diagram along the X-axis. Number counts as a function of magnitude are an important and more robust quantity. In Figure 2.6 the the SDSS data are shown for the complete range in g band in order to illustrate total numbers and the cutoffs at bright and faint magnitudes. Poisson error bars were adopted. The incompleteness at $g > 22$ mag is obvious and a significant confusion with misidentified extragalactic sources is likely to occur here. To be on the safe side we choose $g = 20.5$ mag as the faint limit. One significant jump appears at 14 mag caused by the incompleteness. The bright limit at 14 mag is set by the saturation of the stars in the SDSS.

The ring fields and a low stripe are considered to compare with models also. The sky area selections, Hess diagrams of the SDSS data and the models are discussed in Chapter 7.

2.2 Globular clusters

2.2.1 Photometry

Apart from the catalog from DR7, we select the photometric data of globular clusters by An et al. (2008) to compare the resulting fiducial isochrones to model isochrones. According to the extinction parameters and distance modulus of each globular cluster, the de-reddened absolute magnitude and color index are determined.

During the SDSS-I phase, 15 globular clusters were observed. And then two more clusters were imaged in SDSS-II, such as M71. Using the standard SDSS photometric pipelines the magnitudes of single stars in each cluster were reduced from images and PSF. Because the pipelines (*Photo*) were designed for the low density fields at high latitude, the crowded fields as present in a cluster need an optimized pipeline process. An et al. (2008) adopted *DAOPHOT* as the tool to reduce the crowded field photometry.

2.2.2 Parameters

The parameters of 17 globular clusters are listed in Table 2.2. The reddened magnitude and color index of each cluster are listed in Table 9, 12 to 23 and 25 to 28 of An et al. (2008) as their fiducial isochrones. The photometry of An et al. (2008) is uncorrected for reddening and absolute magnitudes need to be determined. Their de-reddened magnitude g_0 and r_0 need to

Table 2.2: Properties of globular clusters used for fiducial isochrones

Number	NGC	Name	l (deg)	b (deg)	V_{HB} (mag)	$E(B - V)$ (mag)	$(m - M)_0$ (mag)	[Fe/H]
1	6838	M71	56.744	-04.564	14.48	0.25	13.02	-0.73
2	5904	M5	3.863	+46.796	15.07	0.03	14.37	-1.27
3		Pal 5	0.852	+45.860	17.51	0.03	16.83	-1.41
4		Pal 4	202.311	+71.803	20.80	0.01	20.19	-1.48
5		Pal 14	28.747	+42.199	20.04	0.04	19.35	-1.52
6	6205	M13	59.008	+40.912	15.05	0.02	14.42	-1.54
7	5272	M3	42.208	+78.708	15.68	0.01	15.09	-1.57
8	7089	M2	53.371	-35.770	16.05	0.06	15.30	-1.62
9	7006		63.770	-19.407	18.80	0.05	18.09	-1.63
10		Pal 3	240.139	+41.861	20.51	0.04	19.84	-1.66
11	4147		252.849	+77.189	17.01	0.02	16.42	-1.83
12	5024	M53	332.967	+79.765	16.81	0.02	16.25	-1.99
13	2419		180.370	+25.242	20.45	0.11	19.63	-2.12
14	5466		42.150	+73.592	16.47	0.00	16.00	-2.22
15	7078	M15	65.013	-27.313	15.83	0.10	15.06	-2.26
16	6341	M92	68.339	+34.859	15.10	0.02	14.58	-2.28
17	5053		335.690	+78.944	16.65	0.04	16.07	-2.29

Note: Column 1 and 2 list NGC IDs and available alternate names of 17 globular clusters used for comparison with models' isochrones. These clusters are sorted by metallicities in descending order. Column 3 and 4 list the Galactic longitudes and latitudes of globular clusters in degree. Column 5 lists the V magnitude of horizontal branch of each cluster. Column 6 and 7 are their color excess $E(B - V)$ and distance moduli $(m - M)_0$ from An et al. (2008). Column 8 lists metallicity of each cluster. Harris (1996) metallicities are adopted here to have a consistent source of observed measurements.

be determined by color excess $E(B - V)$ given in Table 2.2 and reddened magnitude g and r ,

$$u_0 = u - 5.155 \cdot E(B - V), \quad (2.1)$$

$$g_0 = g - 3.793 \cdot E(B - V), \quad (2.2)$$

$$r_0 = r - 2.751 \cdot E(B - V), \quad (2.3)$$

$$i_0 = r - 2.086 \cdot E(B - V), \quad (2.4)$$

$$z_0 = r - 1.479 \cdot E(B - V), \quad (2.5)$$

$$(u - g)_0 = (u - g) - 1.362 \cdot E(B - V), \quad (2.6)$$

$$(g - r)_0 = (g - r) - 1.042 \cdot E(B - V), \quad (2.7)$$

$$(r - i)_0 = (r - i) - 0.665 \cdot E(B - V), \quad (2.8)$$

$$(i - z)_0 = (i - z) - 0.607 \cdot E(B - V), \quad (2.9)$$

$$(2.10)$$

Table 2.3: Extinction parameters of different bands of the SDSS system.

Filter	$\lambda_c(\text{\AA})$	$A_\lambda/E(B - V)$
<i>u</i>	3546	5.155
<i>g</i>	4925	3.793
<i>r</i>	6335	2.751
<i>i</i>	7799	2.086
<i>z</i>	9294	1.479

Note: Column 1 lists names of 5 SDSS filters. Column 2 is the central wavelength of each filter in units of \AA . Column 3 lists the ratio of total to selective extinction, R_λ parameter of each band. An $R_V = 3.1$ is assumed.

where the extinction parameters of different bands are listed in Table 2.3.

According to the definition of distance module and magnitude extinction,

$$m - M = 5 \lg(d) - 5 + A(d), \quad (2.11)$$

$$(m - M) - A(d) = 5 \lg(d) - 5, \quad (2.12)$$

$$(m - M)_0 \equiv 5 \lg(d) - 5, \quad (2.13)$$

the extinction of magnitude is available for different filters.

The absolute magnitudes M_u , M_g , M_r , M_i , and M_z are determined by applying the distance modulus given in Table 2.2 and de-reddened magnitude g_0 from Equation 2.2 as following:

$$M_u = u_0 - (m - M)_0, \quad (2.14)$$

$$M_g = g_0 - (m - M)_0, \quad (2.15)$$

$$M_r = r_0 - (m - M)_0, \quad (2.16)$$

$$M_i = i_0 - (m - M)_0, \quad (2.17)$$

$$M_z = z_0 - (m - M)_0. \quad (2.18)$$

$$(2.19)$$

2.2.3 The isochrones of clusters

The final results of de-redden magnitudes, color indexes, and absolute magnitudes of each cluster are used for our standards. Since the members of the globular clusters have the similar distances, ages, and metallicities, the mean rigid lines of MS (and partial giants) of the globular clusters are adopted to stand for the fiducial isochrones of the SDSS data.

The one color of fiducial isochrones of globular clusters based on de-reddened absolute magnitude M_g and intrinsic color index $(g - r)_0$ are plotted in Figure 2.7.

According the metallicities of different models, the fiducial isochrones of two or three globular clusters are used to cover the stellar sequences on the absolute-magnitude diagrams

of models. The fiducial isochrones indicate the actual metal abundance (and age limit) of matched models.

An et al. (2009) compared the fiducial isochrones of the six globular clusters (and two open clusters) with several models in the CMDs of $(g-r, M_r)$, $(g-i, M_r)$, $(g-z, M_r)$, and $(u-g, M_r)$, respectively. The stellar models from the Yale Rotating Evolutionary Code (YREC, Sills et al. 2000) and a grid of one-dimensional, hydrostatic, plane-parallel and spherical LTE model (named MARCS, Gustafsson et al. 2008) were considered to be compared with the data. The theoretical isochrones of Girardi et al. (2004), the Padova stellar evolutionary tracks, and the grids of the ATLAS9 model were compared to be the references (Castelli et al. 1997; Bessell et al. 1998).

There is the systematic difference between isochrones of globular clusters and models in $(g-r, M_r)$, $(g-i, M_r)$, and $(g-z, M_r)$ slightly, i.e. the color difference are less than 0.04 mag. There are the ~ 0.1 mag offsets in the $(u-g)$ for all metallicities and all clusters. The u band was considered to be suspect, since the $(g-r)$ and $(g-i)$ showed the good agreement with the data. The cluster M71 showed a worse agreement with the model than the other clusters. That may means that color transformation for this highly reddened cluster has a problem, which still has not been sure. As the functions of cluster metallicities, the color differences between models and fiducial sequences were studied. The metal-rich clusters with $[\text{Fe}/\text{H}] > -1.0$ showed the worse agreements with the models than the metal-poor clusters. The worst agreements were in the $(u-g)$, the differences between models and the data were larger than ~ 0.12 mag.

Meanwhile, An et al. (2009) found that the strong departure of the models from the open cluster isochrones of the lower MS stars. The large offsets in the $(g-z)$ for Dartmouth stellar evolution database (DSEP) and PHOENIX models (Hauschildt et al. 1999) were found also. The YREC and MARCS models were better than the others to match the observed data.

The fiducial isochrones of the SDSS data determined by the globular clusters are our standards to compare the sequences of models in CMDs. When the globular clusters with the similar metallicities are selected to overplot the sequences of models in the CMDs, the MS and turn-offs of the fiducial isochrones and models should be consistent. The significant shifts of isochrones between observed globular clusters and models reveal shortcomings of the models, which are caused by the abundance laws or stellar population synthesis processes.

These comparisons are for the thick disk and halo both. For the thick disk, the globular cluster M71 (NGC 6838, $[\text{Fe}/\text{H}] = -0.73$) and M5 (NGC 5904, $[\text{Fe}/\text{H}] = -1.27$) are selected to compare with the Just-Jahreiß, TRILEGAL, and Besançon models. For the halo, five different clusters are selected to compare with three models: Pal 5 ($[\text{Fe}/\text{H}] = -1.41$), M13 (NGC 6105, $[\text{Fe}/\text{H}] = -1.54$), M3 (NGC 5272 $[\text{Fe}/\text{H}] = -1.57$), NGC 4147 ($[\text{Fe}/\text{H}] = -1.83$) and M92 (NGC 6341, $[\text{Fe}/\text{H}] = -2.28$).

2.3 DR7 and DR8

SDSS DR8 (Aihara et al. 2011) was released recently. Besides including new data, former data are re-calibrated also. I tested the difference between DR7 and DR8 using a Hess diagram at

NGP field.

The main differences between DR7 and DR8 (Figure 2.8) are reflected in three places as following:

1. The largest difference is bright-blue (top left corner of Hess diagrams). The relative difference between DR8 and DR7 is 20% in this region. But its stellar number density is less than 1 star per unit interval, the effect is not too big. The region extends to 18th ... 19th mag with the relative difference of 5%. DR8 has fewer stars than DR7 in this part of Hess diagrams.
2. The second largest difference is bright-red (top right corner of diagrams). The difference value is close to 20% in the worst spot. The stellar number density is less than 3 stars per unit interval in this part. And the density at the worst spot is less than 1. This part extends to 16th mag only.
3. At the main star counts area (covered by MS and RGB stars of models), the relative difference is not larger than 5%.

For our model comparison with SDSS DR7, the only significant caveat is the spot with range of color $0.8 < g - r < 1.0$ and magnitude $15.5 < g < 16.5$. I estimate the error is about 0.5 star per unit interval and I suppose it can be neglected.

I tested three improvements of DR8 with DR7: magnitude re-calibration, photometric error improvement and star/Galaxy classification.

These changes are drawn as the distribution plots (Figure 2.9 and 2.10).

The changes of g magnitudes (the left panel of Figure 2.9): 88.10% stars with $|\Delta g| < 20$ millimag, 82.04% stars with $|\Delta g| < 15$ millimag, 70.05% stars with $|\Delta g| < 10$ millimag. The changes of $g - r$ (the right panel of Figure 2.9): 86.83% stars with $|\Delta(g - r)| < 20$ millimag, 79.86% stars with $|\Delta(g - r)| < 15$ millimag, 66.19% stars with $|\Delta(g - r)| < 10$ millimag. These changes of magnitude create the minor shifts on Hess diagrams between DR8 and DR7.

There is not any significant improvement of photometric error between DR8 and DR7 (see Figure 2.10). The change of star counts cannot be caused by the error limit. In fact, the number of stars of DR8 with error of < 0.2 mag is not reduced as compared to the DR7. Only reason of changing star total number in the NGP field is the new classification of “star” and “galaxy” in the SDSS.

The star counts of DR8 are less about 1.5% than DR7 in NGP. These missing objects are mainly faint point sources with the magnitudes of $g > 21$.

As mentioned above, the changes between DR8 and DR7 photometric data are mainly caused by magnitude changes and new classifications. In order to study the contribution of new classifications, the Hess diagrams are smoothed using 0.1×0.5 mag to filter out the differences caused by the magnitude change.

The smoothed difference Hess diagrams are plotted using 20% and 5% scales respectively. These differences represent how many stars are classified as galaxies and how many galaxies convert to stars. In the bluer (than turn-off) part, 10% “stars” are reconsidered as galaxies. But at the red end, 20% bright stars are “rediscovered” from former galaxies. These most serious changes appear around $g = 14.5^{\text{th}} \dots 16^{\text{th}}$ mag.

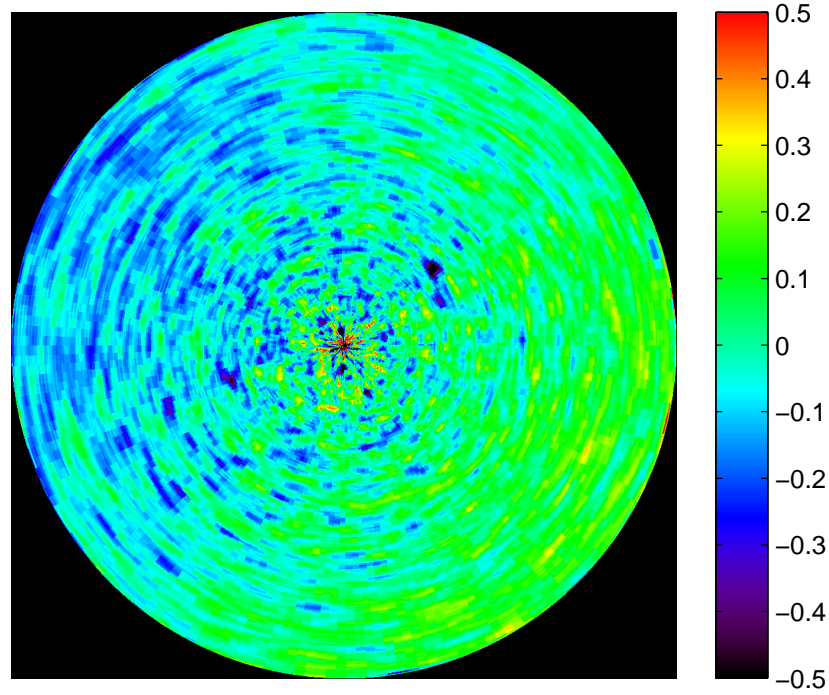


Figure 2.2: The relative spatial distribution of our sample at the NGP field. The color coding stands for the relative difference between star numerical density and their average (876 stars per deg^2). The color coding is from -50% to $+50\%$. In polar coordinates, the center of the circular figure is the northern Galactic pole. The left edge of this figure points the direction of the Galactic center. The Galactic longitude is along with the counterclockwise direction from 0 to 360 deg. The Galactic latitude of 80 to 90 deg is from outer edge to the center of this figure.

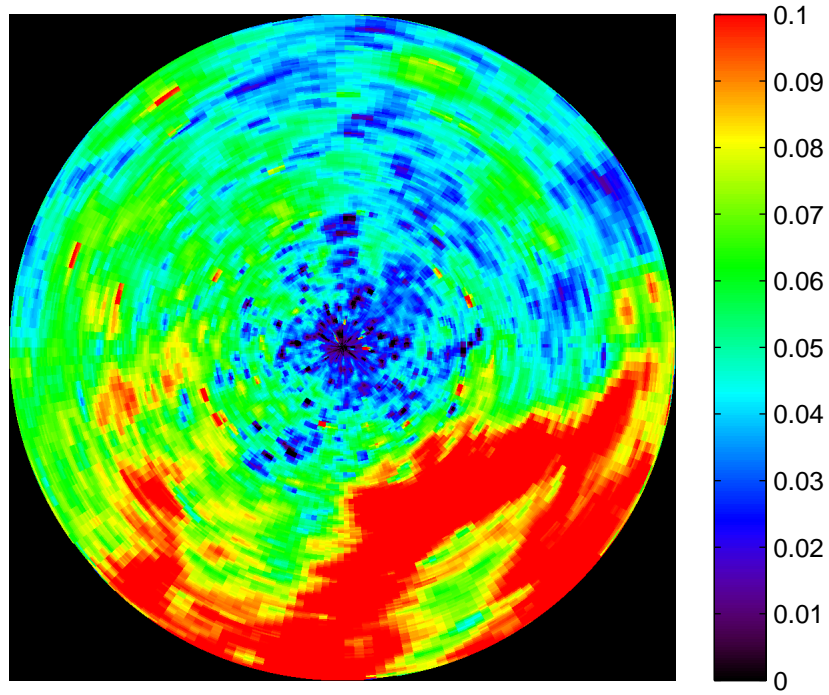


Figure 2.3: The extinction distribution at the NGP field. The color coding stands for the extinction at g band A_g based on the maps of Schlegel et al. (1998). This figure adopts the polar coordinates used in Figure 2.2.

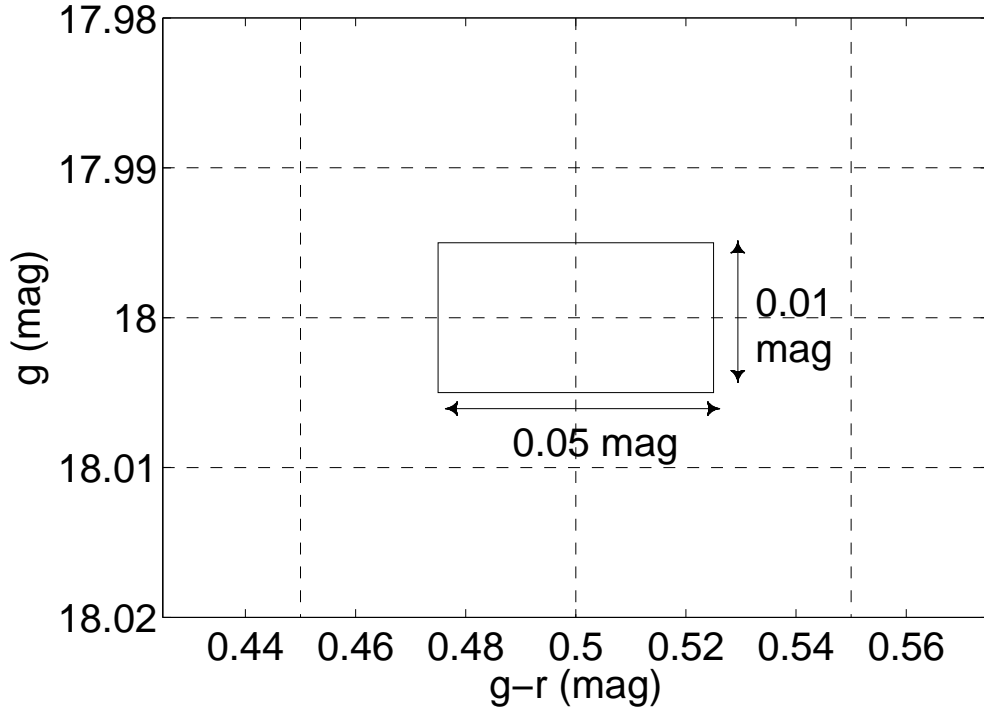


Figure 2.4: The scheme displays the box size of Hess diagrams adopted in this thesis. The color and magnitude bins are 0.05 and 0.01 mag respectively. In this figure, for example, stars belonging in the range of $0.475 < g-r \leq 0.525$ and $17.995 < g \leq 18.005$ are accounted as the density value at the point $(g-r, g) = (0.5, 18)$. A full Hess diagram contains 29×651 points. A car-box smoothing of 0.5 mag size as a standard in the g axis is used to the further studies.

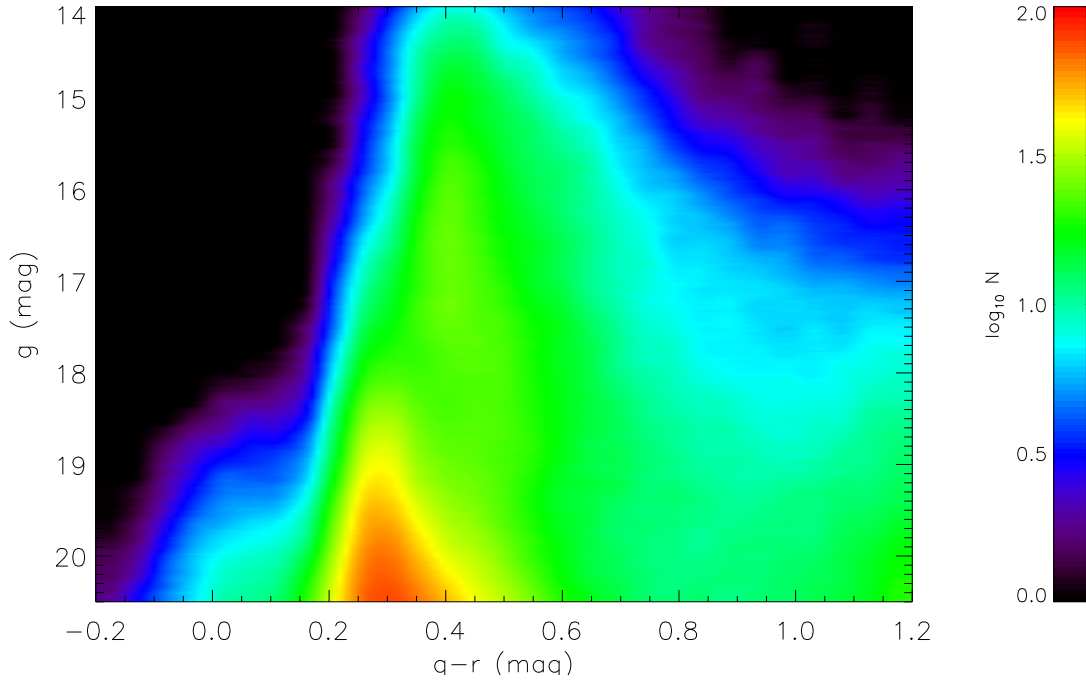


Figure 2.5: Hess diagrams of the stellar sample selected from SDSS DR7. The NGP field covers an area of 313.36 deg^2 . The x-axis is the de-reddened color index ($g - r$) and the y-axis is the de-reddened apparent magnitude g . The number density per square degree in each bin of 1 mag in g and 0.1 mag in ($g - r$) is coded by rainbow colors in logarithmic scale from 0 to 2. The stellar number density has been smoothed with a moving average box of 0.5 mag in g and 0.05 mag in $g - r$. The faint blue plume is dominated by mis-identified unresolved extragalactic objects.

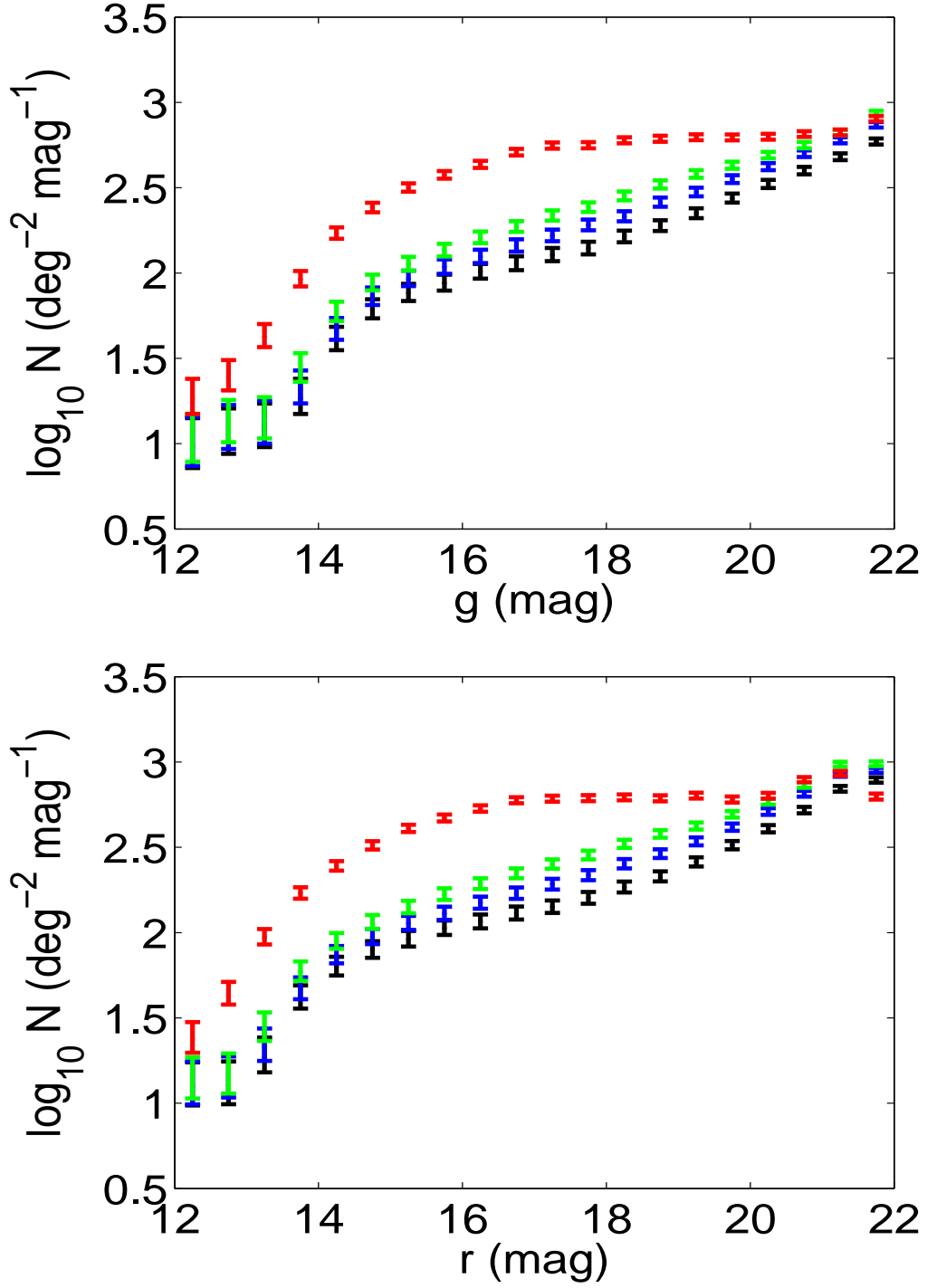


Figure 2.6: De-reddened g (top panel) and r (bottom panel) magnitude distributions of the NGP (black), and some lower latitude fields (blue for $b = 75^\circ$, green for $b = 65^\circ$, red for $20^\circ \leq b \leq 30^\circ$) fields selected from the SDSS DR7 photometric database. The bins of this luminosity function are the logarithmic star numbers per 0.5 mag. The assumed Poisson error bars are also indicated.

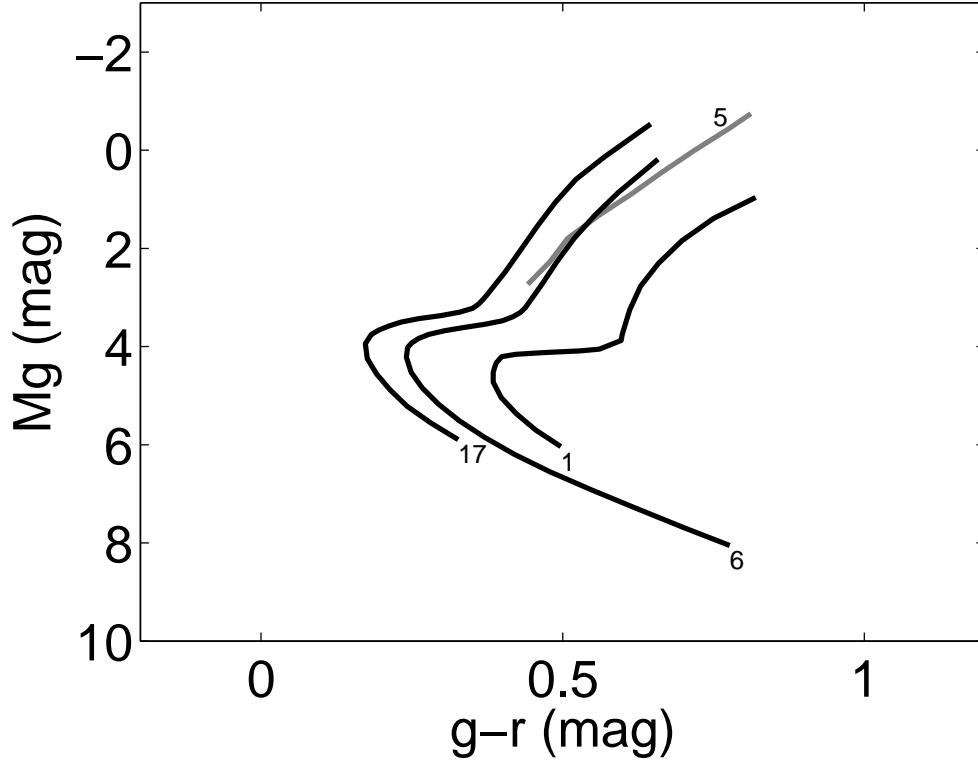


Figure 2.7: The fiducial isochrones of three globular clusters based on de-reddened absolute magnitude M_g and intrinsic color index $(g - r)$. The CMDs of four of 17 clusters are plotted and labeled. The 1st, 5th, 6th and 17th clusters in Table 2.2 with the metallicities $[\text{Fe}/\text{H}] = -0.73, -1.52, -1.54$ and -2.29 , respectively, are plotted in the CMD from right to left. These CMDs display the isochrones of stellar populations with the specific metallicities. These three isochrones as examples of 17 clusters cover the full range of cluster metallicity observed by SDSS. The corresponding turn-offs are from $(g - r)_0 = 0.17 \dots 0.38$ mag. The 5th (in gray color) and 6th clusters have the similar metallicities, which results that their isochrones are close to each other.

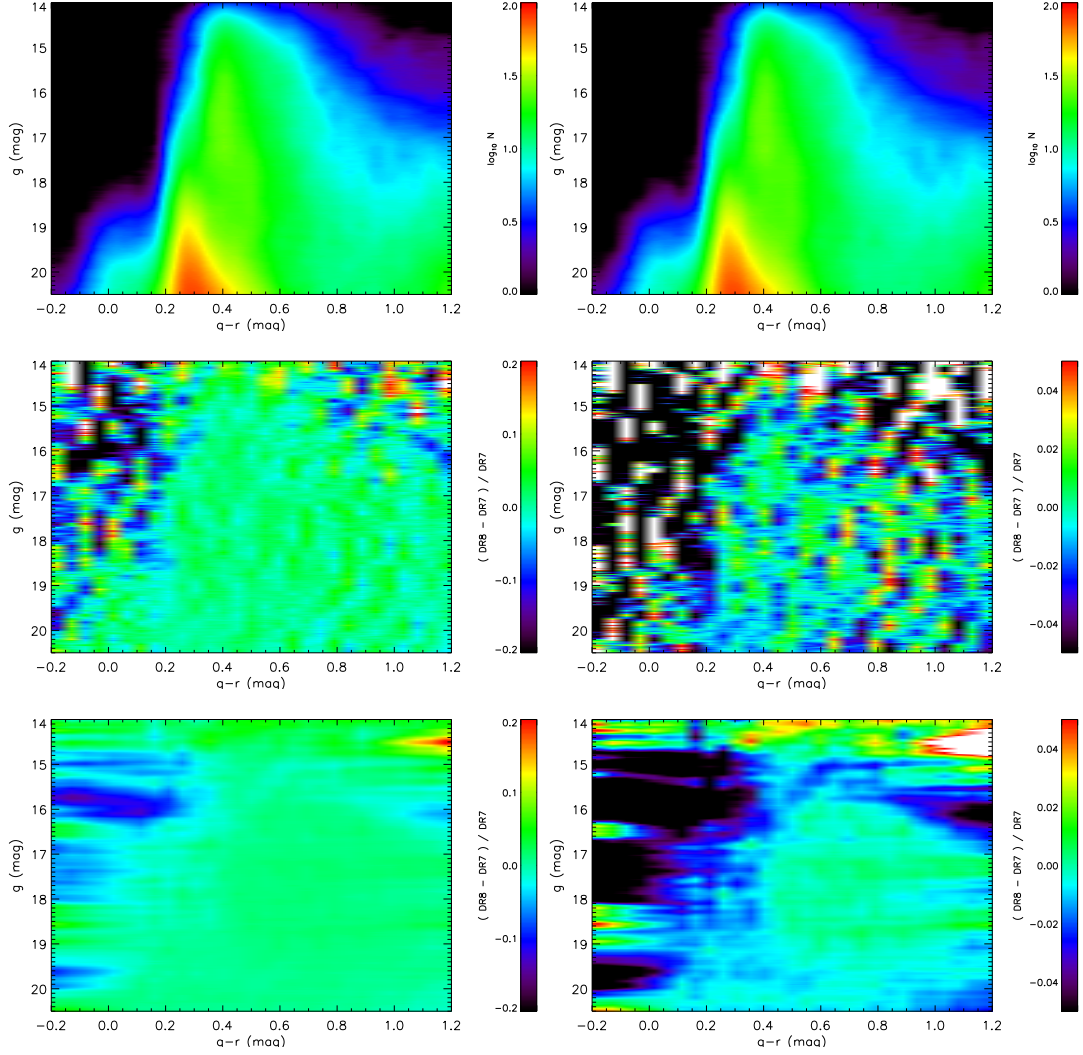


Figure 2.8: The top row shows CMDs of DR7 and DR8 at the NGP field respectively. The middle panels indicate the relative difference distributions between DR8 and DR7 in 20% and 5% scales respectively. And the bottom panels are the smoothed relative difference distributions in 20% and 5% scales respectively. The smoothing filter sizes are 0.1 mag in g axis and 0.05 mag in $g - r$ axis to smooth out the difference of photometric errors of DR7 and DR8.

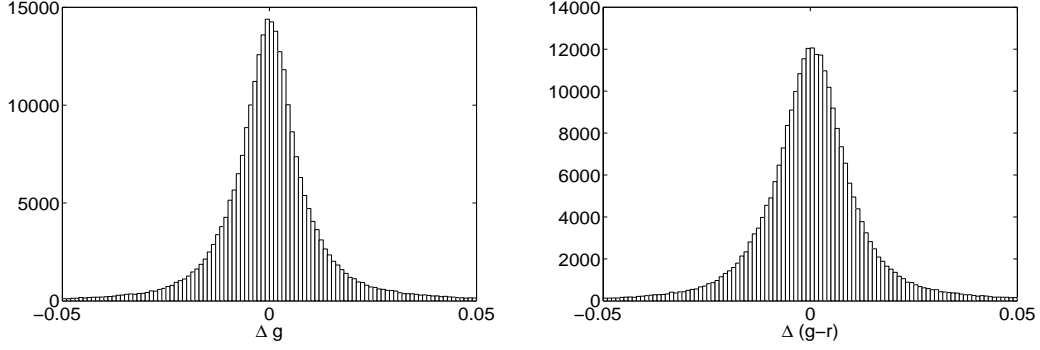


Figure 2.9: The distributions of differences of g and $g-r$ in DR7 and DR8. the left panel shows the difference of g magnitude in DR7 and DR7 and the right panel shows the difference of $g-r$ in DR7 and DR8. The significant Gaussian profile suggests that the difference of magnitudes and colors between DR7 and DR8 is from a random statistical process of the calibration pipeline.

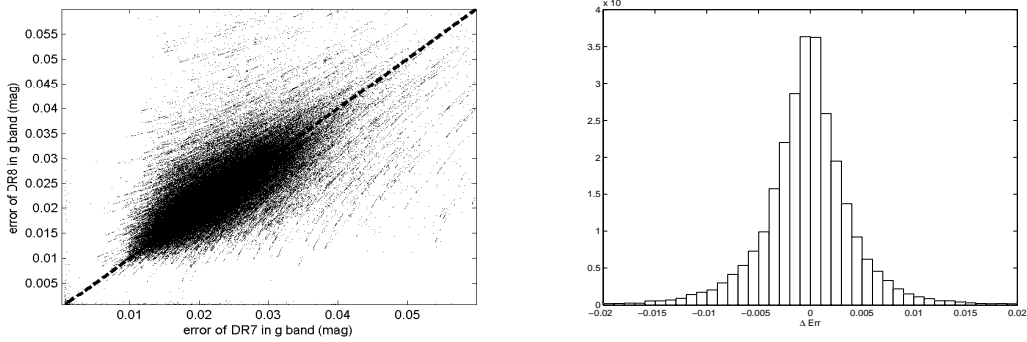


Figure 2.10: The left panel shows the relationship of photometric errors between DR7 and DR8. The dashed line is the case of unity (equivalence of the errors in the two data releases). The black dots are distributed around this line which means the errors of DR8 have not been improved yet. The right panel shows the distribution of photometric errors in DR8.

*“Perhaps it doesn’t matter who you are,
what you are doing is more important.”*

Prof. Dr. Biwei Jiang, 2003

3

Models

A series of Galactic star count models were presented in recent years. In this chapter we describe the basic properties of the four models used for comparison with the SDSS data. The Just-Jahreiß, TRILEGAL, Besançon, and Jurić models provide different points of view to look at the structure and the evolution of stellar populations of the Milky Way. The TRILEGAL and Besançon models allow ones to easily generate a simulated stellar catalogue of the volume of interest, and the Jurić model is based on fitting of SDSS photometric data directly. The Just-Jahreiß model was developed in order to improve the vertical structures of the thin and thick disks for the consistent predictions of star counts and the kinematics. The Just-Jahreiß model can reproduce best observations of a specified volume. The TRILEGAL model produces a mock stellar catalogue using a pre-defined scale height function of thin disk, IMF, and SFR. The Besançon model is able to simulate a large field with a set of sub-populations of thin disk quickly. The Jurić model is determined by the simple fitting of the SDSS observations. These different scopes provide the chance to check the effects of different methods in the case of simulating NGP of the Milky Way. The observational data are described in Chapter 2.

3.1 Just-Jahreiß model

Just & Jahreiß (2010) presented a local disk model (the Just-Jahreiß model). As a self-consistent disk model, the Just-Jahreiß model is created with a self-gravitating potential and the AVR described by vertical velocity dispersion σ_w in the Jeans equation. As the input functions the SFR and the AVR produce stellar sub-populations of disk in the vertical direction. The components described by dynamical equations include stellar disks (the thin and thick disks), gas layer, and dark matter, which are indicated as s , t , g , h in Just & Jahreiß (2010).

3.1.1 Isothermal sub-population

The Besançon model contains seven sub-populations in the thin disk. Unlike that, Just & Jahreiß (2010) divided the thin disk into a series of continuous sub-populations with own ages, vertical dispersions, and scale heights. The thin disk is composed of a continuous series of isothermal sub-populations characterized by the SFH and the AVR. A distinct isothermal thick disk component with older age is added. The vertical density profiles $\rho_{s,j}(z)$ of all sub-populations j are determined self-consistently in the gravitational potential $\Phi(z)$ of the thin

disk, thick disk, gas component, and dark matter halo. Adopting dynamical equilibrium leads to

$$\rho_{s,j}(z) = \frac{g(\tau_j)\text{SFH}(t_j)dt}{2h_d(\tau_j)} \exp\left(\frac{-\Phi(z)}{\sigma_w^2(\tau_j)}\right) \quad (3.1)$$

with a (half-)thickness h_d , a vertical velocity dispersion σ_w determined by the AVR, and the parameter g to account for mass loss by stellar evolution. The time t and age τ are connected by the total disk age $t_p = t + \tau = 12$ Gyr. The potential $\Phi(z)$ and the thicknesses $h_d(\tau_j)$ are determined iteratively. The density profiles of the MS stars are calculated by adding the profiles of the sub-populations accounting for their respective MS lifetimes. In a similar way the thicknesses and the velocity distribution functions of MS stars are derived as a function of lifetime.

The thick disk is considered using an oldest single population with an age of ~ 12 Gyr (10 Gyr for model C, details in Chapter 3.1.3). This means that the thick disk has a larger scale height and velocity dispersion than those of the thin disk. Similarly, for the thin disk component, gas is taken into account using gravitational force and dynamical relationship. The dark matter halo is approximated near the mid-plane (small z) with a one dimensional Poisson equation. The self-consistent profile of the isothermal thick disk can be fitted by

$$\rho_t(z) = \rho_{t,0} \text{sech}^{\alpha_t}\left(\frac{z}{\alpha_t h_t}\right), \quad (3.2)$$

where the parameters α_t and h_t depend on the velocity dispersion and on the total gravitational potential.

The input parameters and functions take three different properties into account: SFR, AVR, and local vertical velocity W data. We have four different SFR and AVR (Figure 3.1) pre-definitions with different current σ_w values and average surface SFRs. The Hipparcos survey provides a complete sample with velocity data at solar neighborhood. The distribution of the W velocities is used to fit the velocity dispersion profiles $\sigma_{ms}(z)$ and velocity distribution function $f_{ms}(W, z)$ for MS stars constructed by isothermal sub-populations of the thin disk.

The SFH and the AVR are the main input parameters, which are to be determined as a pair of smooth continuous functions. For each given SFH the AVR is optimized to fit the velocity distribution functions of MS stars in V band magnitude bins in the solar neighborhood. A metal enrichment law is included, which reproduces the local G dwarf metallicity distribution for the right MS lifetimes and luminosities. Additionally a consistent IMF can be determined, which reproduces the local luminosity function. In Just & Jahreiß (2010) four different solutions with similar minimum χ^2 but very different SFHs were discussed.

We describe the basic framework of the model of Just & Jahreiß (2010). Four models (A, B, C, and D) with different SFR and AVR definitions reproduce different density profiles at vertical direction of the Galactic plane. The thin disk is divided into a set of sub-populations with different age bins. Each sub-population has its own age and vertical density profile.

In “model A” the SFH is given by the star formation rate as a function of time, $\text{SFH}(t)$:

Table 3.1: Parameters of the Just-Jahreiß model A.

Quantity	Unit	Model A Fiducial	Model B Min. χ^2	Model C Const. SFR	Model D $\tau = 10$ Gyr
$h_{d,\text{eff}}$	pc	400	389	357	398
$\rho_{d(\odot)}$	$M_{\odot}\text{pc}^{-3}$	0.037	0.037	0.037	0.037
$\Sigma_{d(\odot)}$	$M_{\odot}\text{pc}^{-2}$	29.4	28.6	26.3	29.2
form	-	$\rho_t \sim \text{sech}^{\alpha_t} \left(\frac{z}{\alpha_t z_t} \right)$			
α_t	-	1.16	1.17	1.60	1.13
h_t	pc	800			
$\rho_t(\odot)$	$M_{\odot}\text{pc}^{-3}$	0.0022	0.0023	0.0022	0.0023
$\Sigma_t(\odot)$	$M_{\odot}\text{pc}^{-2}$	5.3	5.7	5.4	5.8
[Fe/H]	dex	-0.7			
age	Gyr	12	12	12	10
form	-	$\rho_h \sim \left(R^2 + \frac{z^2}{b^2} \right)^{\alpha_h/2}$			
α_h	-	-3.0			
b	-	0.7			
$\rho_h(\odot)$	$M_{\odot}\text{pc}^{-3}$	0.00015			

Note: Main components: thin and thick disks and stellar halo (top to bottom). The scale height of the oldest sub-population of the thin disk $h_{d,\text{eff}}$ is the maximum one. The α_t and α_h are power indexes of the thick disk and halo. The ρ and σ with subscripts d, t, h are the local density and local surface density of each component. The scale height and metallicity of the thick disk are fixed to 800 pc and -0.7 dex, respectively.

$$\text{SFH}(t) = \langle \text{SFH} \rangle \frac{(t + t_0)t_n^3}{(t^2 + t_1^2)^2}$$

with $\langle \text{SFH} \rangle = 3.75 M_{\odot}\text{pc}^{-2}\text{Gyr}^{-1}$, $t_0 = 5.6$ Gyr, $t_1 = 8.2$ Gyr, and $t_n = 9.9$ Gyr. The vertical velocity dispersion is given by

$$\sigma_w(\tau) = \sigma_e \left(\frac{\tau + \tau_0}{t_p + \tau_0} \right)^{\alpha}$$

with $\sigma_e = 25 \text{ km s}^{-1}$, $\alpha = 0.375$, and $\tau_0 = 0.17$ Gyr. The density profiles of each sub-population are calculated self-consistently. The exponential scale height and thickness are increasing with mean age of the population. The total thin disk density profile is characterized by a scale height of 270 pc and a thickness $h_{d,\text{eff}} = 400$ pc.

3.1.2 Constrains of kinematics

The stellar sample within a 25 pc sphere around the Sun from the Hipparcos Catalogue (Gliese 1988) is used to determine the distribution of vertical velocities $f(W)$. Another independent sample from McCormick K and M dwarfs (Vyssotsky 1963) also are used for that. The sample is divided into a few bins with own age ranges using a constant SFR assumption (Jahreiß & Wielen 1997). The vertical velocity dispersion of each bin is determined. The distance of sample is limited within 25 pc and the V magnitude is restricted to stars brighter than 7.3 mag. The bins are selected as $M_V = -1 \pm 1.5, 1 \pm 0.5 \dots 6 \pm 0.5, 8 \pm 1.5$ mag. The bin with magnitude fainter than 7.5 mag is provided by Catalog of Nearby Stars, 4th edition (CNS4).

The selection range in CMD is determined by the MS isochrones from the Padua models (Bertelli et al. 1994; Girardi et al. 2002). The absolute magnitude of the zero age main sequence (ZAMS) $M_{V,ms}$ is calculated using the Padua isochrone program (<http://stev.oapd.inaf.it/cgi-bin/cmd>). The final sample includes all stars in the magnitude range $M_{V,ms} \pm 0.8$ mag. We adopt the peculiar motion of the Sun of $W_\odot = 7$ km/s which is consistent with the value (7.17 ± 0.38) km/s determined by Dehnen & Binney (1998) from Hipparcos data.

3.1.3 Density profile and metallicity

The vertical density profile of each sub-population of the thin disk can be determined by the kinematics constraints and the Poisson equation. The isolated isothermal sub-population should display a sech^2 profile. The actual profiles are in-between an exponential and sech^2 law. The sum of all sub-populations is the total density profile of the thin disk.

We adopt a simple analytic metal enrichment law as the age metallicity relation (AMR):

$$[Fe/H](t) = 2.67[O/H](t) = 2.67 \lg(Z_{oxy}(t)),$$

and

$$Z_{oxy}(t) = Z_{oxy,0} + (Z_{oxy,p} - Z_{oxy,0}) \frac{\lg[1 + \ln(1 + q(t/t_p)^\lambda)]}{\ln(1 + q)},$$

where q , r , and the initial and present $[Fe/H]$ for model A, B, C, and D are as follows:

$$\mathbf{A} \quad q = 2; r = 0.55; [Fe/H]_0 = -0.6; [Fe/H]_p = 0.02,$$

$$\mathbf{B} \quad q = 2; r = 0.55; [Fe/H]_0 = -0.6; [Fe/H]_p = 0.02,$$

$$\mathbf{C} \quad q = 2; r = 0.55; [Fe/H]_0 = -0.6; [Fe/H]_p = 0.02,$$

$$\mathbf{D} \quad q = 2; r = 0.55; [Fe/H]_0 = -0.6; [Fe/H]_p = 0.02,$$

where the $[Fe/H]_0$ is the initial $[Fe/H]$ and the $[Fe/H]_p$ is the present $[Fe/H]$.

3.2 TRILEGAL

One of main goals of the TRILEGAL model is the simulation of Milky Way star counts in several photometric systems. For that purpose, Girardi et al. (2002) developed a detailed method to convert theoretical stellar spectral libraries to photometrically measurable luminosities. The authors can produce these transformations routinely for any new photometric system, such as the five-color filters of the SDSS (Girardi et al. 2004). The TRILEGAL model has been used to predict stellar photometry in different systems. For calibration and comparison, a few surveys have been simulated such as Chandra Deep Field South (CDF-S, Groenewegen et al. 2002), Deep Multi-color Survey (DMS, Hall et al. 1996), 2MASS, the Southern Galactic Pole (SGP as observed by the ESO Imaging Survey (EIS) (Prandoni et al. 1999; Zaggia et al. 1999)), and Hipparcos.

Being able to simulate both very deep and very shallow surveys is one of the most difficult goals in the TRILEGAL model. As for the shallower samples like the Hipparcos data, MS, red giant branch (RGB) and red clump stars with partly very low number statistics need to be generated. On the other hand, for more sensitive surveys an extended lower-luminosity MS, which reaches down to $M_V \sim 30$ mag corresponding to stellar masses of $M \sim 0.1 M_\odot$ as well as old white dwarfs need to be included.

Most subroutines of TRILEGAL can be divided into two main parts. The first part was developed by Girardi (1996) and is used for interpolating and searching for parameters of a given mass, age, or metallicity in stellar theoretical evolutionary tracks. These routines were designed for recent work such as creating theoretical isochrones to simulate the CMDs of nearby galaxies. Recently, a second group of routines was developed as a tool to deal with synthetic photometry. Girardi et al. (2002) converted between intrinsic stellar properties and observable magnitudes.

At the moment, there are four main elements in TRILEGAL's approach:

1. A set of theoretical stellar evolutionary tracks used to calculate of isochrones that can be processed before submitting a job is included;
2. The library of synthetic spectra is essentially the same one as described in Girardi et al. (2002), but is now complemented with white dwarf spectra. The spectra of most stars were computed with the Kurucz (1992) code, which covers T_{eff} from 50,000 K down to 3,500 K (O to early M-type stars) and metallicities $[M/H]$ from +0.5 to -2.5 dex. For stars with higher effective temperature than 50,000 K black-body spectra are adopted. For all dwarfs cooler than 3,900 K down to 500 K the BDdusty1999 code (Allard et al. 2000) is applied. Fluks et al. 1994 and Finley et al. 1997 are used as empirical spectra of M giants and all white dwarfs of DA type respectively;
3. For the prediction of star counts in different bands, the parameters of the photometric system were determined (Johnson-Cousins-Glass, HST/WFPC2, HST/NICMOS, Washington, and ESO Imaging Survey filter sets as described in Girardi et al. (2002); and for the Sloan Digital Sky Survey *ugriz* system as given in Girardi et al. (2004));

4. Then, the star counts are calculated for a small patch on the sky from parameterized density distributions of the Galactic components.

3.2.1 Input sets

The tables of evolutionary tracks as a function of initial mass (M_i), stellar age (τ) and metallicity (Z) provide parameters such as bolometric magnitude M_{bol} , effective temperature T_{eff} , surface gravity g , core mass, and surface chemical composition.

The stars are subdivided into four subgroups with different mass ranges. For masses between $0.2 M_\odot$ and $7 M_\odot$ (first subgroup), the TRILEGAL model uses the tracks of Girardi et al. (2002). The evolutionary range extends from the zero-age main sequence (ZAMS) to the thermally pulsing asymptotic giant branch (TP-AGB) (or a maximum age of 25 Gyr for lower-mass stars) and metallicities between $[M/H] = -1.7$ dex ($Z = 0.0004$) and $+0.2$ dex ($Z = 0.03$). The second subgroup contains MS stars with masses from $0.2 M_\odot$ to $0.01 M_\odot$. It includes very low mass stars and most of the brown dwarfs with dusty atmospheres (Chabrier et al. 2000).

The MS is going down to $\lg(L/L_\odot) = -5$, $T_{eff} \sim 916$ K, but covers only solar metallicity, which is adopted as the standard value of all stars. The third subgroup includes post-AGB stars and white dwarfs with a stellar initial mass between 0.6 and $5 M_\odot$. These tracks commence at the end of the TP-AGB phase. The last subgroup contains stars with masses higher than $7 M_\odot$, where the method of Bertelli et al. (1994) is applied, and covers also metallicities of $Z = 10^{-4}$ and 10^{-3} .

The stellar parameters are calculated by linear interpolation of the parameter grid in TRILEGAL. The input parameters stellar mass, age, and metallicity are transformed to the independent variables $\log(m)$, $\log(t)$ and $[M/H]$ in log-scale for all tracks. The wavelength-dependent bolometric corrections BC_{λ_i} are taken from a theoretical library (Girardi et al. 2002). The photometric magnitudes are computed by an integral over the spectrum weighted by the detector's transmission function.

The IMF $\phi(M)$ is a crucial ingredient in Galactic modeling, because it determines the relative number of stars with different photometric properties and lifetimes. For comparison and convenience, the IMF is normalized to one solar mass: $\int_0^\infty M\phi(M)dM = 1 M_\odot$. Its default shape is a log-normal function in TRILEGAL following Chabrier (2001):

$$\phi_M \propto M \exp\left[-\frac{(\lg M - \lg M_0)^2}{2\sigma^2}\right],$$

whose parameters are $M_0=0.1 M_\odot$ and a dispersion of $\sigma = 0.627$. Two segmented IMF power-laws (Salpeter 1955; Kroupa 2001) and an IMF in exponential forms (Larson 1986) have been included as well and can also be chosen in the TRILEGAL interface.

The above relationships are used only for populations consisting of single stars. The TRILEGAL model does, however, also account for binaries if desired: If the option “binary” is turned on, the following approximation is adopted: for each primary star with mass M_1 that star has a secondary star with probability f_b . The secondary star has a uniform mass ratio distribution in the range $[b_b, 1]$. With $f_b = 0.8$ and $b_b = 0$, for example, 80 percent of all

stars have a secondary star and the masses of the secondary stars are chosen from a uniform distribution between 0 and M_1 . The default parameters are $f_b = 0.3$ and $b_b = 0.7$.

The function $\psi(t)$ describes the SFH. For old components the shape of the SFH is not well constrained, because the observed star counts are quite insensitive to it. For the thin disk the SFH has not yet been safely determined (e.g., Aumer & Binney (2009); Just & Jahreiß (2010)). The interface allows only the choice between a constant SFH up to 11 Gyr and a two-step SFH with 1.5 times enhancement between 1 and 4 Gyr.

The age-metallicity relation (AMR) is also important for the Galactic model. The AMR affects the stellar CMDs. For the thin disk, the abundances of Rocha-Pinto et al. (2000) are adopted in TRILEGAL,

$$[\text{Fe}/\text{H}] = -0.10\tau/\text{Gyr} + 0.44,$$

with a default scatter in metallicity of 0.2 dex.

There are five Galactic components in TRILEGAL: thin disk, thick disk, halo, bulge, and an extinction layer in the disk.

Thin disk: The mass density decreases exponentially with Galactocentric radius R projected onto the plane of the disk,

$$\rho_d = C_d \exp(-R/h_R) f(z),$$

where $f(z)$ is the vertical density profile. It is either an exponential $\exp(-|z|/h_d)$ or a squared hyperbolic secant $\text{sech}^2(0.5z/h_d)$ function. According to stellar dynamics, a sech^2 density profile corresponds to an isothermal and isolated self-gravitating disk. The Galactic thin disk is not isothermal, because the scale height h_d is a function of stellar age and the thin disk is not isolated. The typical height of the disk sub-populations depends on stellar age as described by

$$h_d = z_0 \left(1 + \frac{\tau}{t_0} \right)^\alpha \quad (3.3)$$

with the initial scale height z_0 , timescale t_0 , and power-law index α as free parameters. This relation shows that stars are formed very close to the plane and disperse vertically later. C_d is normalized by the local surface density,

$$\Sigma_d(\odot) = \int_{-\infty}^{+\infty} \rho_d(r_\odot) dz \int_0^\tau \psi_d(t) dt.$$

Thick disk: The density can be described as a double exponential or vertically with a sech^2 form similar to the thin disk. But h_t is not a function of stellar age because the thick disk is predominantly an old population.

The SFH is constant over an age range of 11–12 Gyr with metallicity $[\text{Fe}/\text{H}] = -0.73 \pm 0.1$ dex and α enhancement of $[\alpha/\text{Fe}] \sim 0.3$.

Halo: Its mass density ρ_h follows a de Vaucouleurs $r^{1/4}$ law (de Vaucouleurs 1948) and allows a spheroidal flattening (Gilmore 1984). The density profile of the halo can be approximated as follows (Young 1976):

$$\rho_h(s) \propto \exp(-b \cdot j) \cdot j^{-3.5}, \quad (3.4)$$

for $s = r/r_{\text{eff}} > 0.1$, where $j = s^{1/4}$, r_{eff} is the effective radius, and $r^2 = R^2 + z^2/q_h^2$ with oblateness q_h .

The SFH is constant over an age range of 12—13 Gyr and there are two choices for the metallicity distribution. We fix the metallicity to $[\text{Fe}/\text{H}] = -1.6 \pm 1$ dex with a corresponding α enhancement of $[\alpha/\text{Fe}] = 0.3$.

Bulge: The bulge has not yet been calibrated well in the TRILEGAL model, because of too few constraints from observations. Since the bulge does not contribute to high Galactic latitude data considered in this thesis, we are not discussing the parameters further.

Extinction: We are not using the dust extinction model in TRILEGAL. Instead we compare star counts with de-reddened observational data as described in Section 2.

3.2.2 Interface and procedure

In 2005 the code was frozen and the TRILEGAL interface was released on the web after recalibration. It has since been complemented with additional photometric systems. Version 1.4 is online ¹ since June of 2009 and accessible for external users now. The maximum available sky area that can be simulated covers 10 deg² so far and users can choose among more than 40 different filter systems. The TRILEGAL model is currently the most convenient star count simulation interface available.

A set of parameters and functions is chosen and submitted by the user. The output data file can be downloaded directly after a few minutes. As the input data, evolutionary tracks are converted to isochrones of different age intervals. And then the SFR and AMR data generate global “perfect” photometric data using stellar isochrones. In order to simulate observed photometric data, the “perfect” data are degraded by or convolved with the Galactic geometry, photometric limits and filters effects (noise, saturation, incompleteness and effective area).

3.2.3 Calibration and output

For calibration and comparison, a few surveys have been simulated such as CDF-S (Chandra Deep Field South), DMS (Deep Multi-colour Survey by Hall et al. (1996)), 2MASS, SGP (Southern Galactic Pole as observed by EIS (Prandoni et al. 1999; Zaggia et al. 1999)), and Hipparcos.

The TRILEGAL model simulated three fields for calibration and fine tuning. Groenewegen et al. (2002) compared the TRILEGAL model with the CDFS field with five pass-bands ($UBVRI$) for 0.3 deg² and seven pass-bands ($UBVRIJK$) for 0.1 deg². The 90% completeness level of the number counts is reached at approximately $V = 23.5$ mag. Non-stellar objects are eliminated by the Point/Extended (P/E) source classification and the Spectral Energy Distribution (SED). The CDFS field is centered at ($l = 220.0^\circ, b = -53.9^\circ$), which is a relatively empty region with respect to galactic stars. Girardi et al. (2005) presented the magnitude distributions of model and observations in seven different pass-bands. In the B and V bands, the observational star counts are $\sim 87\%$ of the model predictions within a 90 percent completeness limit in Figure 3.3. Because the disk in the model dominates the star counts at $V < 22$

¹ See the web online: <http://stev.oapd.inaf.it/cgi-bin/trilegal>

mag, the discrepancy is caused by an over estimated disk between 18 and 20 mag. By fitting these observations of the CDFS field the simulated densities of the disk and stellar halo can be determined as the default input parameters in the early version of the TRILEGAL model. The discrepancy can be improved greatly when the sample is limited to include the blue sub-sample with a color range $-0.4 \leq B - V \leq 1.2$ (see the right panel of Figure 3.3). That suggests that low mass and red stars are the most important source of significant discrepancy. In fact Girardi et al. (2005) had shown that the simulation would be perfect if the halo stars with $M < 0.2M_{\odot}$ are eliminated.

The DMS (Hall et al. 1996; Osmer et al. 1998) contains 6 different fields of mid-latitude with deep UBVRI photometry. An image area of 0.83 deg^2 was observed with the 4-m Mayall telescope at Kitt Peak National Observatory that reaches $V = 22$ mag deep. Only “star” objects are considered for comparison with TRILEGAL. In general these fields show a good agreement with TRILEGAL’s simulated star counts with the completeness limits given in Figure 3.4. The largest discrepancy appears in field 21 of the DMS and reaches $\sim 10\%$ in stellar numerical density. This is caused by too few stars in the disk. This field 21 ($l = 51.73^{\circ}, b = -39.18^{\circ}$) is located in the inner region of the Milky Way and is effected by Galactic bulge stars.

The SGP field contains a sky area covering 1.21 deg^2 and is centered at ($l = 306.7^{\circ}, b = -87.9^{\circ}$) with 3 pass-bands (BVI) photometry. In the B and V bands, the observational star counts are $\sim 60\%$ of model predictions within the completeness limits given in Figure 3.5. The magnitude range covers 16 to 21.5 mag for all pass-bands. The discrepancies are much larger than for the CDFS and DMS fields. The largest discrepancies occur at $B \sim 17$ mag and $V \sim 18$ mag and reach more than 50% of relative star counts. The SGP field close to near the southern Galactic pole is similar to our target NGP field to study the vertical structure on the Galactic plane. Girardi et al. (2005) cannot improve the large discrepancy at the SGP, improving this discrepancy is one of aims in this thesis.

The output of TRILEGAL resulting from a given submission is a single data file that includes the apparent photometric data in the user-selected filter system and several stellar physical parameters of the populations (see Table 3.2). TRILEGAL does not currently provide any positional information except the stellar distances. Binaries are presented by single entries containing the physical parameters of the primary plus the photometry for the entire system. The photometric output is well-suited for comparison with the SDSS and the other observations. TRILEGAL will be improved at these terms in next versions in the future.

The photometric data can be used directly to make a Hess diagram that is the reference for comparison. Each population (the thin disk, the thick disk and stellar halo) can be presented on a Hess diagram separately. The Galactic component of a star in a specified apparent magnitude-color box at a specified direction is determined by the relative ratio of numerical density of each population of TRILEGAL.

Table 3.2: Header information of an output file of TRILEGAL.

Fields	Physical parameters
Gc	the Galactic component: 1=thin disk, 2=thick disk, 3=halo, 4=bulge, 5=additional object
logAge	log10 of stellar age
[M/H]	initial metallicity respect to the Sun's
m_ini	initial mass in M_{\odot}
logL	log10 of luminosity in L_{\odot}
logTe	log10 of effective temperature in K
logg	log10 of surface gravity in cm/s^2
m-M0	absolute distance modulus
Av	extinction in the V band
m2/m1	mass ratio for binaries (=0 for single stars)
Mbol	apparent bolometric magnitude
(filters)	apparent magnitudes in the several pass-bands
Mact	actual mass in M_{\odot}

Note: The explanation of the header of a TRILEGAL output file. The first column is the parameter name in the header of the output file. The filter names depend on the user-selected photometric system. In this thesis, we fix our photometric system to “SDSS *ugriz*”. The filter fields occupy five columns in the output file and are ordered by *ugriz*. The second column in the table above is the physical meaning and unit of each field of the header.

3.3 Besançon model

The Besançon model (model of stellar population synthesis of the Galaxy by the Besançon observatory) also can obtain a simulated mock data using the web-based interface to compare with the observation data. Figure 3.6 shows the edge-on view of the simulated Galaxy using the Besançon model with six colors *BVRJHK*. The Besançon model adopts a self-consistent method to simulate the structure of disks. But this self-consistent method was not complete consistency, which means that the dynamical equilibrium was approximated by the parameterized heating function and the corresponding density profiles but was calculated by the Poisson equation completely. The seven sub-populations of the thin disk and a population of the thick disk were expressed by the analytical functions with the exponential or power laws.

3.3.1 Internal properties

In Robin et al. (2003) the properties of the Besançon model were described in detail. The web-based version was released in 2004 and last modified in 2009. This web interface is able to create catalogues of pseudo-stars from Monte-Carlo simulations in specified directions and in specified areas with the luminosity limits defined by the user. Users are not able to change

any structural parameters and stellar evolutionary features, which are included in the internal program:

1. Three populations (thin disk, thick disk, spheroid) are included in the NGP direction.
2. Each population is described by a SFH, an IMF, a set of evolutionary tracks, kinematics (AVR), a metallicity (and gradient), and includes a white dwarf population
3. Density profiles of the thin disk are constrained self-consistently by the potential using the Boltzmann equation and are a function of age.
4. The extinction is modeled by a diffuse thin disk. This is not reliable for the Galactic plane where a more sophisticated 3D extinction model should be used instead. The users can include their own extinction distribution along the line of sight.

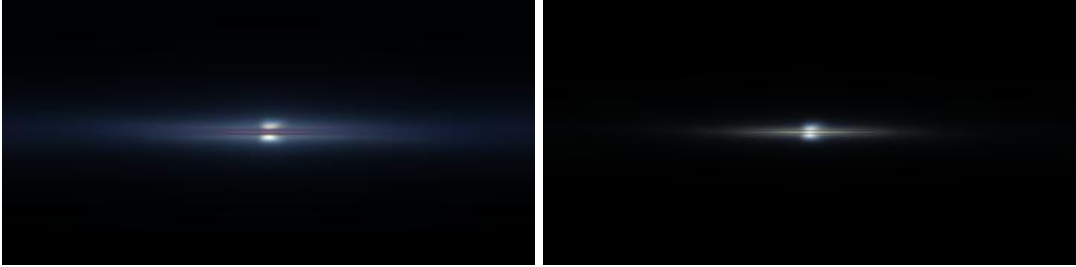


Figure 3.6: Simulated image in 6 colors of the Milky Way as would be seen from the sun. Colors are given by the integrated flux in bands B , V , R (upper panel), J , H , and K (lower panel).

The density profile of the stellar halo is described by a power law with the slope $\alpha = -2.44$ and the oblateness $q_h = 0.76$ (see Equation 4.1). The total local stellar density of the halo is determined by constraints of the IMF in the Besançon model. The value ($9.32 \times 10^{-6} \text{ M}_\odot \text{pc}^{-3}$) is much smaller than in the other models referred to in this article.

Robin et al. (2003) developed a population synthesis approach to simulate the structure and evolution of the Milky Way. The Besançon model is based on different well calibrated data sets and the structural parameters are optimized to reproduce a set of selected fields across the sky. The model was continuously improved and extended by adding additional filter sets. The simulation of each component is based on a set of evolutionary tracks, assumptions on stellar number density distributions, constrained either by dynamical considerations or by empirical data, and guided by a scenario of a continuous formation and evolution of the stellar populations.

Our target is limited to the NGP with a Galactic latitude $b > 80^\circ$. In this volume, stars belonging to the Galactic bulge can be ignored. The stellar populations in the NGP field can be divided in three distinct components: thin, and thick disks and stellar halo. For details of the properties of the Galactic components see Robin et al. (2003).

The Besançon model is able to output photometric data, distances, extinctions, etc. The de-reddened photometric data are our basic catalogue. The catalogue simulations with five color photometric data are considered to be the test of the population synthesis approach. With the NGP field we can test the vertical structure of the Galactic components and the calibration of the underlying isochrones in the filter system.

Using the web interface (<http://model.obs-besancon.fr/>), users can choose one out of two photometric systems either the Johnson-Cousins system or CFHTLS-Megacam as the output. We selected CFHTLS-Megacam as our photometric system to input the simulated volume and magnitude limits. The mock catalogues of thin, and thick disks and halo and of their sum are generated by the Monte-Carlo procedures in different jobs. The stellar number of the sum of the three components is therefore not exactly the same as the stellar number of the general simulation.

The Besançon model is also able to output simulated space velocities, i.e., U , V and W data with errors, to describe the kinematics of the stars. The detailed comparison and analysis of the Besançon model with SDSS data in the NGP field will be discussed in Chapter 6.

3.3.2 Options

First of all, users need to choose one photometric system either Johnson-Cousins or CFHTLS Megacam. Two output methods may be chosen: Catalogue simulations or Tables and differential counts. Users can request the output table with or without kinematics data. Stellar kinematics contain U , V , and W velocities and their errors at local rest system. In the context of this thesis we do not consider the kinematics. And we select the Catalogue simulation to generate the mock catalogue with stellar parameters.

Users cannot change any internal properties (i.e. local density or scale size) so far. We can only input output limits:

- The volume such as distance interval, central coordinate and the area of the field.
- The diffuse extinction law and user-defined absorption clouds.
- Absolute magnitude range: 7 to 20 for the thin disk, 2 to 13 for the thick disk, and 2 to 11 for the spheroid.
- Spectral type and subtype, luminosity class, and population from the youngest disk to oldest halo and bulge.
- Apparent magnitude range for output limits.
- Photometric error of each pass-band using a parabolic or exponential function.

We keep the default values of distance interval (0 to 50 kpc) and ignore the extinction and photometric errors for this thesis because we have obtained de-redden photometric data from SDSS observations, and in order to compare with observation the photometric errors can be smoothed in our boxcar smoothing diagrams.

Table 3.3: Header information of an output file of Besançon.

Fields	Physical parameters
Dist	stellar distance to Sun in kpc
Mv	absolute magnitude in V band
CL	luminosity class (“5”=V and “3”=III etc.)
Typ	
LTef	
logg	log10 of stellar surface gravity
Age	stellar age in
Mass	stellar mass in solar mass
(4 color indexes)	four color indexes
(apparent magnitude)	apparent magnitude
[Fe/H]	Metallicity
l	Galactic longitude
b	Galactic latitude
Av	Total extinction at V band in mag
Mbol	Total bolometric magnitude

Note: The explanation of the header of the Besançon output file. The first column specifies the fields of the header in the output file. The color index names depend on the selected photometric system by the user. In this thesis, we fix our photometric system to “CFHTLS Megacam”. Then the filters fields occupy five columns in the output file and order of $u^*g'r'i'z'$. The second column of the above table is the physical meaning and unit of each field of the header.

The output files of Besançon model contain very rich information. Apart from the list of input parameters and limits, a data file with stellar parameters can be downloaded directly after a notice by Besançon email service.

3.4 Jurić model

In Jurić et al. (2008) a map of the three-dimensional number density in the Milky Way derived by photometric parallaxes based on star count data of SDSS DR6 is presented. Most stars are at high latitudes and cover a distance range from 100 pc to 20 kpc and 6500 deg² on the sky in the sample.

The density distribution in the solar neighborhood is fitted using two exponential disks and the sample implies the existence of an oblate halo. The stellar distances in the sample are determined by the color-absolute magnitude relation of MS stars. The estimated errors of the model parameters are less than ~ 20 per cent and the errors of the scale heights of the disks are less than ~ 10 per cent. By adjusting the fraction of binaries and bias correction, the scale heights of the disks are found to be $h_d = 300$ pc and $h_t = 900$ pc, and the local calibration is

$$\rho_t(\odot)/\rho_d(\odot) = 0.12.$$

Furthermore Jurić et al. (2008) found for the spheroid a best-fit oblateness of 0.64, a power law radial profile of $\rho_h \propto r^{-2.8}$, and a local calibration of $\rho_h(\odot)/\rho_d(\odot) = 0.005$. After subtraction of the smooth background distribution, there are still over-density areas, in particular areas that are explained as tidal streams including the “Virgo over-density” (Duffau et al. 2006) and the Monoceros stream (Abadi et al. 2003).

The solar offset Z_\odot is (25 ± 5) pc or (24 ± 5) pc at the bright and faint end, respectively, which is consistent with the value 24.2 pc adopted by the TRILEGAL model.

The Jurić model is used to calculate a set input parameters for the TRILEGAL model (Set 4 in Chapter 5) in this thesis, since the Jurić model uses the simple parameters space to approximate the stellar background of SDSS observations.

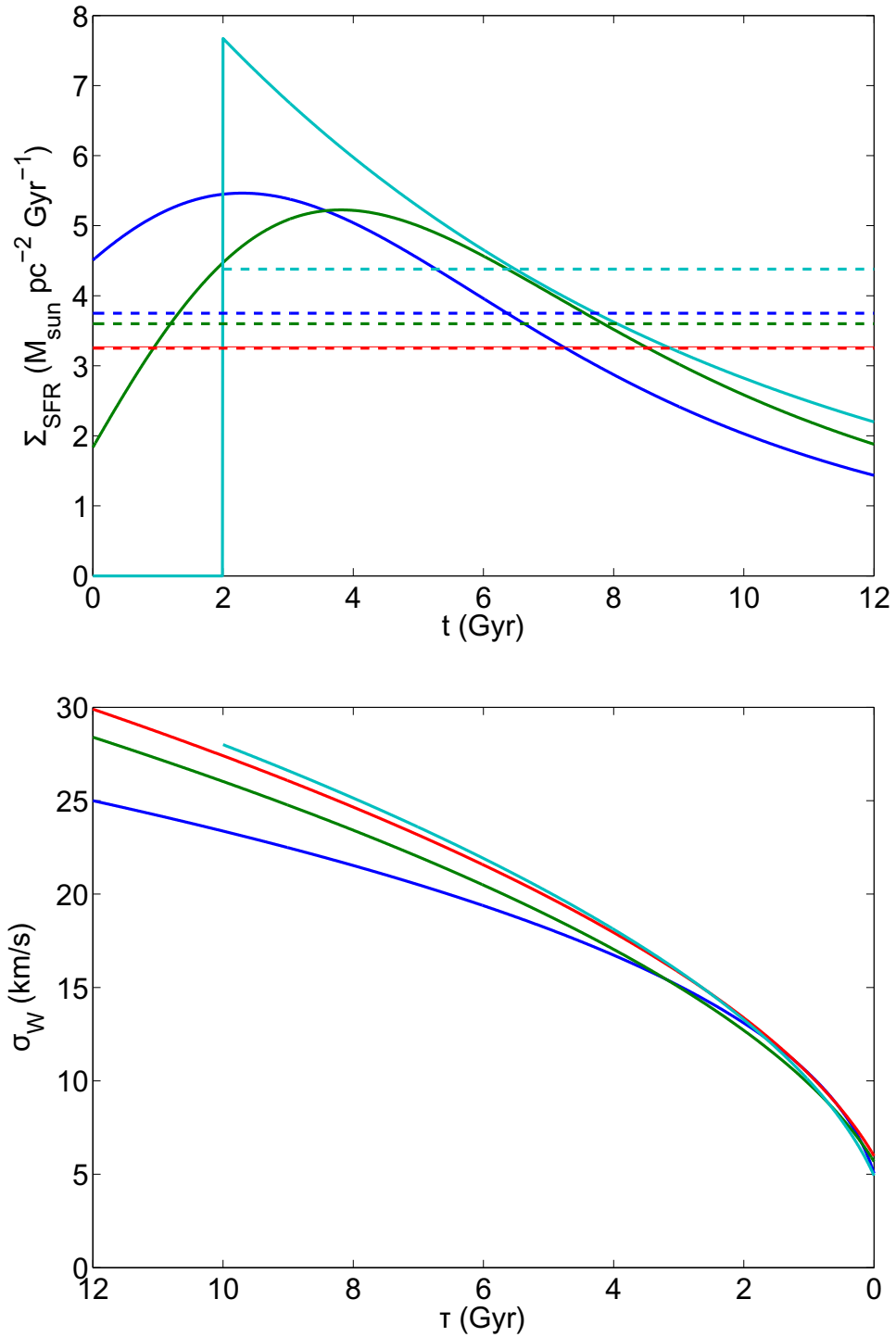


Figure 3.1: The surface SFRs (upper panel) and AVRs (lower panel) of A, B, C, and D in the Just-Jahreiß model. SFRs of the four models A (blue), B (green), C (red), and D (cyan) are illustrated by time functions (solid lines) and average values (dashed lines). The time t is the Galactic evolutionary time until $t_p = 12$ Gyr. The unit of surface SFR is solar mass per square parsec per giga year. The vertical velocity dispersions σ_W of the models A (blue), B (green), C (red), and D (cyan) as the functions of the ages from 0 to 12 Gyr are plotted using the four curves.

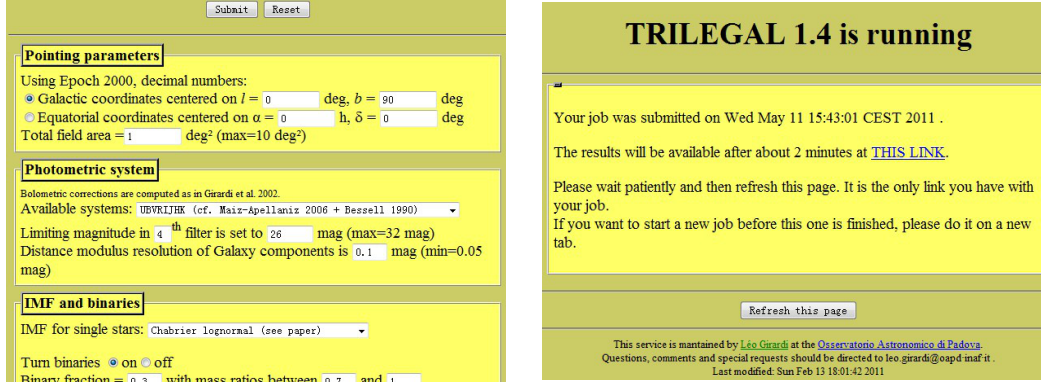


Figure 3.2: Snapshots of the web interface and submitted result of the TRILEGAL model. The web address is <http://stev.oapd.inaf.it/cgi-bin/trilegal>, where you can visit, submit, and download results via a web browser. The left panel is partial snapshot of the user interface for input and the right panel is the result after submitting an input set. The output file will be available within a few minutes.

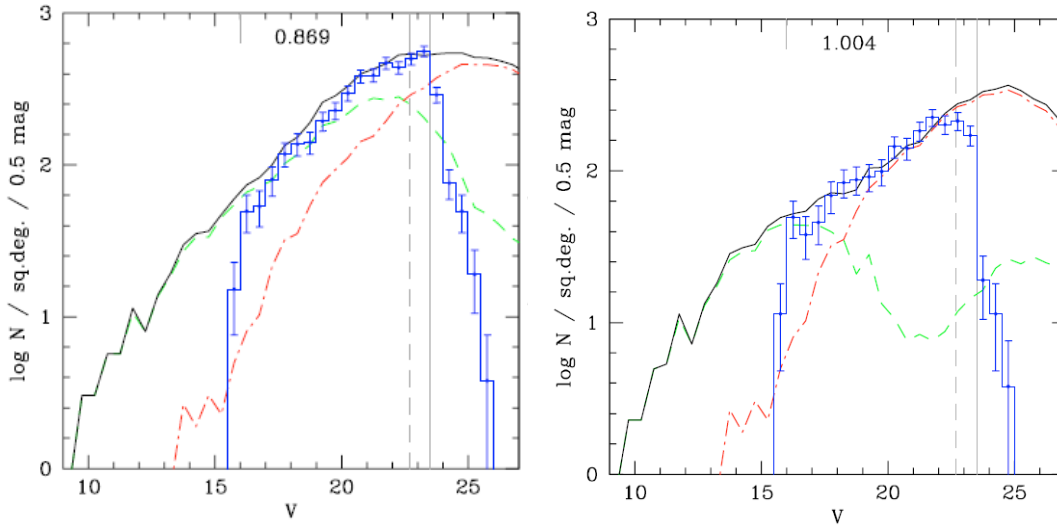


Figure 3.3: The magnitude distribution of the CDFS in the V band as an example. The left panel is the sample with all stars and the right panel is the sub-sample limited in color range $-0.4 \leq B - V \leq 1.2$. The x-axis is the apparent magnitude in V and y-axis is the logarithmic stellar numerical density in square degrees and 0.5 magnitude bin. The simulated disk and halo are presented using green dashed and red dot-dashed lines respectively. The black solid line is their sum and blue stairs with error bars are the observational data from the CDFS field. The number in each panel indicates the relative ratio of observational star counts to the model counts. The figures are cited from the Figure 6 of Girardi et al. (2005).

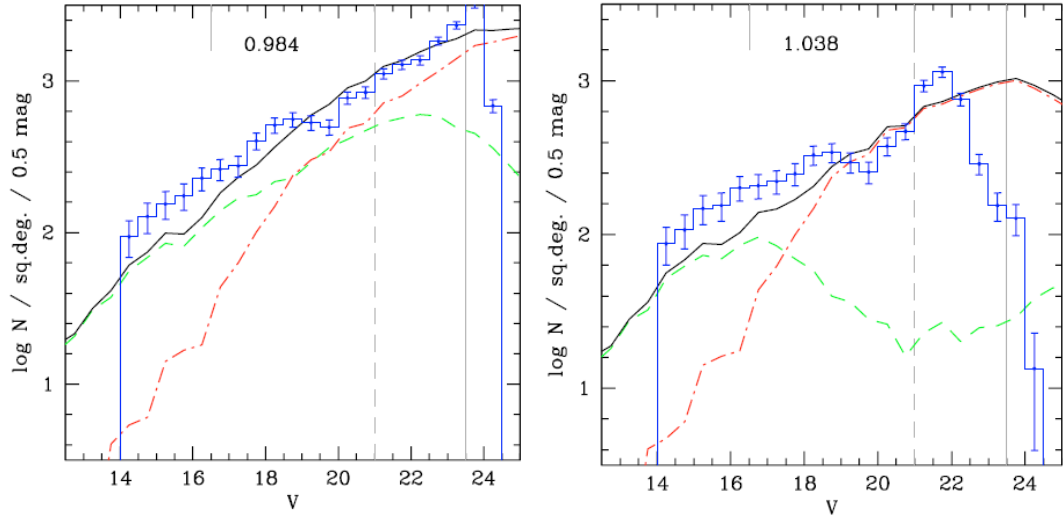


Figure 3.4: Same as Figure 3.3 but for the DMS field. One of 6 fields in the V band is displayed as an example. The figures are cited from Figure 8 of Girardi et al. (2005).

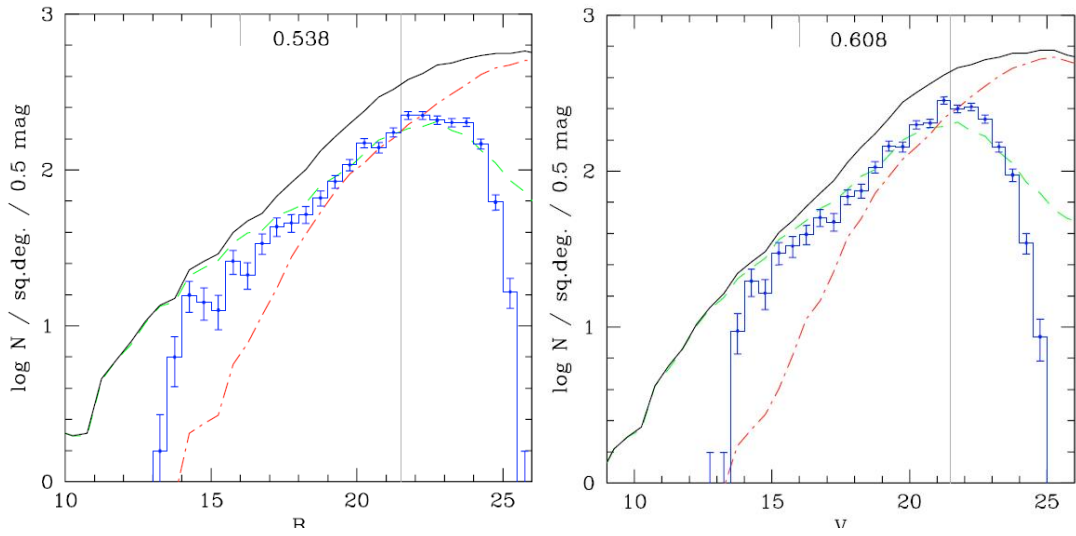


Figure 3.5: Same as Figure 3.3 but for the SGP field. The SGP field in the B and V bands are shown as examples in the left and right panels respectively. The figures are cited from Figure 10 of Girardi et al. (2005).

“If you’re not afraid of the darkness in a planetarium, you could try to learn astronomy.”

My mother, 1986

4

The local Just-Jahreiß model at the NGP field

Just & Jahreiß (2010) presented the Just-Jahreiß Galactic model created by a self-consistent disk structure of the Milky Way. The normalized density profiles of each sub-population of the thin disk and the thick disk were determined by the Jeans and Poisson equations and the fitting of vertical kinematics sample. The self-consistent gravitational potential is calculated from the dynamical self-consistency process. Four models (A, B, C, and D) with different SFRs and AVR as input functions are presented.

In order to constrain the local SFR and AVR in the disk, models should be calibrated by local star counts with a color distribution. The models predict the stellar content with stellar numerical densities of MS the stars in solar neighborhood which can then be compared with observed data at the NGP field. The local star counts of different color bins and the scale height of the thick disk are fitted via Hess diagrams in this chapter. The χ^2 statistics are used to evaluate the quality of the fit of the Hess diagrams.

4.1 Local models

In the case of the Just-Jahreiß model, we adopt a Galactocentric distance of the Sun, R_0 , of 8.0 kpc. The vertical offset of the Sun above the Galactic plane z_\odot is about 20 pc, which is in agreement with literature sources (Girardi et al. 2005; Jurić et al. 2008). The total stellar star count is expressed by the stellar density

$$\rho = \sum_v \rho_v, \quad \text{with } v = d, t, h$$

where d, t, and h indicate the contributions of the thin disk, thick disk, and halo. Star counts are expressed in the Hess diagram with the stellar numerical density

$$N(g - r, g) = \sum_v N_v(g - r, g), \quad \text{with } v = d, t, h$$

where N_v is determined from the isochrones and the distance at each color bin.

4.1.1 Thin disk

The thin disk is the most important component in the local disk model, since its complicated sub-populations are calculated self-consistently. The density profile of each sub-population

has been determined by Just & Jahreiß (2010) from the Jeans and Poisson equations. The magnitude and star count of each distance and color bin are calculated considering the distance modulus and the decrease in the density profile. The trend of decreasing metallicity with increasing height above the Galactic mid-plane of the thin disk is considered to correct the absolute magnitude.

A simple relation

$$\Delta M_g = 0.4 \left(\frac{z}{z + 600 \text{ pc}} \right)^2 \text{ mag},$$

is adopted to approximate the correction of absolute magnitude M_g of the thin disk due to the metallicity of the thin disk, which decreases with increasing height above the Galactic plane. This correction is necessary for all color bins and it is found to be agreement with Ivezić et al. (2008). The corrected absolute magnitude M_g is converted into apparent magnitude g by the distance modulus

$$g = M_g + \Delta M_g + 5 \lg s - 5,$$

where s is the solar distance in units of pc along the line of sight.

According to the profile and pre-specified local density of each sub-population, the star counts $N_d(g-r, g)$ at different magnitude and color bins can be determined. The local star count of each color bin with absolute magnitudes of the local MS can be converted into different densities at different magnitudes according to the distance and density profile.

4.1.2 Thick disk

In order to maintain dynamical equilibrium, the parameters of the thick disk can be changed by the weak potential approximation. Compared with the thin disk, the potential of the thick disk is so small in the local neighborhood that we can adopt the following relationship:

$$\alpha_t z_t \approx \text{constant},$$

where α_t and z_t are the power and scale height of the density profile law of the thick disk fitted by

$$\rho_t(z) = \rho_t(0) \text{sech}^{\alpha_t} \left[\frac{z}{\alpha_t z_t} \right].$$

For a single isothermal population, the power $\alpha = 2$. The power of the thick disk population α_t is between 1 and 2. The actual value is determined by the fit.

For this single stellar population with its velocity dispersion, we adopt a single metallicity $[\text{Fe}/\text{H}] = -0.7$ and age value of 12 Gyr. This matches the fiducial isochrones very well (See the upper panel of Figure 4.1).

4.1.3 Halo profile

In Just et al. (2011) we combined the models of Just & Jahreiß (2010) with the empirically determined photometric properties of the local MS in the *ugriz* filter system. With a best fitting procedure of the local normalization of thin disk, thick disk and stellar halo as a function of color we compared the star count predictions of the different models for the NGP field. In that

procedure we used Equation 4.1.2 to optimize the parameters α_t and z_t of the thick disk and we added a simple stellar halo with a flattened power law density distribution

$$\rho_h(R, z) = \rho_{h,0} \left(\frac{R^2}{R_\odot^2} + \frac{z^2}{q_h^2 R_\odot^2} \right)^{\alpha_h/2} \quad (4.1)$$

with a similar MS as the globular clusters M13 and M3 from An et al. (2008) (See the lower panel of Figure 4.1).

Then the total density of the stellar components at the position (R, z) is the sum of the individual components:

$$\rho(R, z) = \rho_d(R, z) + \rho_t(R, z) + \rho_h(R, z). \quad (4.2)$$

4.2 Simulation of the NGP field

We reproduce the star counts in the NGP field using four Just-Jahreiß models: A, B, C, and D. Model A simulates the best fitting star counts in the NGP field as our fiducial model. Model B has the smallest χ^2 of the fits to the velocity profile of all models. Model C adopts a constant SFR and the age in model D is not 12 Gyr but 10 Gyr. Figure 4.2 displays a schematic diagram to indicate the radial direction and unit volume. For the NGP case, we adopt $(l, b) = (0, 90^\circ)$ with an area of 313.3626 deg^2 for the north polar cap. We ignore the difference caused by the horizontal distribution. Although the Galactic latitude is down to 80° to show the density pattern (Figure 2.2 and 2.3), the scale lengths of disks could be neglected in this case (discussed in Section 2.1.2).

Similar as in Figure 4.2, we put the local star count to some volume element as a function of distance. The spatial density decreases with the density profile of the components. The star count in dV is the density times dV . And the star counts of a series of dV at the direction of line-of-sight are added. The total star count is the sum of each dV which has color distribution. The total star count with a color distribution is our Hess diagram which is we can compare with the data. The local star counts are expanded into three-dimensional space by density profiles. Then the three-dimensional data are projected into two-dimensional space in this process. The local star count of each color bin need to be iterated to find the best fit.

4.3 Fitting process

4.3.1 Local normalization

The Galactic model is represented by star counts which are determined by local star counts and density profiles of three components. The local star counts in each color bin i should be fitted by the data. The stellar contents of the three components is divided into

$$N_{25} = \sum_v N_{25,v}(g-r, M_g), \quad \text{with } v = d, t, h$$

where the subscript 25 stands for the stellar contents in a sphere of 25 pc radius with the volume $V_{25} = 65,450 \text{ pc}^3$.

4.3.2 Algorithm

We constrain the fitting range in order to obtain credible results for the three components. For the thin disk, because the main contribution falls outside the bright saturation limit of the SDSS ($g = 14 \text{ mag}$) $N_{25,s}$ is fixed for $g - r < 0.35$. For the halo, the $N_{25,h}$ is excluded for $g - r < 1.0$ because the main contribution falls outside the fainter limit ($g = 20.5 \text{ mag}$).

We adopt the non-linear Levenberg-Marquard algorithm (LMA, Press et al. (1992)) as our fitting method to deal with the Hess diagram. LMA aims to search the maxima and minima of a function with the form of the sum of a series of squared terms. According to our definition of χ^2 , it allows us to find the minima by the LMA which means the best fitting results for the Hess diagram.

The χ^2 is defined as follows

$$\chi_i^2 = \sum_{gj} \frac{(\lg Y_{ij} - \lg N_{ij})^2}{\sigma_{ij}^2}$$

where the weights are expressed by the reciprocal for data $\sigma_{ij}^2 = \frac{1}{Y_{ij}}$. The total χ^2 is the normalized sum of each color bin i

$$\chi^2 = \frac{A_{\text{NGP}}}{1 \text{ deg}^2} \frac{d(g-r)}{0.1 \text{ mag}} \frac{\Delta g}{1 \text{ mag}} \sum_i \frac{\chi_i^2}{n \times \text{dof}_i},$$

the normalized coefficient is the area of the field, box size of the color and the magnitude, the degree of freedom (dof_i) of each color bin i depends on the fits in g .

The three free parameters $N_{25,s}$, $N_{25,t}$ and $N_{25,h}$ determine the local star count in the solar neighborhood V_{25} . The fitting in each color bin is independent of each other. The total contribution of each component is the sum of $N_{25,s}$, $N_{25,t}$ and $N_{25,h}$. LMA minimizes the χ^2 in each color bin i using Equation 4.3.2 to determine the scale height and power of the thick disk, and the power and flatness of the halo.

4.4 Comparisons and results

The parameters of the halo are fixed for the fitting of disks. Minimum χ^2 value of halo is the power $\alpha_h = -3$ and the flatness $q_h = 0.7$. The size of the magnitude box is 0.5 mag for the models A, B, C, and D. The fitting parameters are listed in Table 4.1. The model A has the minimum reduced χ^2 value among the four models.

We compare the star counts of the Just-Jahreiß model with observations represented by Hess diagrams. The relative difference (data-model)/model are displayed in the second column of Figure 4.3. The relative difference values range from +20% to -20% and are shown in linear scales. The red and black color in the figure stands for lower and higher model values than the

Table 4.1: Parameters of the best-fitting Just-Jahreiß model

Model	Δg	χ^2	N_{25}	($=N_{25,s}$	$+N_{25,t}$	$+N_{25,h}$)	z_t (pc)	α_t
A	0.5	0.33	739.1	696.2	40.2	2.7	800	1.16
B	0.5	0.94	748.0	710.2	35.2	2.6	880	1.07
C	0.5	1.12	810.9	780.3	27.9	2.7	885	1.23
D	0.5	1.18	709.3	680.2	26.4	2.7	930	0.99

Note: The models A-D are fitted by the local normalization. The smoothing Δg is fixed to 0.5 mag. The χ^2 is only for the reduced fit regime. The total local star counts N_{25} are the sum of three components which are of the order of the observed number 726 (Rodgers et al. 2006) or 770 (Chonis & Gaskell 2008).

data, respectively. The green color implies agreement between model and data. The models A, B, C, and D of the Just-Jahreiß model result in different Hess diagrams. Model A is the best match with the data in Hess diagrams.

The analysis of the $(g - r, g)$ Hess diagrams of the SDSS observations and the Just-Jahreiß model is shown in Figure 4.4. The upper left panel shows the predicted star counts with the same coding as the SDSS data in Figure 2.5. The middle left panel quantifies the relative differences (data-model)/model color coded in linear scale. The relative difference between the SDSS DR7 data and this model is less than 10 per cent over most of the CMD. The right panels of Figure 4.4 display the three components of the Just-Jahreiß model.

The largest discrepancies appear in the top-right corner (the white area at $14 < g < 15$ and $0.8 < g - r < 1.2$) in the middle panel of Figure 4.4, because the red giants of the thick disk and halo are not included in the model. The other regions are consistent with discrepancies of less than 5 per cent. The bottom plot shows the χ^2 distribution in log-scale. The values of χ^2 are less than 0.5 over most of the parameter space and the main contributions to the total χ^2 are well distributed over the CMD. The largest discrepancy (blue regime in the Hess diagrams, $0.6 < g - r < 1.1$ and $16.5 < g < 18.5$) is in the transition of thin disk and thick disk. The Just-Jahreiß model does not reproduce the transition between the oldest thin disk and thick disk. A continuous transition between them is impossible because it will add more stars in the model to worsen this discrepancy. An idea to reduce this discrepancy is that the thin disk may have a steeper slope than in the current model above 1 kpc.

The local stellar numerical density of each component is fitted by a Hess diagram of the model with SDSS data. The total fitted stellar numbers in the solar neighborhood of the models A, B, C, and D range from ~ 700 to ~ 800 which is comparable with the observed value $N_{25} = 720$ (Rodgers et al. 2006) or $N_{25} = 770$ (Chonis & Gaskell 2008), which shows that the results of the local total star counts are reasonable.

The simulated luminosity functions in the g and r bands of the model and the SDSS observations are shown in Figure 4.5. Here the number densities are normalized to 1 deg² sky area and 1 mag in luminosity. The number densities of the model are systematically smaller by 0.05 dex compared to the observations.

4.4.1 SFR and AVR

The SFRs of model A, B, C, and D are defined in Figure 3.1. The specific form of SFR is not sensitive to the star counts at the NGP field. However, the χ^2 value of the Hess diagram of each model is able to suggest a lower limit of the SFR. The SFR of model A has relatively large fraction of star formation older than 8 Gyr. In contrast, model D with the smallest current age results in the worst Hess diagram. The χ^2 values of the Hess diagrams of model B and C are in-between A and D. This implies that the SFH should tend to have a large fraction of older star formation.

The model A with maximum velocity dispersion $\sigma_e = 25$ km/s of thin disk is a fully consistent model with the SDSS data at the NGP field. It is the smallest χ^2 value within the models A, B, C, and D. That suggests that the thin disk of model A was the steepest density profile because the scale height of each sub-population depends on the velocity dispersion. In the Hess diagrams, the thin disk of model A shows slightly better agreement with the observational data than the others.

4.4.2 Smoothing and filter conversion

Along the axis of the magnitude g , we provide three different box sizes, $\Delta g = 0.5, 0.2, 0.1$ mag respectively. The comparison between different smoothing sizes helps in two respects: reducing the noise of the Hess diagrams, and testing for possible systematical shifts.

The different smoothing sizes of model A are indistinguishable although smaller Δg produces larger χ^2 caused by more degrees of freedom.

Three different transformations (Jordi et al. (2006), Rodgers et al. (2006), and Chonis & Gaskell (2008)) convert MS stars into SDSS filters. The difference between them is shown in Figure 4.7. The total χ^2 values and the local star counts of the three transformations are similar. There are not any significant differences in their Hess diagrams except small deviations in the regime where the thin disk dominates.

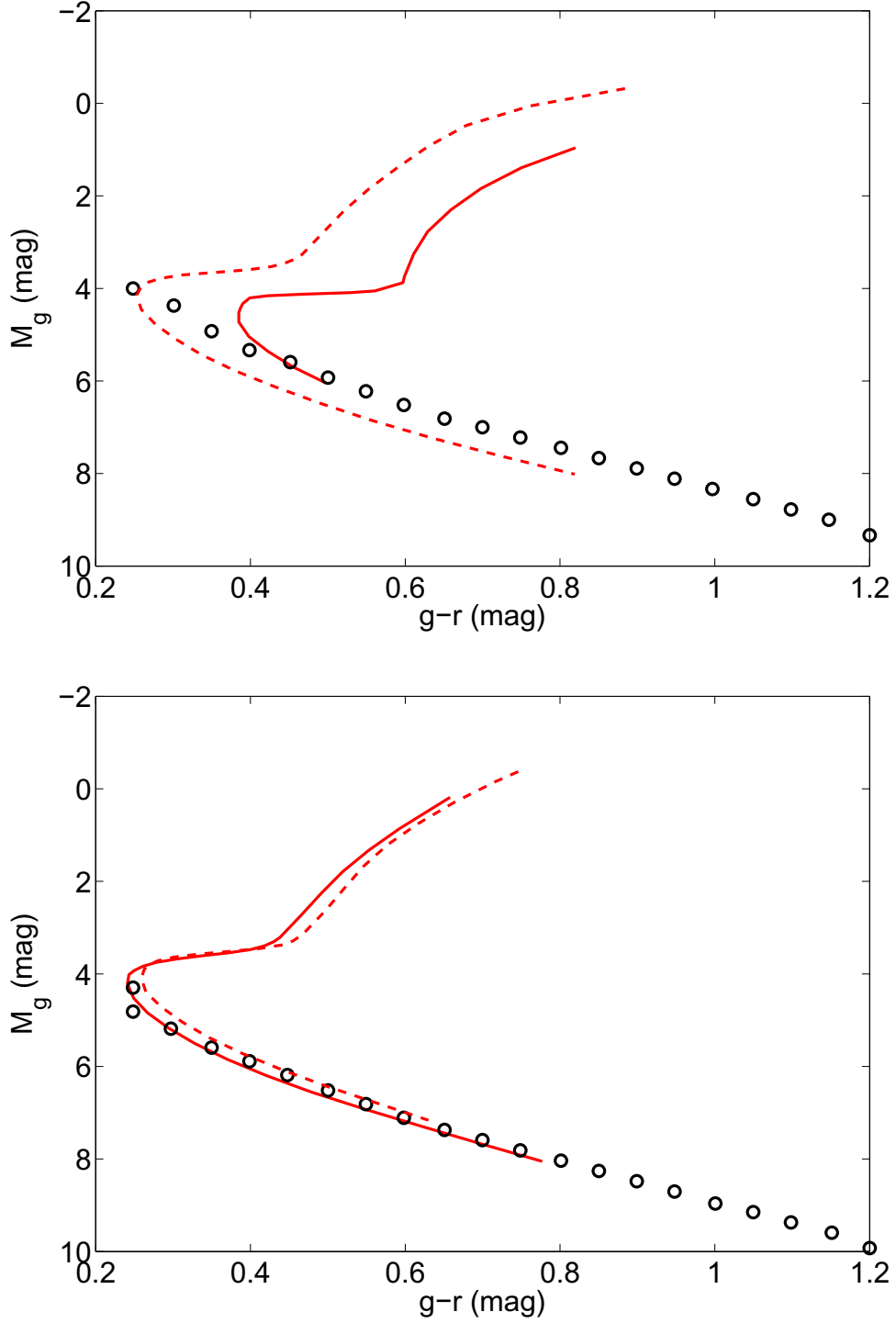


Figure 4.1: The comparison between the thick disk and halo of the Just-Jahreiß model and fiducial isochrones. The upper panel displays the single population of thick disk of the Just-Jahreiß model and isochrones of two globular clusters. Black open circles stand for thick disk model. The red solid and dashed line stand for the globular clusters M71 ($[\text{Fe}/\text{H}] = -0.73$) and M5 ($[\text{Fe}/\text{H}] = -1.27$) respectively. The lower panel shows the halo of the Just-Jahreiß model and the isochrones of two globular clusters: M13 (solid line, $[\text{Fe}/\text{H}] = -1.54$) and M3 (solid line, $[\text{Fe}/\text{H}] = -1.57$). The vertical axis in each panel is the absolute magnitude M_g and the horizontal axis is the de-reddened color index $g - r$.

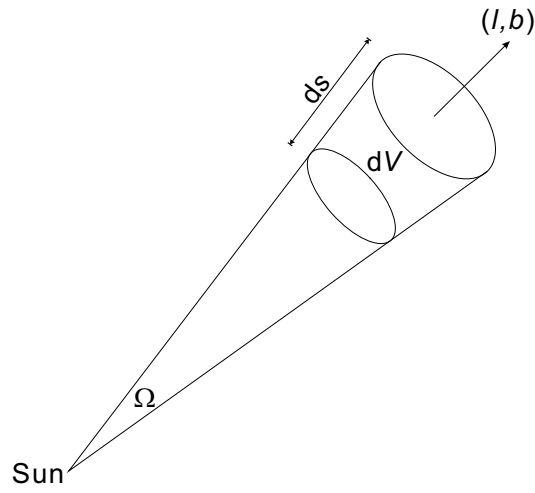


Figure 4.2: A schematic diagram to indicate the radial direction and unit volume. The Sun is our position and Ω is solid angle of the the observed and simulated field pointing the direction (l, b) and contains a series of volume elements dV .

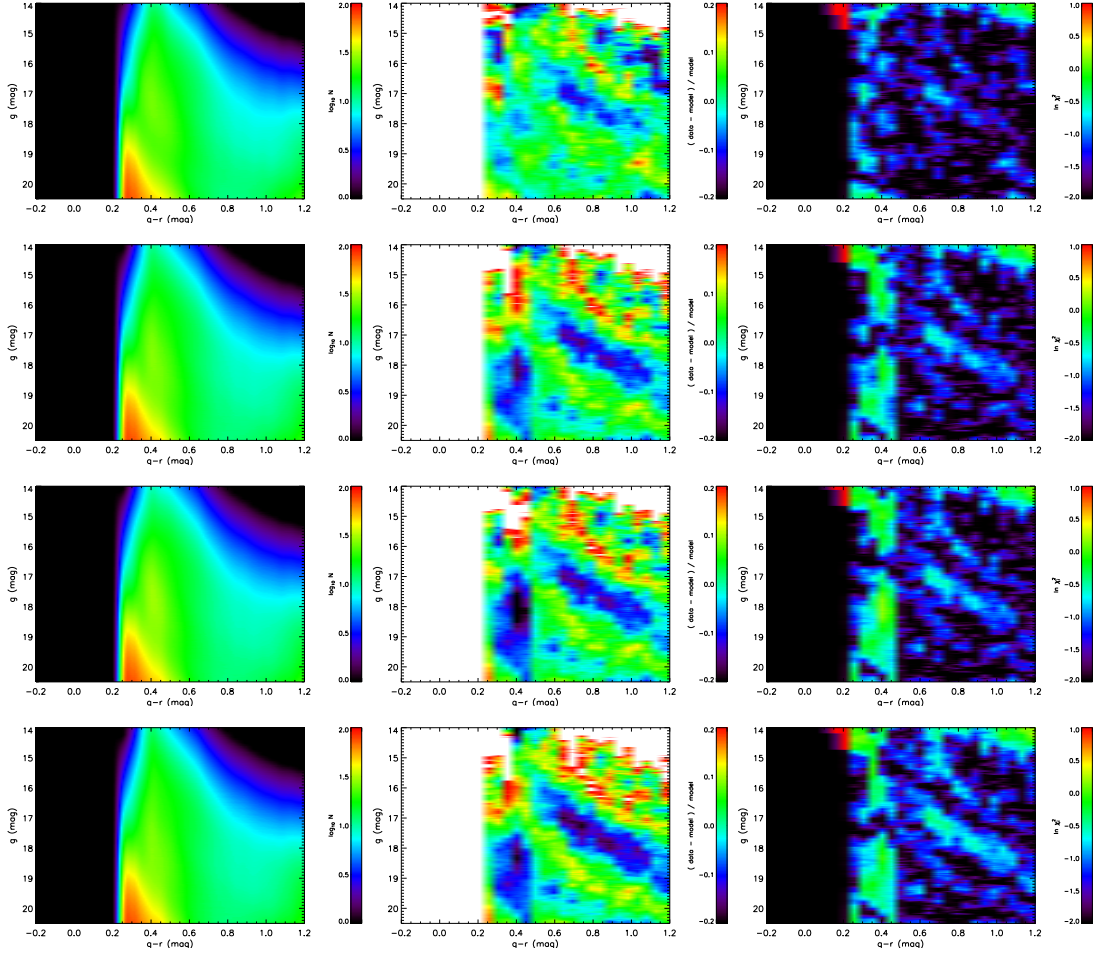


Figure 4.3: The comparison of A, B, C, and D (from top to bottom) of the Just-Jahreiß models. The Hess diagrams of the four models (left panels), the relative difference (middle panels) to SDSS data with range from -20% to +20%, and χ^2 distributions in logarithmic scale (right panels).

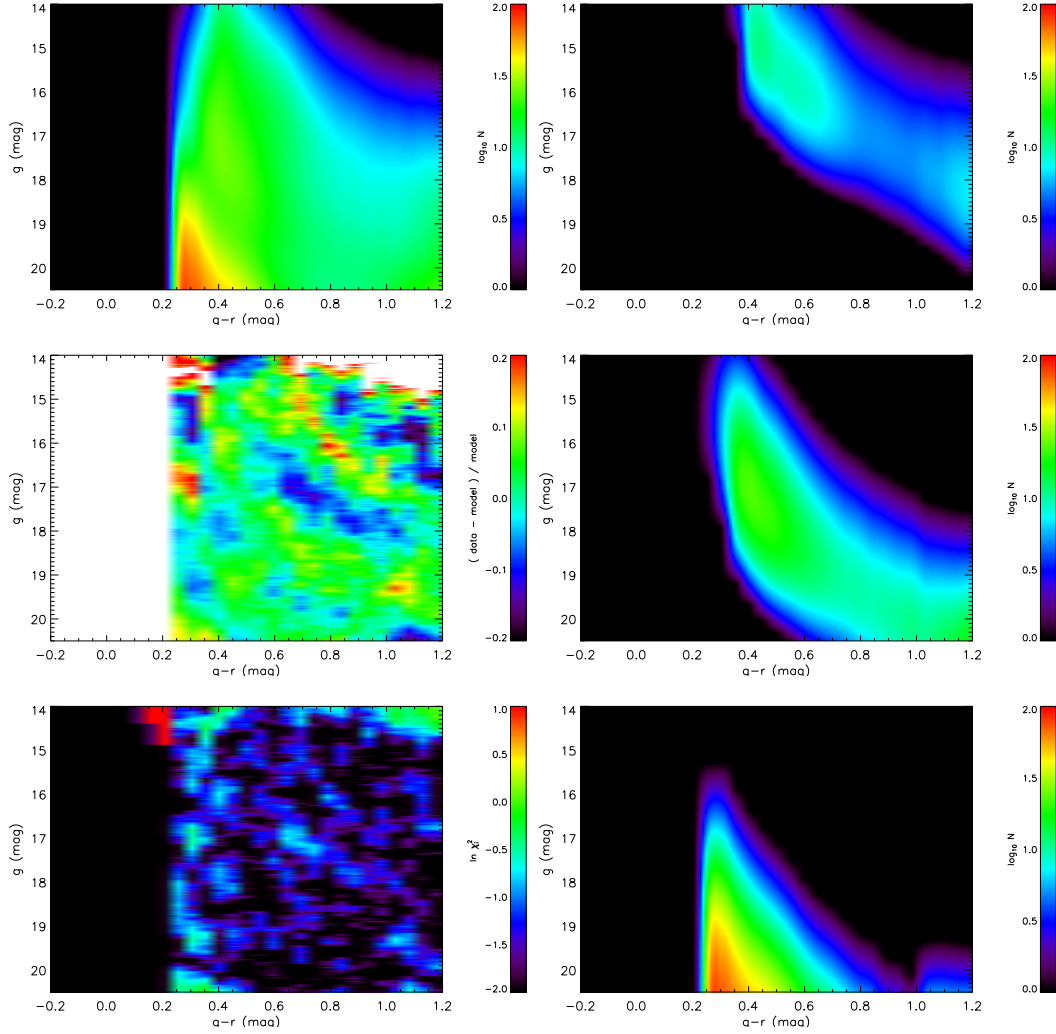


Figure 4.4: Hess diagrams and the comparison between SDSS observations and the best-fitting Just-Jahreiß model. The first panel shows the Hess diagram of the simulation of our best model. The second panel shows the relative difference $(\text{data} - \text{model}) / \text{model}$ between SDSS DR7 star counts and the best model. The color coding covers deviations of ± 20 percent from the model. The last panel is the χ^2 distribution of the difference between model and observations.

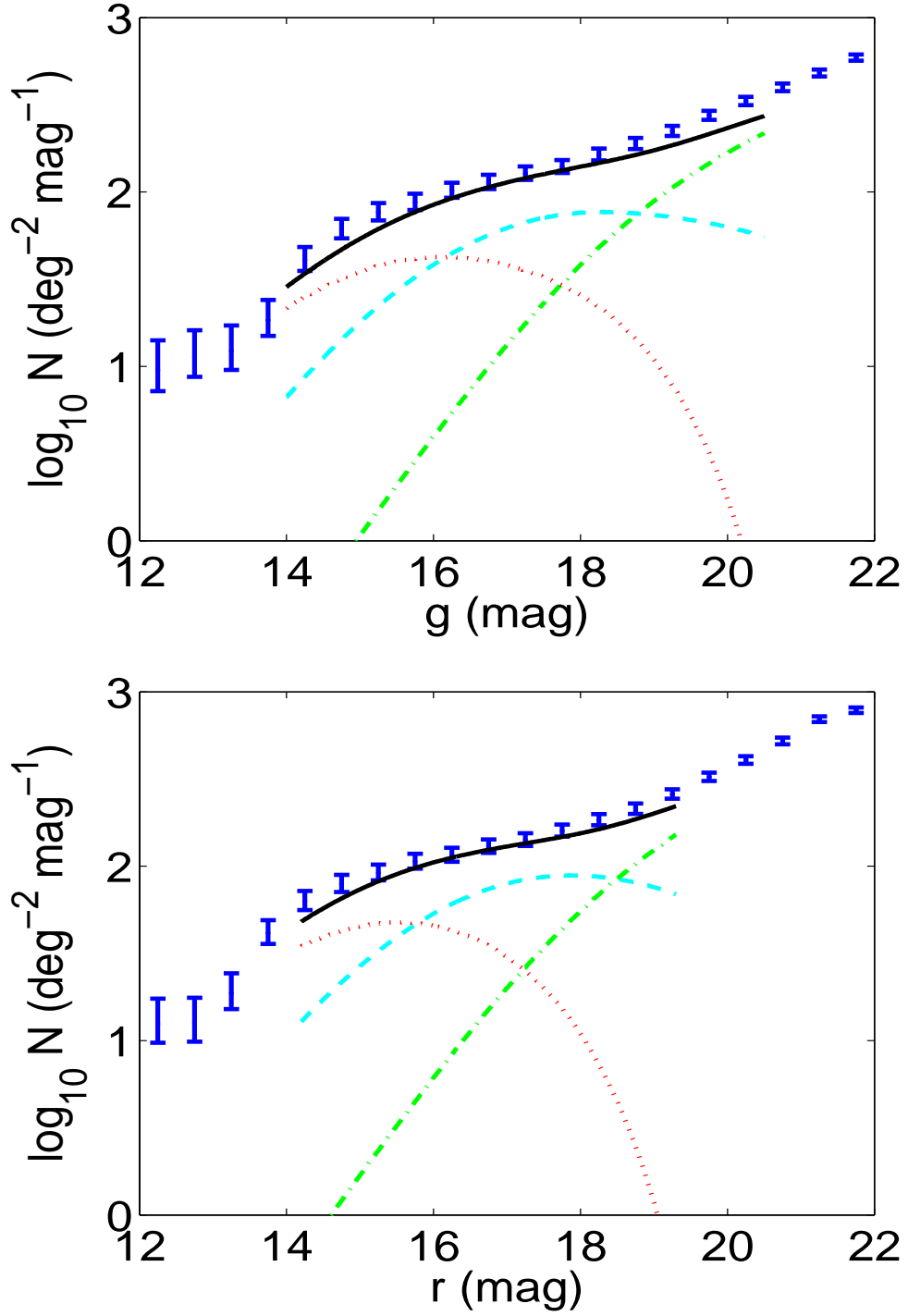


Figure 4.5: The luminosity function of the Just-Jahreiß model (solid black line) and of the SDSS data with error bars (blue) in the g (top) and r band (bottom). Number densities are normalized to 1 deg^2 sky area and 1 mag in luminosity. The dotted (red), dashed (cyan) and dashed-dotted (green) lines represent the thin and thick disks and the halo. The black solid line is their total number density.

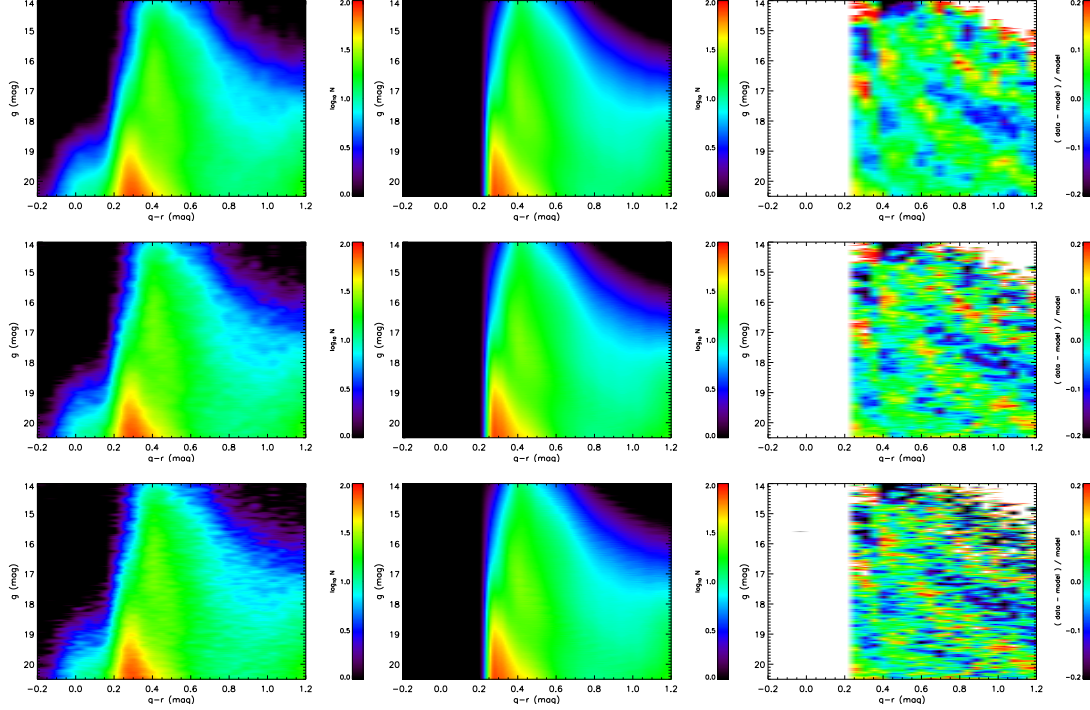


Figure 4.6: Hess diagrams of different smoothing size in the g band magnitude. The box size is $\Delta g = 0.5, 0.2, 0.1$ mag from the top to bottom row. The SDSS data at the NGP field (left column), model A with different Δg (middle column), and the relative difference of Hess diagrams (right column) are displayed respectively. Same color coding as in Figure 4.4.

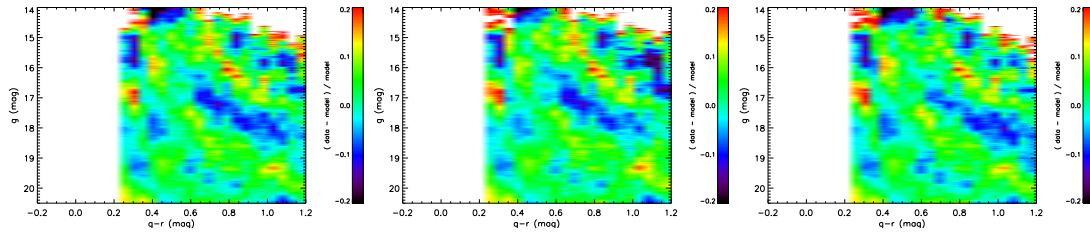


Figure 4.7: The relative differences between models with three different transformations and Hess diagrams. From the left to the right, the three models adopt the photometric transformations of Jordi et al. (2006), Rodgers et al. (2006), and Chonis & Gaskell (2008) respectively.

“Now is no time to think of what you do not have. Think of what you can do with what there is.”

E. Hemingway, *The Old Man and the Sea*
(1952)

5

Simulations of TRILEGAL

TRILEGAL provides a web-based interface to set the structural input parameters. Users can simulate the stellar populations in a specific volume, luminosity range and direction on the sky using different parameter sets. Because the parameter sets and profile shapes are relatively simple and the web-based program returns the result in real-time, we compare TRILEGAL with other models including the Just-Jahreiß, Besançon and Jurić models to find an optimization of input parameters, which is able to simulate a “best” model with minimum χ^2 for TRILEGAL.

There are two aspects of input parameters in the TRILEGAL interface. One aspect is about the structural parameters, such as volume, scale size of each component and photometric limit. The other one is about the internal stellar population parameters including IMF, AVR and SFR. We try to input several different sets (listed in Table 5.2) for the TRILEGAL model to simulate and compare with SDSS observations.

Each simulated photometric catalogue in the TRILEGAL model has a given direction, which is a conical area with a maximum sky coverage of 10 deg^2 . The center of the area can be specified in Galactic coordinates (l, b) or equatorial coordinates (α, δ) . The resolution in magnitudes, Δm , in the TRILEGAL calculation can be modified by the user. The default value is $\Delta m = 0.1 \text{ mag}$ and can be reduced to a minimum of 0.05 mag . Any details with less than Δm will not be presented. The output catalogues of TRILEGAL are based on a random number generator, which allows one to investigate the effect of noise. Therefore the same input parameters cannot generate exactly same catalogue in different submitting. Their statistical results, however, should be consistent with each other. We collect simulations of more areas in order to stack them for improvement of the random errors.

Since the maximum sky area is much smaller than the observed field (313.36 deg^2 for the NGP field), we generate catalogues for 37 different sight lines (Table 5.1) to cover the NGP field. We stack all the star counts and then normalize to star counts per deg^2 to reduce the random errors of the simulations. Each submission creates a “job” in the TRILEGAL interface. We run 37 jobs for each input set listed in Table 5.1.

We fix some parameters and input functions in the TRILEGAL web interface for each job in order to facilitate the comparison with the observational data. We fix the IMF to Chabrier’s log-normal IMF (Chabrier 2001) and use the default binary distribution with a binary fraction of 0.3 and a mass-ratio range of 0.7—1. The solar Galactic cylindrical coordinate is $(R_\odot, z_\odot) = (8000, 24.2) \text{ pc}$ and we fix the SFH for the thin disk to be constant. For the other input parameters in TRILEGAL we selected the five sets of parameters as given in Table

Table 5.1: The central Galactic coordinates of 37 selected fields simulated using TRILEGAL for comparison with SDSS observations.

b (deg)	l (deg)
90	0
87	0, 60, 120, 180, 240, 300
84	0, 30, 60, 90, 120, 150, 180, 210, 240, 270, 300, 330
81	0, 20, 40, 60, 80, 100, 120, 140, 160, 180, 200, 220, 240, 260, 280, 300, 320, 340

5.2. The “Set 1” parameters in this table are from the default input of TRILEGAL in the web interface, “Set 2” is best adjusted to the Just-Jahreiß model (Just & Jahreiß 2010), “Set 3” to the Besançon model (Robin et al. 2003), “Set 4” to the Jurić model (Jurić et al. 2008), and the optimized “Set 5” is discussed in Section 5.3). The other models have very different functional forms than the TRILEGAL model. They are fitted to match the form of the TRILEGAL model, therefore some parameters (such as local density value) are slightly different than their original values and the profiles are not same as in the real original models.

Basically it is difficult to find the “best” input set for the components with a lot of parameters by using the web interface interactively, since the transitions of the thin to the thick disk and of the thick disk to the halo in the CMD are not known a priori. We cannot search independently for the best-fitting parameters in each component. Therefore we first test the parameters of the default model and those that reproduce best the other three Milky Way models. Because in TRILEGAL we have to choose between either an exponential or a sech^2 shape of the disk profiles, the best fitting values with minimum χ^2 are adopted as the input for the TRILEGAL simulations in each case. Based on these results we derive an optimized parameter set (Set 5) by fitting sequentially the halo, thick disk, and then the thin disk parameters.

At colors bluer than $g - r = 0.2$ mag, the SDSS data are unreliable and all selected models cannot generate sufficient stars in that regime. Therefore the mean χ^2 value $\langle \chi^2 \rangle$ of the reduced color regime $0.2 < g - r < 1.2$ is treated as the standard to determine the quality of the model. The values $\langle \chi^2 \rangle^*$ and $\langle \chi^2 \rangle^\star$ stand for the full color range and for partial regime of $0.2 < g - r < 1.2$, respectively, are listed in Table 5.2.

Table 5.2: The sets of input parameters in TRILEGAL and the χ^2 values of the Hess diagram comparisons.

Quantity	Unit	Set 1 Default	Set 2 Just-Jahreiß input	Set 3 Besançon input	Set 4 Jurić input	Set 5 Optimization
$\langle\chi^2\rangle^*$	-	3.52	3.69	3.26	3.11	2.66
$\langle\chi^2\rangle$	-	1.94	2.74	2.65	1.76	1.33
z_0	pc	95.00	60.64	13.61	300.00	90.00
t_0	Gyr	4.4	0.7118	0.02016	-	4.4
α	-	1.6666	0.7576	0.5524	0	1.3
$h_{d,\max}$	pc	767	506	443	300	459
$\rho_d(\odot)$	$M_\odot \text{pc}^{-3}$		0.0297	0.030	0.029	
$\Sigma_d(\odot)$	$M_\odot \text{pc}^{-2}$	59.00	49.36	25.20	17.40	50.00
form	-	sech ²	sech ²	exp	exp	sech ²
h_t	pc	-	793	910	900	750
$\Omega_t(\odot)$	$M_\odot \text{pc}^{-3}$	-	0.0044	0.0015	0.0034	0.0014
$\Sigma_t(\odot)$	$M_\odot \text{pc}^{-2}$	-	7.08	2.82	6.12	4.2
form	-	-	exp	exp	exp	sech ²
r_{eff}	pc	2800	11994	39436	18304	22000
q_h	-	0.65	0.65	0.71	0.59	0.61
$\Omega_h(\odot)$	$M_\odot \text{pc}^{-3}$	0.00015	0.000158	0.00009	0.000145	0.0001

Note: Columns 1 and 2 list the parameters of each Galactic component in TRILEGAL and their units. Columns 3 to 7 list the adopted values of the five input sets for TRILEGAL. Set 1 is the default input of the web-based TRILEGAL interface. Set 2, 3 and 4 are from TRILEGAL fits form with three models: Just & Jahreiß (2010), Robin et al. (2003) and Jurić et al. (2008). Set 5 (the last column) lists our best input set determined by the optimization based on the results of Sets 1 to 4. We provide two mean χ^2 values of the Hess diagram comparisons of the five input sets: $\langle\chi^2\rangle^*$ is with all stars covering the full colour range in the Hess diagram and $\langle\chi^2\rangle$ is only for stars with $0.2 < g - r < 1.2$. The scale height parameters of the thin disk h_d and the local thin disk's density $\rho_d(\odot)$ as well as the surface density $\Sigma_d(\odot)$ are listed. h_t is the scale height of the thick disk. $\rho_t(\odot)$ and $\Sigma_t(\odot)$ are the locally calibrated volume and surface densities of the thick disk. r_{eff} is the effective radius of the halo along the major axis with an oblateness q_h . $\Omega_h(\odot)$ is the local volume density of the halo.

Figure 5.1 shows the vertical density profiles of thick disk and halo for the different sets for comparison. There are significant differences between the models even in the distant regime. The distant regime dominates the star counts in the Hess diagram. This will be discussed further below.

The color-absolute magnitude diagrams of Sets 2 to 4 are plotted in Figure 6.1. The clusters M5 ($[\text{Fe}/\text{H}] = -1.27$) and M71 ($[\text{Fe}/\text{H}] = -0.73$) are used to provide fiducial isochrones of the thick disk (see An et al. 2008). The other three clusters NGC 4147, M3 and Pal 5 with metallicities $[\text{Fe}/\text{H}] = -1.83$, -1.57 and -1.41 , respectively, are used to provide fiducial isochrones of the halo whose metallicity is assumed to be -1.6 (Girardi et al. 2005). The consistency between the model and the fiducial isochrones for the location of the MS and the turn-off implies that stellar population synthesis of TRILEGAL is satisfactory to predict the dominant contribution to star counts. However there are some systematic deviations concerning the location of the giant branches of the stellar isochrones.

5.1 Default (Set 1)

The default input of TRILEGAL is adopted directly as Set 1. The parameters are listed in Column 3 of Table 5.2. The default Set 1 has no thick disk. For the vertical structure pointing to the NGP, Set 1 simulates star counts using thin disk and halo only.

The top row of Figure 5.3 shows the luminosity functions in the g and r band of the SDSS data and of the models in the color range $0.2 < g - r < 1.2$. The default model (Set 1) fits the data very well in the selected magnitude range 14 to 20.5 mag.

In the CMD the picture is different. We construct a Hess diagram similar to the observed Hess diagram in Figure 4.4. Figure 5.5 shows the analysis of the Hess diagram. The upper panel shows the simulated Hess diagram of Set 1, which we compare directly to the observed Hess diagram. The lower panel shows the relative differences (data-model)/model with a color-coded range of ± 50 per cent. The χ^2 distributions of Set 1 to 4 in log-scale are plotted in Figure 5.9. From the relative differences some clear features can be identified (lower panel of Figure 5.5):

1. The large white “island” in the middle of the diagram is a consequence of the lack of a thick disk in the model.
2. The missing stars at the top-right corner of $g - r \sim 1.1$ and $g \sim 15$ mag are a hint of an underestimation of the local thin disk density due to the strongly flattened sech^2 profile.
3. The underestimated number counts at the faint blue end of $0.2 < g - r < 0.4$ and $g > 19.5$ mag show that the halo density profile falls off too steeply.
4. At the faint end ($0.15 < g - r < 0.25$ and $15 < g < 19$) the stars missing in blue colors (halo) are compensated by too many (or slightly too blue) M dwarfs of the thin disk.
5. The horizontally adjacent black and white colored areas in the color range $0.15 < g - r < 0.45$ at $g \sim 17$ mag show that the (thick disk) population is replaced in the model by a

more metal poor (halo) population with a bluer F-turnoff range. This is an additional strong evidence that a thick disk component with intermediate metallicity is missing in the model.

The value $\langle\chi^2\rangle = 1.94$ is significantly larger than that of the Just-Jahreiß model ($=0.055$, Table 3.1).

A comparison of Figures 5.3 and 5.5 shows that the analysis of the luminosity function integrated over a large color range alone may result in misleading conclusions on the underlying stellar populations.

5.2 Fitting of Set 2, Set 3, and Set 4

5.2.1 Just-Jahreiß input (Set 2)

For Set 2, which is based on the Just-Jahreiß model, we derived a best-fit TRILEGAL profile of the thick disk to the sech^{α_t} profile. Both the exponential and the sech^2 form are fitted, thus both

$$\rho_t(z) = \rho_t(\odot) \exp\left(-\frac{z}{h_t}\right) \quad (5.1)$$

and

$$\rho_t(z) = \rho_t(\odot) \text{sech}^2\left(\frac{z}{2h_t}\right). \quad (5.2)$$

The exponential form results in $\chi^2 = 4.0 \times 10^{-8}$, which is a better fit than the sech^2 profile with $\chi^2 = 6.6 \times 10^{-8}$. Therefore we use the exponential profile. The scale height of the thick disk is 793 ± 6 pc and the local density is $0.0029 \pm 0.000015 \text{ M}_{\odot} \text{pc}^{-3}$. The derived local surface density of the thick disk is $\Sigma_t(\odot) = 4.63 \text{ M}_{\odot} \text{pc}^{-2}$.

The scale height of the thin disk is a function of age with the parameters z_0 , t_0 , α (Equation 3.3). The parameters are determined by fitting the non-linear Just-Jahreiß model relationship of the thin disk (see Table 5.2). We fit the thin disk parameters of the Just-Jahreiß model in exponential and sech^2 form, respectively, with the following results:

$$\rho_d(z) = (0.0339 \pm 0.00026) \exp\left(-\frac{z}{270 \text{ pc}}\right) \text{ M}_{\odot} \text{pc}^{-3} \quad (5.3)$$

or

$$\rho_d(z) = (0.0297 \pm 0.00017) \text{sech}^2\left(\frac{z}{543 \text{ pc}}\right) \text{ M}_{\odot} \text{pc}^{-3}. \quad (5.4)$$

The latter fit results in a smaller χ^2 (namely 4.7×10^{-6}) than the former one (8.3×10^{-6}). Therefore we choose the sech^2 form as the profile of the thin disk. The derived local surface density of the thin disk is $\Sigma_d(\odot) = 32.26 \text{ M}_{\odot} \text{pc}^{-2}$, which is 10 percent larger than the surface density of the thin disk of the Just-Jahreiß model.

The halo of the Just-Jahreiß model is fitted by the TRILEGAL form using Equation 3.4. The best-fit parameters are local density $\rho_h(\odot) = 0.001576 \text{ M}_\odot \text{pc}^{-3}$, oblateness $q_h = 0.65$ and effective radius $r_{\text{eff}} = 11994 \text{ pc}$.

In order to take into account the estimated total local density of all stars ever formed, the input values in TRILEGAL were increased by a factor of $1/g_{\text{eff}} = 1.53$ (Just & Jahreiß 2010).

The second rows in Figures 5.3 and 5.6 show the star count results of TRILEGAL based on the Just-Jahreiß parameters. The luminosity functions are worse compared to the default Set 1, because the halo is now over-represented by about 0.2 dex. In the CMD the thick disk fills the minimum in the center of the Hess diagram seen in the default model. The F-turnoff of the thick disk is still slightly too red (metal rich). At the faint (distant) regime there are significantly too many stars in all components.

The overall fit of the Hess diagram with $\langle \chi^2 \rangle = 2.74$ is worse than for the default model due to the bad fit in the faint magnitude range.

5.2.2 Besançon input (Set 3)

The thick disk of Robin et al. (2003) is a piecewise-defined function of height z :

$$\begin{aligned} \rho_t(z) &= \rho_t(\odot) \left[1 - \frac{1/h_t}{a(2 + a/h_t)} z^2 \right] & z \leq a, a = 400 \text{ pc} \\ &\propto \frac{\exp(a/h_t)}{1 + a/2h_t} \exp\left(-\frac{z}{h_t}\right) & z > a. \end{aligned}$$

We fit this piecewise-defined function using a sech^2 and an exponential function, respectively. The exponential function with smaller fitting error is adopted in Column 5 of Table 5.2. The scale height of 910 pc and a local density of $0.0015 \text{ M}_\odot \text{pc}^{-3}$ yield a local surface density $\Sigma(\odot) = 2.82 \text{ M}_\odot \text{pc}^{-2}$.

There are seven sub-populations in the thin disk of the Besançon model. Each sub-population has its own age range, metallicity, and spatial vertical distribution. We fit scale heights and local densities of each sub-population (see Table 5.3). Exponential profiles yield smaller χ^2 values.

In the next step the scale heights as a function of age of Table 5.3 are fitted by the Equation 3.3 of TRILEGAL. The best fit parameters z_0 , t_0 and α are 13.61 pc, 0.02016 Gyr and 0.5524, respectively. The total local density $\rho_d(\odot)$ is the sum of $\rho_i(\odot)$ of each population, namely $0.030 \text{ M}_\odot \text{pc}^{-3}$. And the derived local surface density of the thin disk is $25.20 \text{ M}_\odot \text{pc}^{-2}$.

The local density of the halo in the Besançon model is determined by the SFH and the IMF. The adopted value is much smaller than our local calibration via SDSS data. Therefore, we fit the halo of the Besançon model with the effective radius, oblateness, and local density of the TRILEGAL de Vaucouleurs profile in two steps:

1. We fit the vertical profile to find the effective radius and the oblateness;
2. We use the local density as a new fitting parameter to reproduce the halo star counts of the SDSS and then use this value for Set 3 (Table 5.2).

Table 5.3: The fit results of the thin disk sub-populations in the Besançon model.

Age range (Gyr)	$\langle t \rangle$ (Gyr)	h_i (pc)	$\rho_i(\odot)$ $M_\odot \text{pc}^{-3}$
0-0.15	0.075	32.5	0.0019
0.15-1	0.575	97.8	0.0066
1-2	1.5	120.0	0.0073
2-3	2.5	195.9	0.0043
3-5	4.0	273.5	0.0049
5-7	6.0	328.3	0.0030
7-10	8.5	370.9	0.0020

Note: Column 1 lists the age range of each sub-population in the Besançon model. Column 2 is the simple arithmetic mean age in each bin. We fit the vertical profile of each sub-population via two parameters: scale height h_i (Column 3) and local density $\rho_i(\odot)$ (Column 4). The relationship of t and h_i is determined by fitting a power law function.

In the first step we find the best-fit parameters $q_h = 0.71$ and $r_{\text{eff}} = 39.436$ kpc. In the second step we determine the local density of the halo by fixing q_h and r_{eff} and fitting the SDSS data in a restricted area of the Hess diagram, where the halo dominates (i.e. in the dashed triangle of Figure 5.11, see Section 5.3). The best-fit local density of the stellar halo is $\rho_h(\odot) = 0.00009 M_\odot \text{pc}^{-3}$, which is about 10 times larger than the value used in the Besançon model.

The upper row in Figure 5.4 and 5.7 shows the star count results of TRILEGAL based on the Besançon parameters. The luminosity functions show a significant deficiency at bright magnitudes dominated by the thin and thick disk and a reasonable fit at the faint end. In the CMD the thin and thick disk regime are strongly under-represented in the model. The halo with the original local density would also be under-represented.

The overall fit of the Hess diagram with $\langle \chi^2 \rangle = 2.65$ is better than that of Set 2 but worse than the default set (Set 1).

This result is not a judgement on the Besançon model compared to the Just-Jahreiß or TRILEGAL model. It is a measure of the flexibility of the TRILEGAL model.

5.2.3 Jurić input (Set 4)

We do not consider the scale height as a function of the age of the sub-population in the Jurić case ($\alpha = 0$ in Equation 3.3). Jurić et al. (2008) fit the basic parameters of their Galactic model via star count observations by the SDSS. Only their final parameters of their disks are considered in our article. Jurić et al. (2008) describe the vertical profiles of the thin and thick disk by simple exponentials with

$$h_d = 300 \text{ pc}, \rho_d(\odot) = 0.029 M_\odot \text{pc}^{-3} \text{ for the thin disk and}$$

$$h_t = 900 \text{ pc}, \rho_t(\odot) = 0.0034 M_\odot \text{pc}^{-3} \text{ for the thick disk. This corresponds to 12 per cent of}$$

the local density of the thin disk given by Jurić et al. (2008). The derived local surface density of the thick disk is $\Sigma_t(\odot) = 6.12 \text{ M}_\odot \text{pc}^{-2}$.

The halo density profile is fitted by TRILEGAL with three parameters. The best-fit parameters are oblateness $q_h = 0.59$, local density $\rho_h(\odot) = 0.000145$, and effective radius $r_{\text{eff}} = 18304 \text{ pc}$.

The lower row in Figure 5.4 and 5.8 show the star count results of TRILEGAL based on the Jurić parameters. The luminosity functions are slightly better than for Set 3. They show a significant deficiency at bright magnitudes dominated by the thin and thick disk and too many stars at the faint end. In the CMD the fit of the thick disk regime and the halo is reasonable in the model. At the red end the bright part is under-represented and the faint end is over-represented.

The overall fit of the Hess diagram with $\langle \chi^2 \rangle = 1.76$ is the best of the four Sets.

An overall comparison of Sets 1 to 4 shows that the default Set fits best the luminosity functions in the g and r band. This confirms the fitting procedure used in TRILEGAL to determine those parameters mainly by comparing luminosity functions in different fields.

All models fail to give a good fit of the CMD. In the next section we try to optimize the TRILEGAL parameters to solve this problem.

5.3 Optimizing (Set 5)

In order to find the best TRILEGAL model it is necessary to obtain the best-fitting parameters. Because there are so many parameters that can be adjusted within TRILEGAL, we cannot determine them simultaneously. But since the thin disk, thick disk, and the halo are not completely overlapping in the $(g - r, g)$ CMD, it is possible to optimize the parameters for halo, thick disk, and thin disk sequentially.

Figure 5.11 gives the schematic diagram to distinguish areas, where only the halo, the halo and thick disk, and where only thick and thin disk contribute significantly to the star counts. We define the separating lines by relative densities of these three components based on the Just-Jahreiß model. In that triangle (dashed line) the halo dominates the other two components because the relative density of disks to halo is less than 1 per cent. In the area under the solid line, the thin disk can be neglected, because the relative density of thin disk to thick disk is less than 1 per cent. We will fit first the halo parameters in the triangle. Then we fix the halo parameters and fit the thick disk parameters below the full line including the star counts of the halo. Finally, we investigate the thin disk parameters by taking into account all three components in the full CMD.

5.3.1 Halo fitting

Locating an area with halo stars but very few disk stars in the CMD is the first step. Our choice is marked by the dashed triangle in Figure 5.11. The disks stars in this selected region can be neglected, i.e., $(\rho_{\text{thin}} + \rho_{\text{thick}})/\rho_{\text{halo}} < 0.01$ as estimated by the Just-Jahreiß model. The boundary conditions to determine the halo parameters are $g - r \geq 0.2$ and $g \geq 15.5 + 12.5(g - r)$. We choose an oblate $r^{1/4}$ spheroid and search for a best fit in the parameter ranges:

$$0.00005 \text{ M}_\odot/\text{pc}^3 \leq \Omega_h(\odot) \leq 0.00035 \text{ M}_\odot/\text{pc}^3;$$

$$2000 \text{ pc} \leq r_h \leq 30000 \text{ pc};$$

$$0.57 \leq q_h \leq 0.70.$$

The fitting result is shown in left panels of Figure 5.12. The best-fitting halo parameters are listed in the last column (Set 5) of Table 5.2 with $\langle \chi^2 \rangle = 0.062$.

5.3.2 Thick disk fitting

We fix the parameters of the halo determined in Section 5.3.1 to fit the parameters of the thick disk in the area dominated by the thick disk (below the solid line determined by $g \geq 16.5 + 3.64(g - r)$ in Figure 5.11). In this area, only relatively few thin disk stars exist, i.e., $\rho_{\text{thin}}/(\rho_{\text{thick}} + \rho_{\text{halo}}) < 0.01$.

The $\text{sech}^2()$ and $\exp()$ prescriptions are tried to fit the vertical profile of thick disk with the parameters scale height h_t and local calibration $\rho_t(\odot)$ within the following ranges:

$$0.0010 \text{ M}_\odot/\text{pc}^3 \leq \rho_t(\odot) \leq 0.00035 \text{ M}_\odot/\text{pc}^3;$$

$$400 \text{ pc} \leq h_t \leq 900 \text{ pc}.$$

The minimum $\langle \chi^2 \rangle = 0.207$ was found for the $\text{sech}^2()$ profile with the best-fitting parameters listed in Column 7 of Table 5.2. The minimum $\langle \chi^2 \rangle$ of the fit using an exponential function is 0.312.

The fit result, shown in the left panels of Figure 5.12, shows on the one hand a homogeneous quality of the fit, but on the other hand already a systematic trend along the MS of the thick disk with too few stars in the G dwarf regime and too many K and M dwarfs.

5.3.3 Thin disk choice

For the thin disk fitting we now fix the halo and thick disk as determined above. For the thin disk we cannot get a best fit of all free parameters. We analyzed the advantages and disadvantages of the thin disk models of Sets 1, 2, 3, and 4 and then adjusted the parameters iteratively to get a better result. All iterations to improve the parameters in order to find an optimal Milky Way model must be done by hand. The power index α changes the fractions of different sub-populations as a function of height above the mid-plane. In the Hess diagram it affects the balance of densities between $g - r > 1$ and $0.2 < g - r < 0.4$. The values for z_0 and $\rho_{d,0}$ affects the total density of the thin disk. These are the general directions to adjust the parameters. The value of t_0 was not changed.

We did these investigations for both vertical profile shapes.

The sech^2 profile results in a better fit with minimum $\langle \chi^2 \rangle = 1.33$ (Set 5, last column of Table 5.2).

5.3.4 Model properties

The final Set 5 (last column of Table 5.2) has a smaller local surface density and smaller maximum scale height $h_{z,\max}$ than the default Set 1, because it does not need to replace also thick disk stars.

The Hess diagram analysis for input Set 5 is plotted in Figure 5.14.

The χ^2 distribution is smoother than for the other four sets, but the systematic features in the relative deviations of data and model do not vanish. These are (see middle panel of Figure 5.14)

1. The dark region at $g - r = 0.2$ is a sign of too many nearby blue (low metallicity) halo stars.
2. The white island at $g - r = 0.35$ and $15 < g < 17$ mag points to a mismatch of the thick disk turn-off stars. There are too few nearby stars due to the flat sech^2 profile or the turn-off is too red.
3. The faint red end with color-magnitude range of $g - r > 1.0$ and $g > 18$ mag shows too many M dwarfs. The reason may be that the $g - r$ color of the thin disk M dwarfs is slightly too blue or that the IMF allows too many stars at the low mass end.
4. The white islands at the bright red end show that the M dwarf density in the solar neighborhood is still underestimated.

The magnitude distributions in the g and r band (see Figure 5.15) show larger discrepancies than for the default Set 1 (upper row of Figure 5.3). This is again a hint that the Hess diagram analysis is much more powerful than luminosity function fitting.

Compared to the Just-Jahreiß model with $\langle \chi^2 \rangle = 0.055$ (Just et al. 2011), the fit of Set 5 is much worse. This is also obvious from the typical relative deviations exceeding 20 percent. The mismatch of the isochrones in $ugriz$ filters cannot account for these deviations. The simple structural forms of thin and thick disks are the main reasons for the large discrepancies.

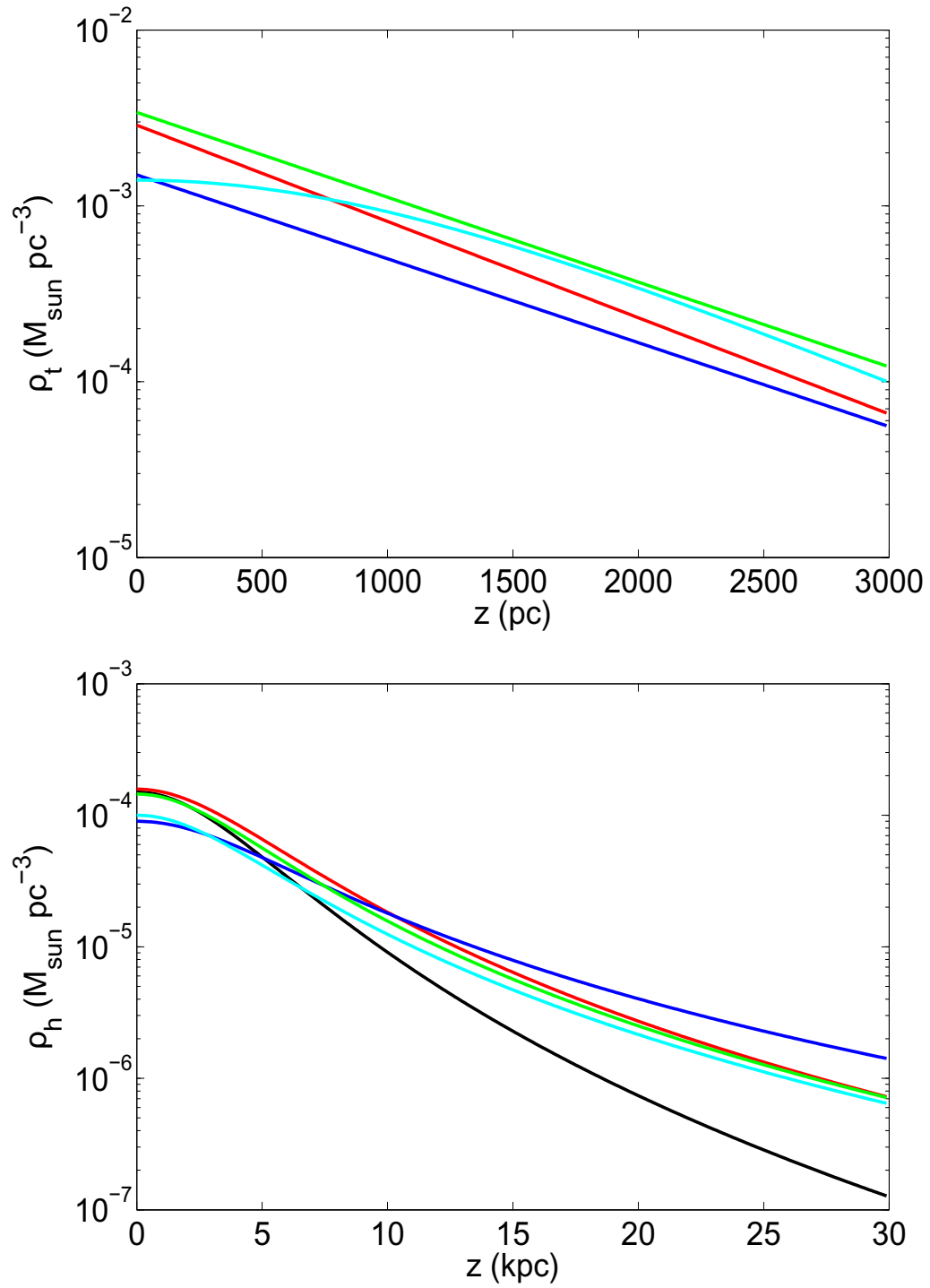


Figure 5.1: The vertical density profiles of thick disk (top panel) and halo (bottom panel) of Set 1 (black), 2 (red), 3 (blue), 4 (green), and 5 (cyan). There is no thick disk in Set 1. The z ranges of the panels are different.

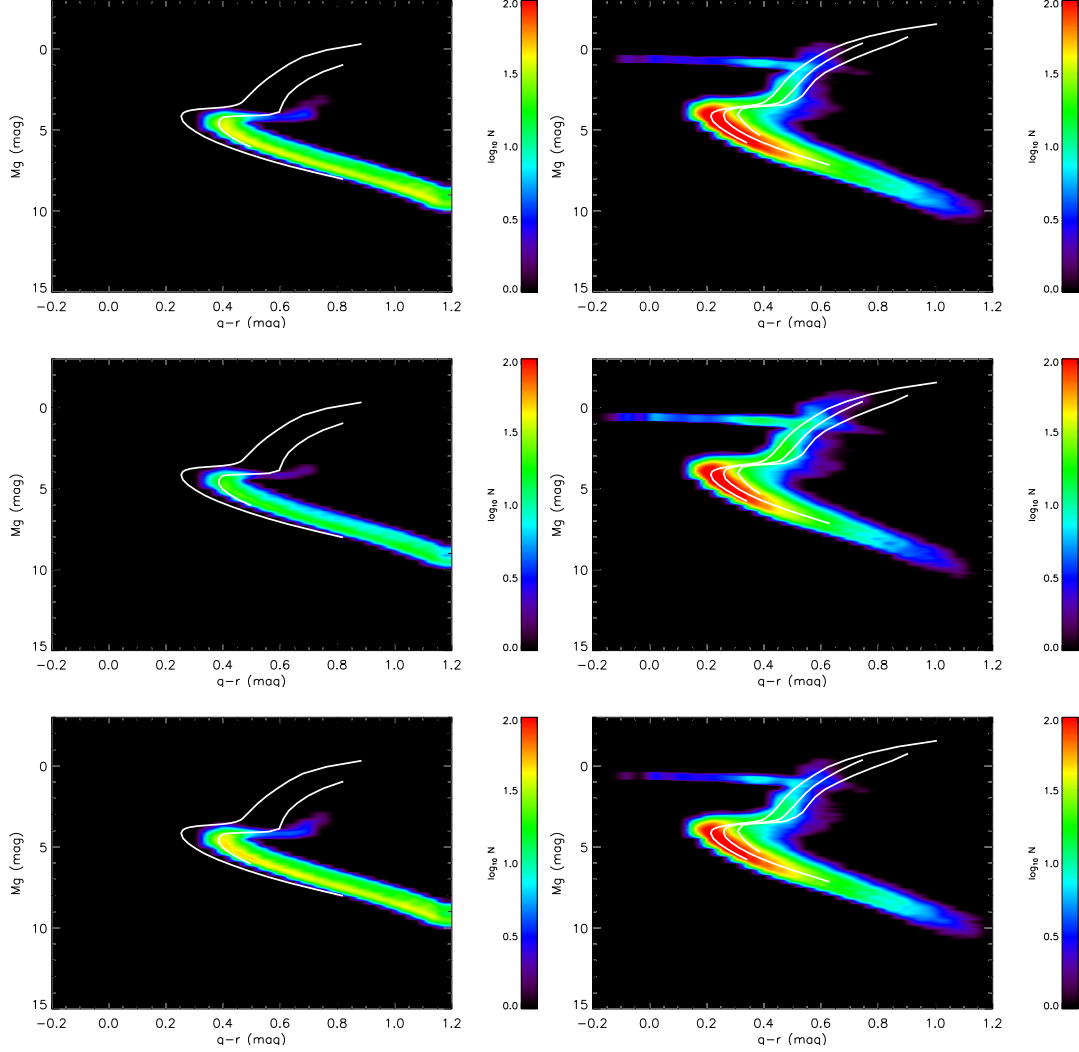


Figure 5.2: The fiducial isochrones of globular clusters from An et al. (2008) (white lines) are overlotted on Hess diagrams of absolute magnitude. The left column shows Hess diagrams of thick disks simulated by the TRILEGAL model using Sets 2, 3 and 4 (left to right). Fiducial isochrones of the globular clusters M5 (left) and M71 (right) are overlotted as white lines. The right column shows the Hess diagrams of corresponding halo populations. From left to right, white lines representing the fiducial isochrones of the three globular clusters NGC 4147, M3 and Pal 5 cover the halo's Hess diagram. The globular clusters are selected to be close to the metallicities of the thick disk and halo which are adopted in the TRILEGAL model.

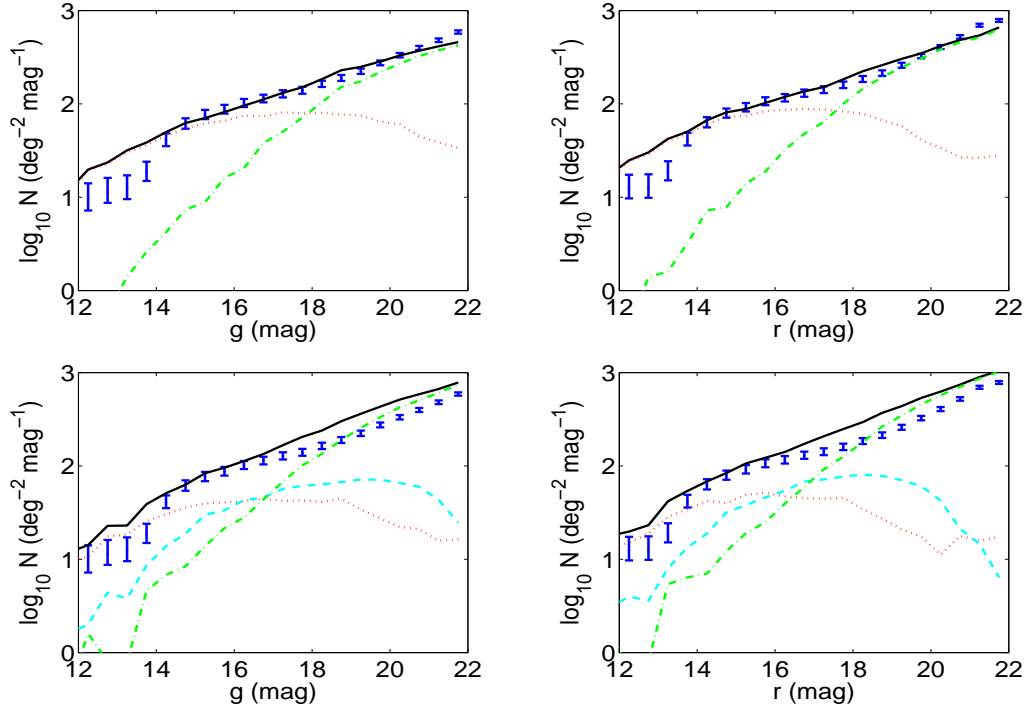


Figure 5.3: The magnitude distributions of the SDSS observations and the TRILEGAL simulations generated with Sets 1 and 2 (top to bottom). The X- and Y-axes are similar to the bottom panel of Figure 4.5. The error bars (blue) are from SDSS DR7 data with the color limit of $0.2 \leq (g - r) < 1.2$. The black solid line represents the model star counts from TRILEGAL. The dotted (red), dashed dotted (cyan) and dashed (green) line stands for the thin and thick disks and the halo from the TRILEGAL model respectively.

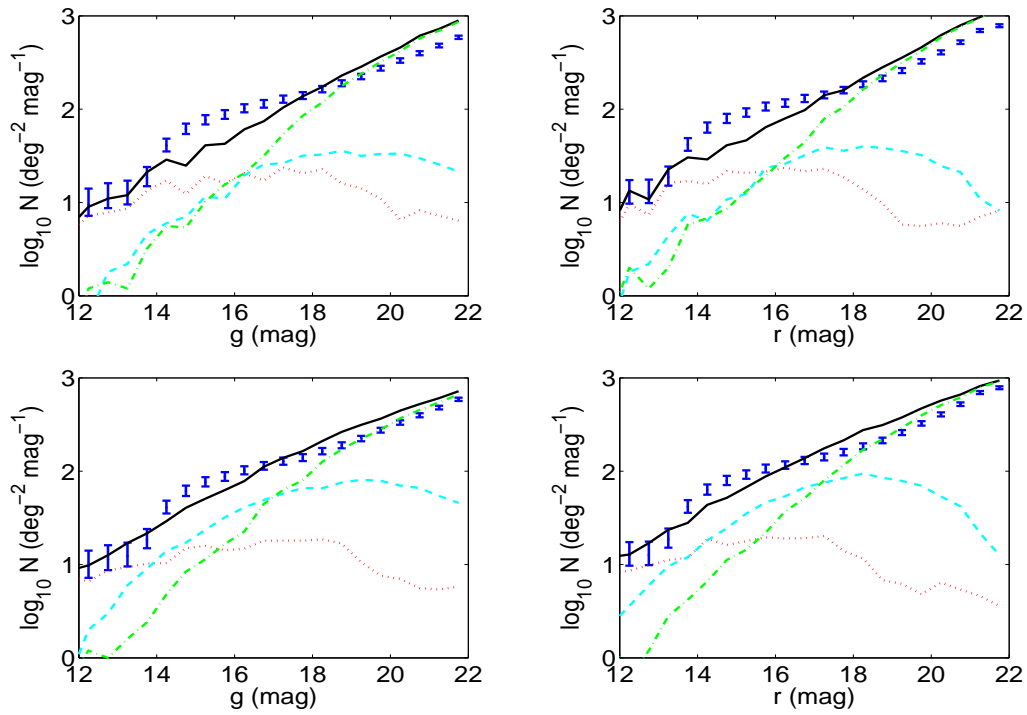


Figure 5.4: Continue of Figure 5.3. The magnitude distributions of the SDSS observations and the TRILEGAL simulations generated with Sets 3 and 4 (top to bottom) are shown.

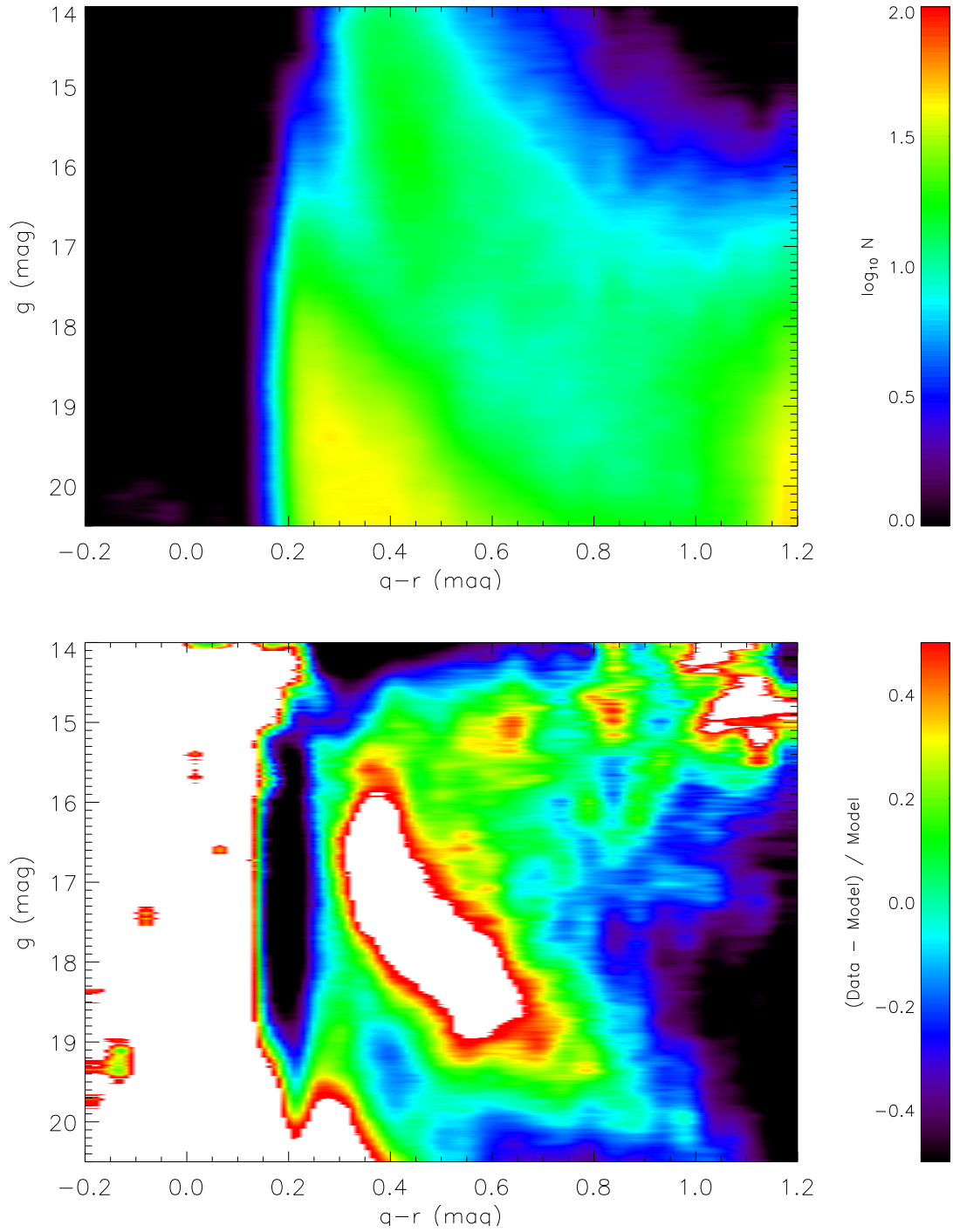


Figure 5.5: Hess diagrams (upper panel), relative differences (lower panel) between the Hess diagrams of the models of Set 1 and the SDSS observations. The notation is the same as in Figure 4.4. Note that the color ranges in the lower panel cover a much larger range (-50% to $+50\%$).

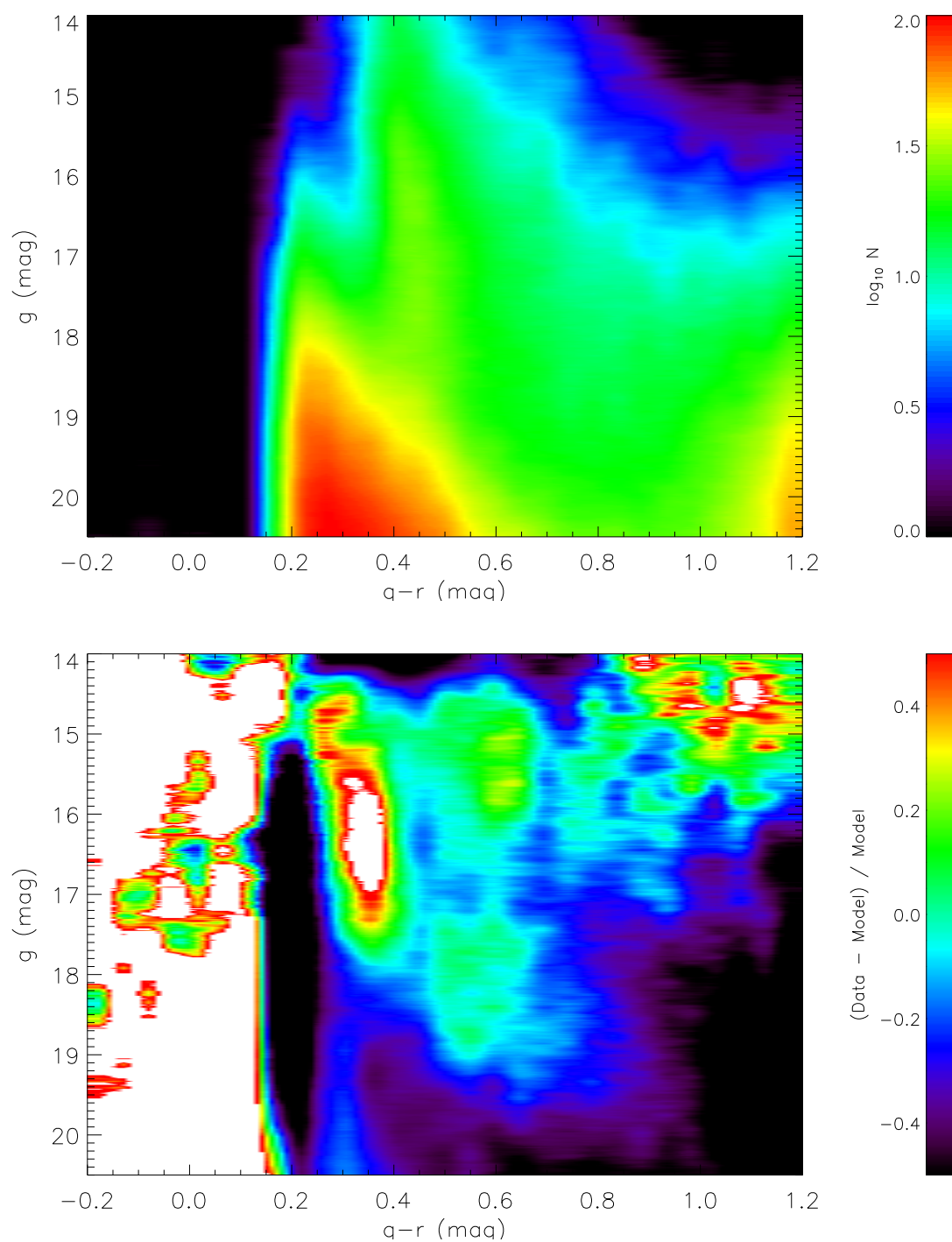


Figure 5.6: Same as Figure 5.5 but for Set 2.

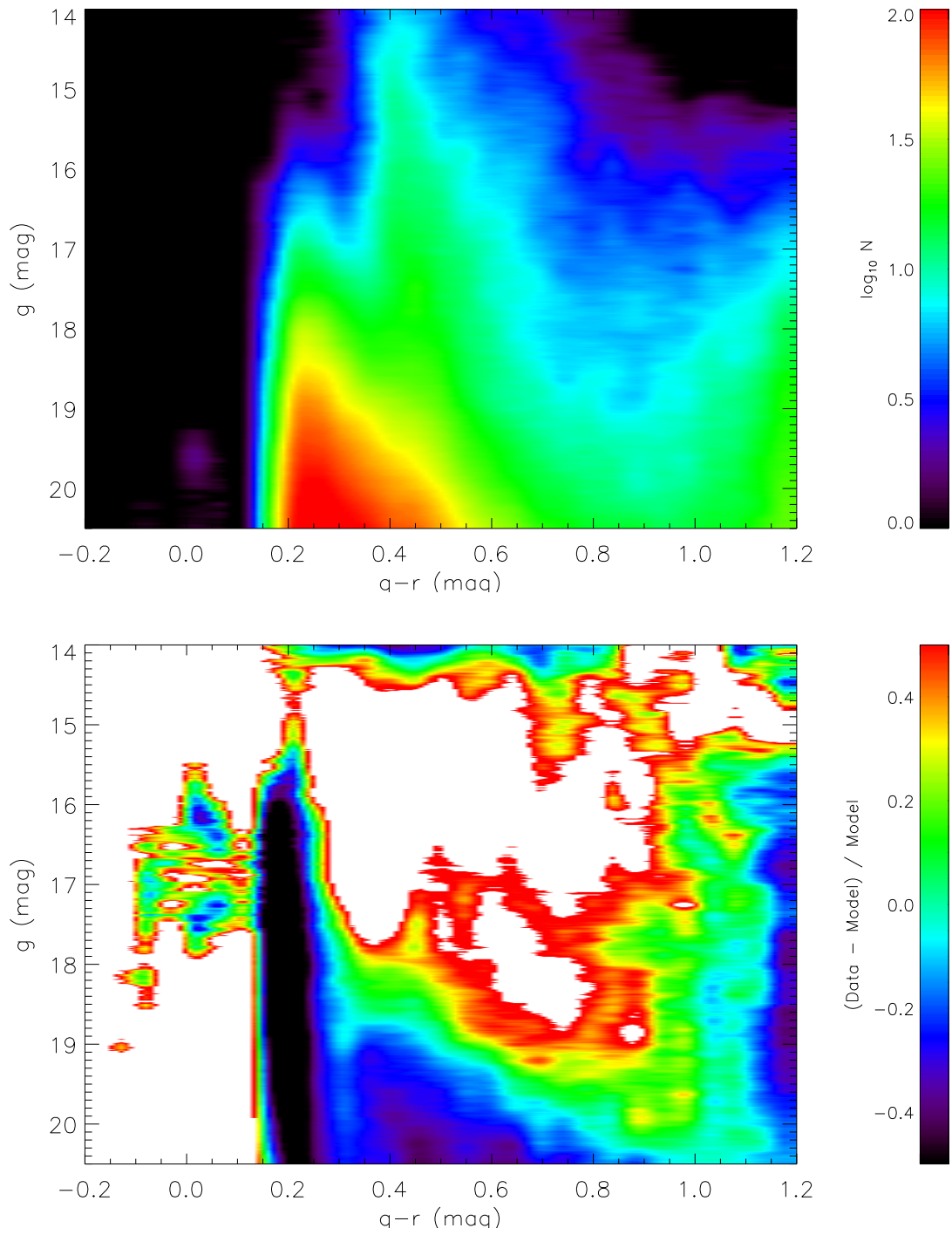


Figure 5.7: Same as Figure 5.5 but for Set 3.

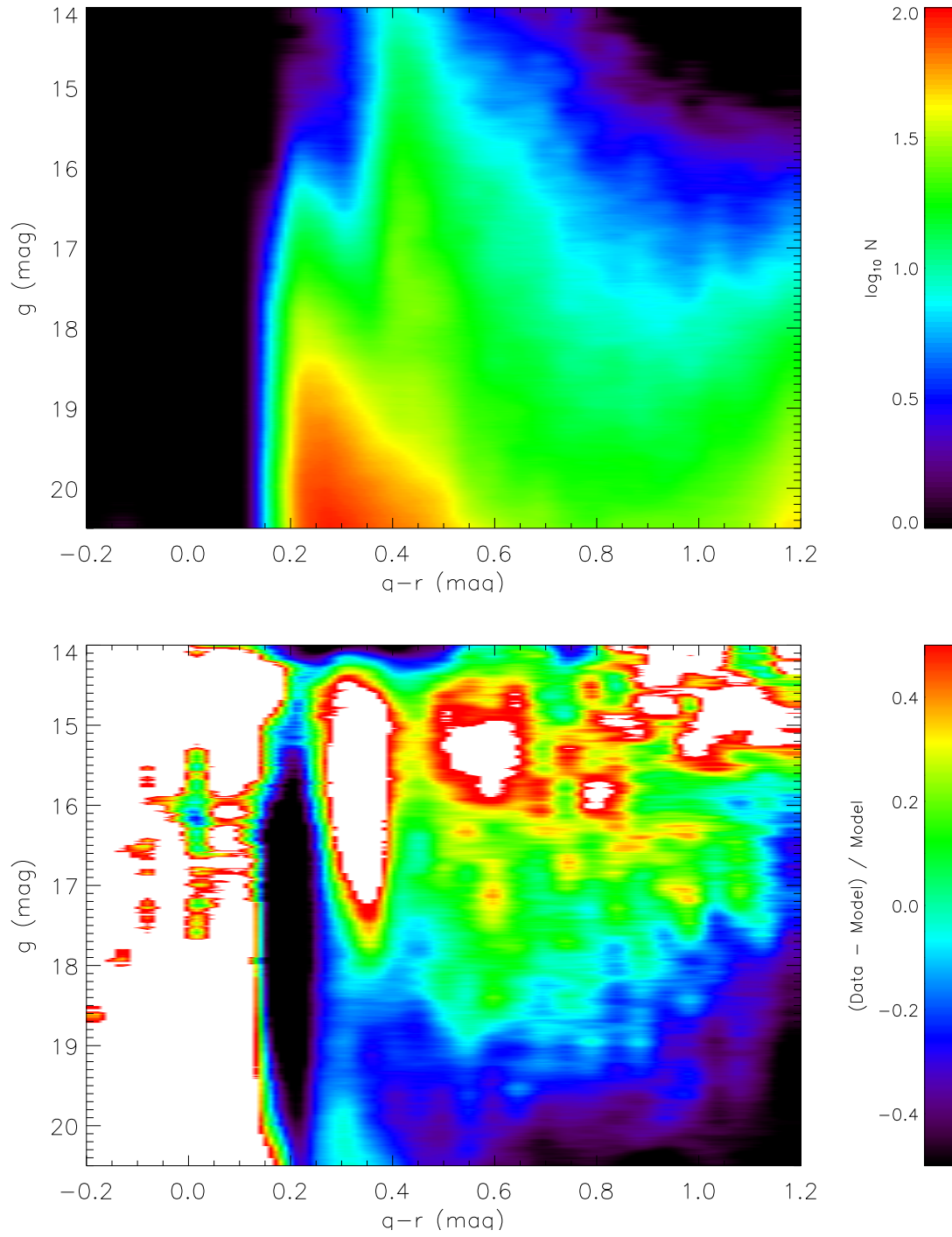


Figure 5.8: Same as Figure 5.5 but for Set 4.

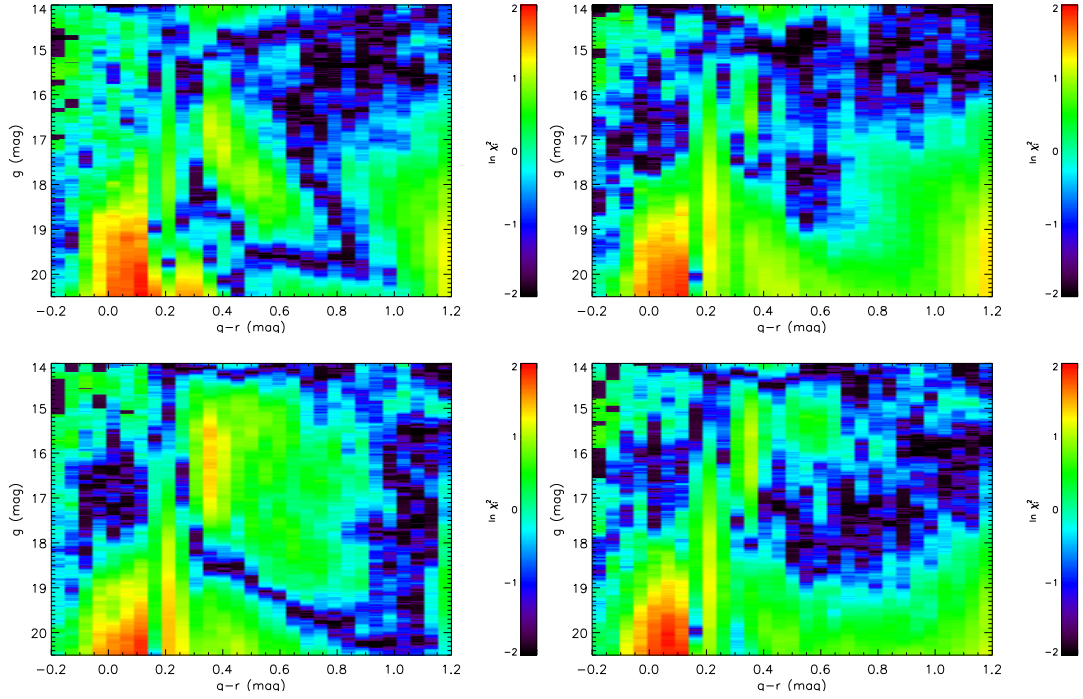


Figure 5.9: The χ^2 diagrams of the Hess diagrams of the models and the SDSS observations. From top-left to bottom-right we show the comparisons based on Sets 1 to 4, respectively. The notation is the same as in Figure 4.4. Note that the color ranges in panels cover much larger ranges (-2 to +2).

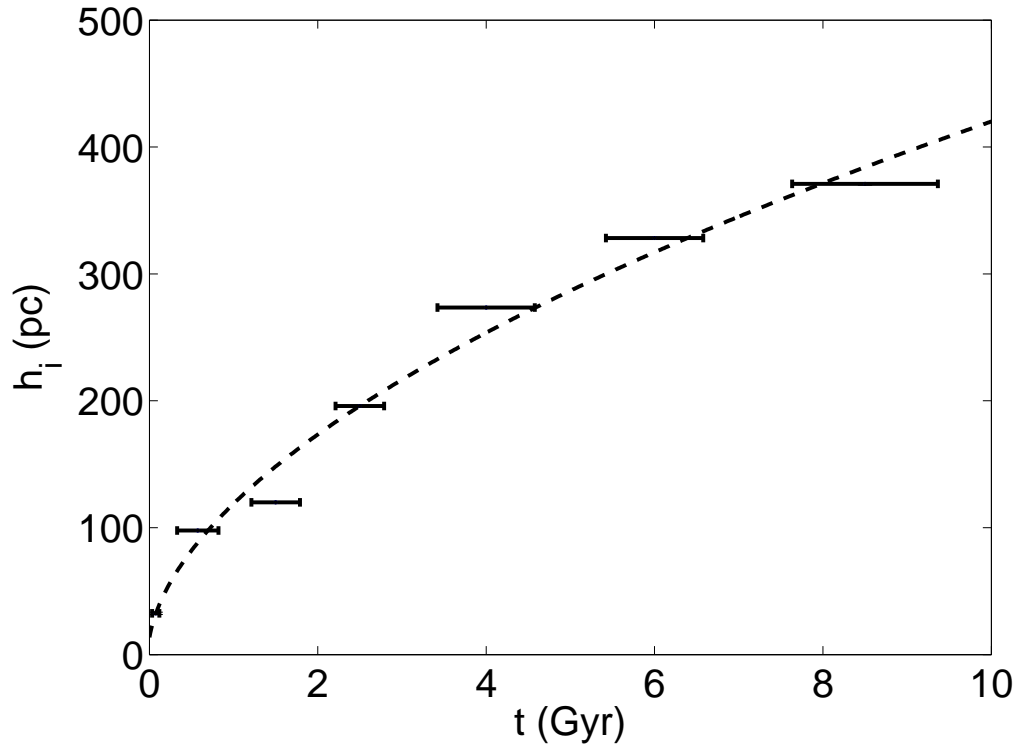


Figure 5.10: The scale height of each age bin of Besançon model and the fitting by TRILEGAL using Equation 3.4. The x-axis is the age of the sub-populations in Gyr up to 10. The y-axis is the scale height in pc. The error bars stand for 7 sub-populations of the thin disk in the Besançon model and the dashed line is the fit result.

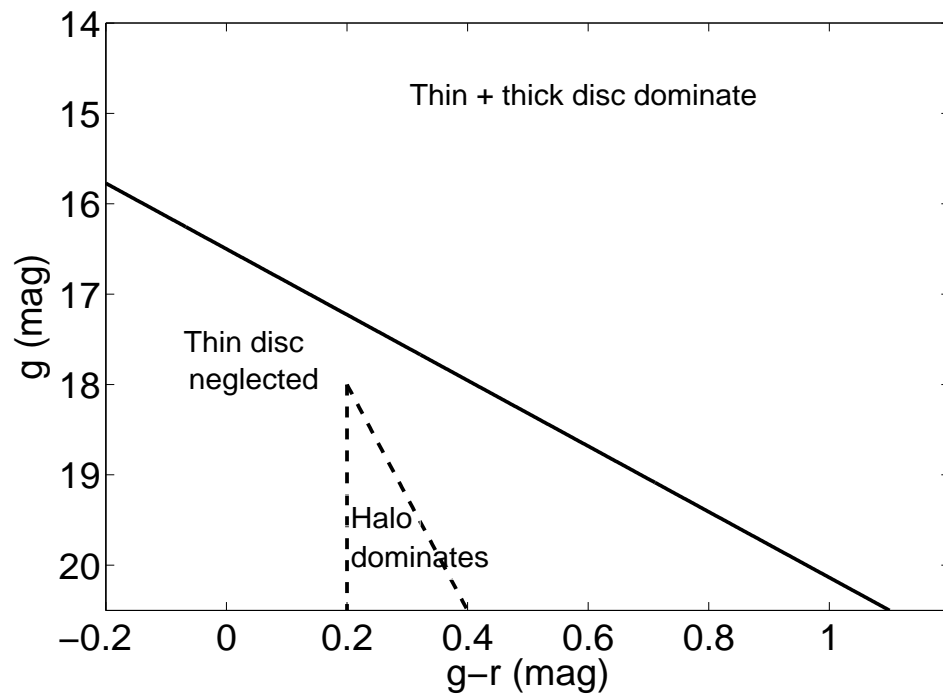


Figure 5.11: A Schematic diagram of the CMD illustrating the distinction between thin and thick disk and halo stars. The dashed triangle represents the area where the halo dominates. The solid line is the upper boundary below which the thin disk contribution is negligible.

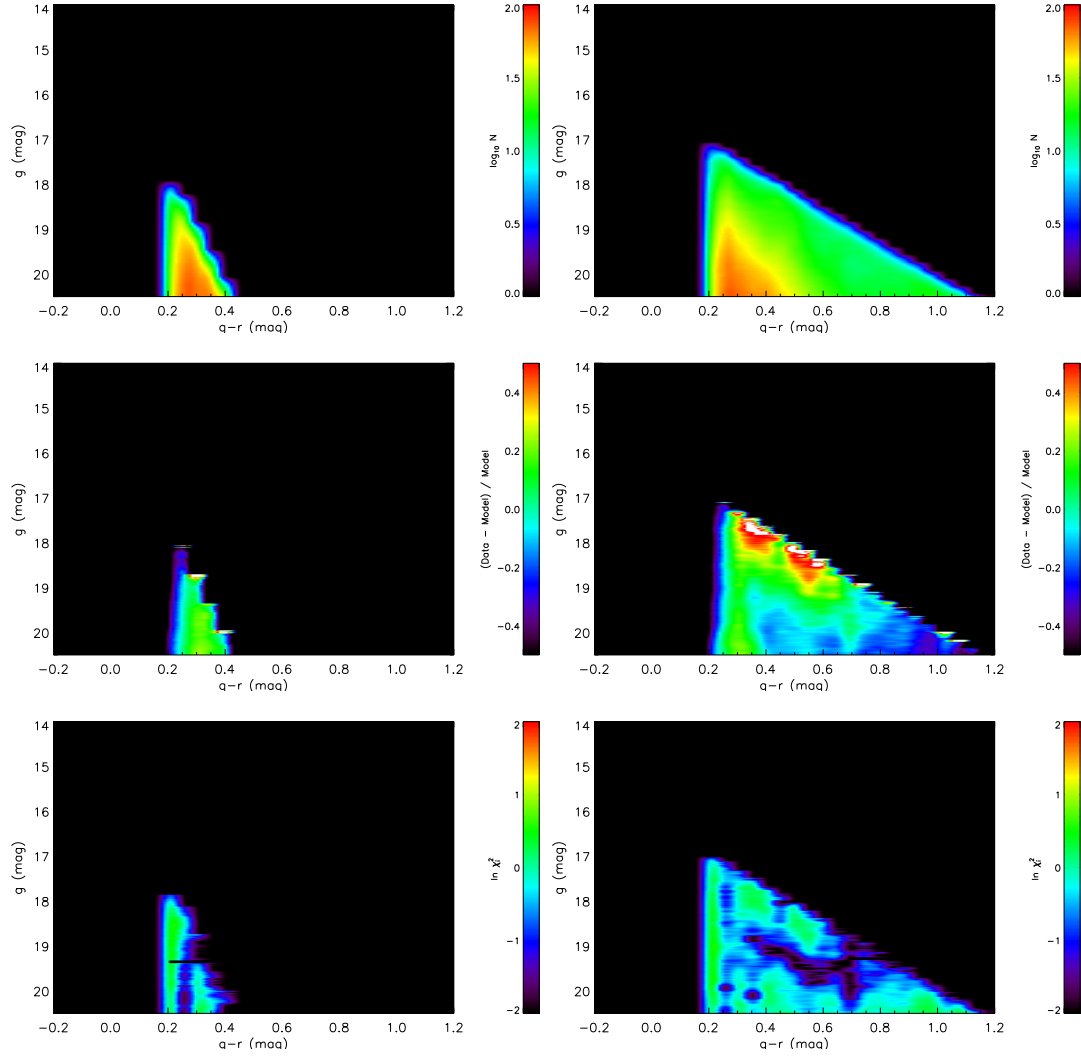


Figure 5.12: Hess diagrams, relative differences and χ^2 distribution (top to bottom) of the best-fit halo and (the left panels) the thick disk (the right panels) in TRILEGAL for Set 5. The coding is the same as in the rows of Figure 5.5.

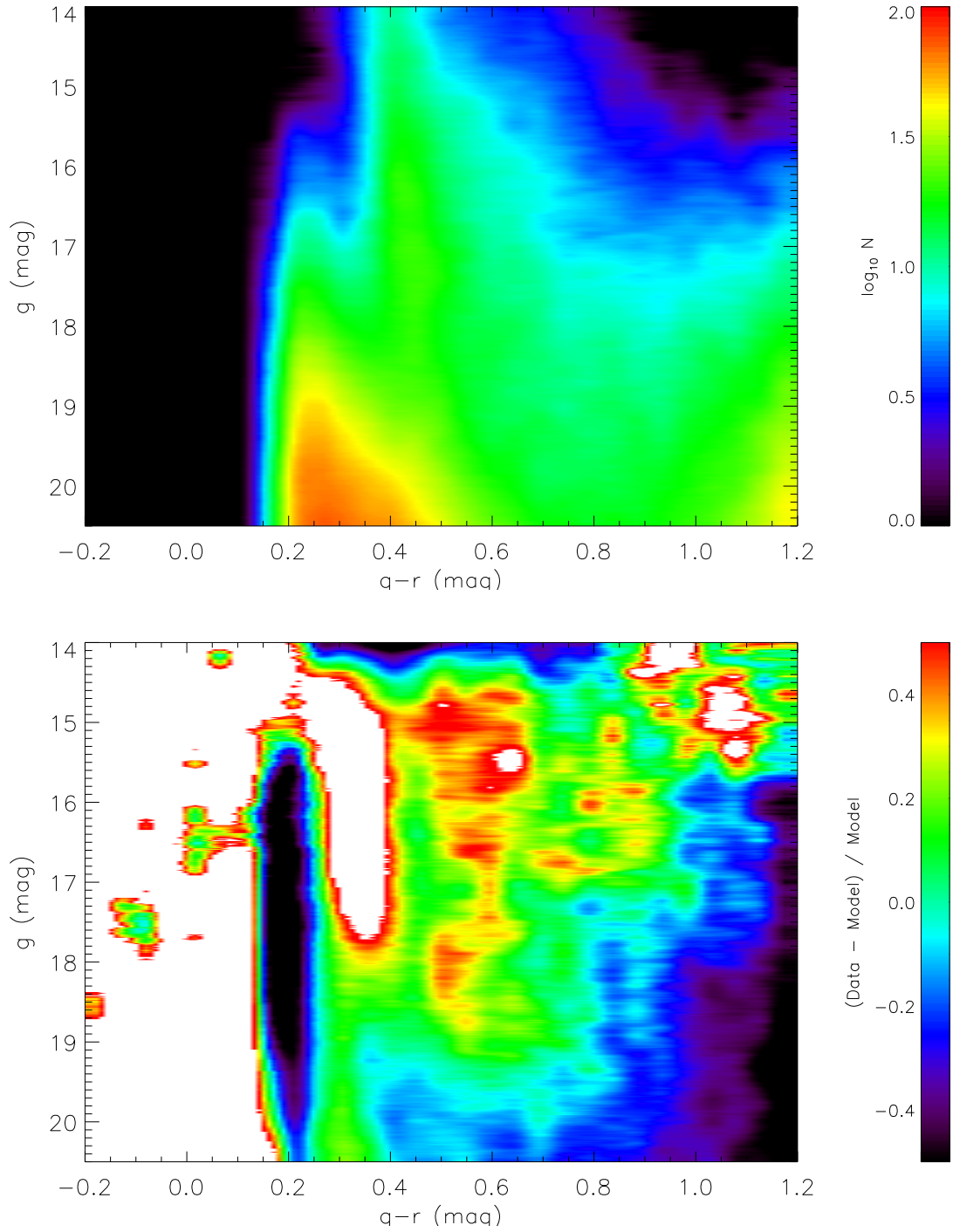


Figure 5.13: Hess diagrams (top), relative differences (middle) between the Hess diagrams of the Set 5 and the SDSS observations, and the χ^2 diagrams (bottom). The notation is the same as in Figure 4.5. Note that the color range in the middle panel covers a much larger range than before, namely ± 50 per cent.

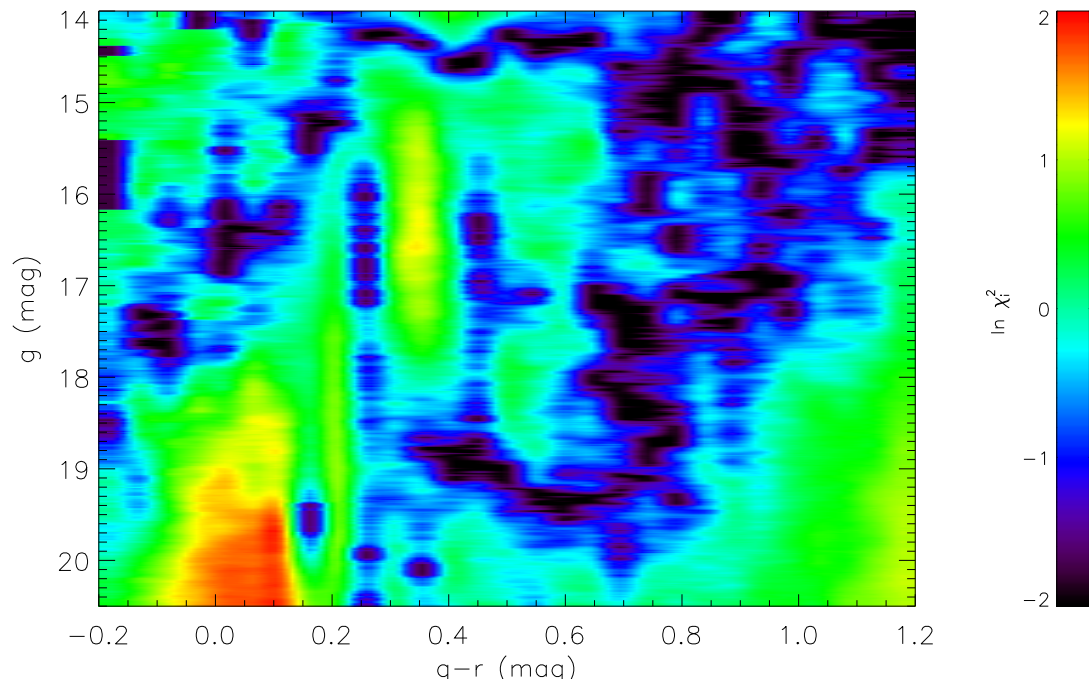


Figure 5.14: The χ^2 distribution of the Set 5 and the SDSS observations, and the χ^2 diagrams (bottom). The notation is the same as in Figure 4.5.

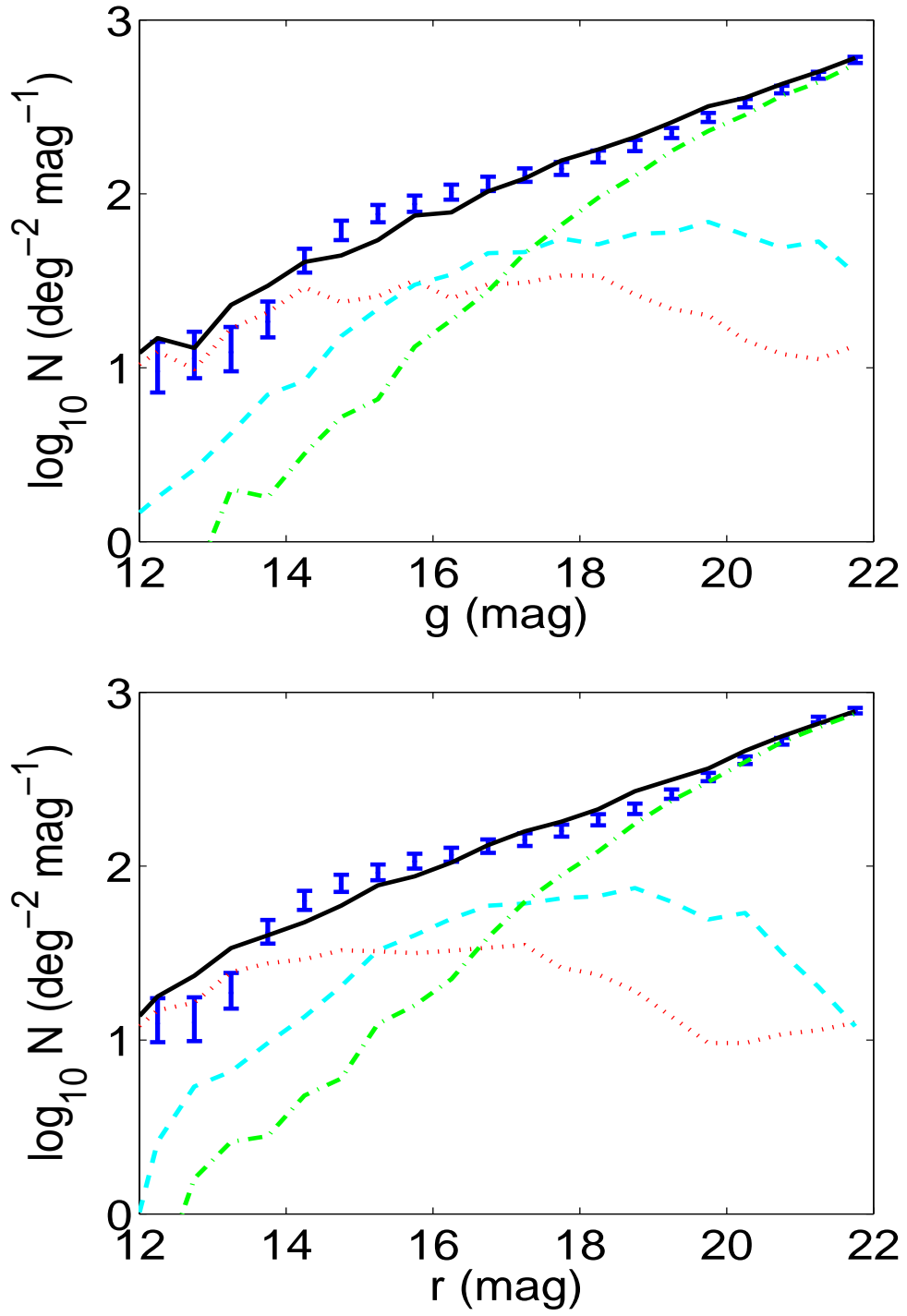


Figure 5.15: Same as Figure 5.3 but for Set 5.

“Science without religion is lame, religion without science is blind.”

A. Einstein, 1941



Multi-color tests of the Besançon model

The Besançon model is discussed in this chapter. The model is tested and is compared with the SDSS data via the automatic process on the web of Besançon. The area target is limited to high latitude field. We focus on the multi-color comparisons between the Besançon simulations and the SDSS photometric data.

6.1 Multi-color simulations

Robin et al. (2003) developed the stellar population synthesis approach to simulate the structures and kinematics of the Milky Way. The Besançon model is based on the calibration with different well calibrated data sets and the structural parameters are optimized to reproduce a set of selected fields at the sky. The model was continuously improved and extended by adding additional filter sets. The simulation of each component is based on a set of evolutionary tracks, assumptions on stellar number density distributions, constrained either by dynamical considerations or by empirical data, and guided by a scenario of a continuous formation and evolution of the stellar populations.

Our target is limited to the NGP with a Galactic latitude $b > 80^\circ$. In this volume, stars belonging to the Galactic bulge can be ignored. The stellar populations in the NGP field can be divided in three distinct components: thin, thick disks and stellar halo. For details of the properties of the Galactic components (see Robin et al. (2003)).

The Besançon model is able to output a photometric catalogue with distances, extinctions, spatial velocities etc. The de-reddened photometric data are our basic catalogue. The catalogue simulations with five color photometric data are considered to be the test of the population synthesis approach. With the NGP field we can test the vertical structures of the Galactic components and the calibration of the underlying isochrones in the filter system. There are two possible choices of the photometric system: the Johnson-Cousins or the CFHTLS-Megacam system. Each system can output a user-defined apparent magnitude and a series of color indexes. The Johnson-Cousins system includes one apparent magnitude and four color indexes $B-V$, $U-B$, $V-I$, and $V-K$. The CFHTLS-Megacam system includes one of five pass-bands (u^* , g' , r' , i' and z') and four color indexes $u^* - g'$, $g' - r'$, $r' - i'$, and $i' - z'$. Their output ranges can be limited in the web interface.

The CFHTLS-Megacam is selected to be our photometric system in order to input the simulated volume and magnitude (and color), since we have reliable method to make transforms

Table 6.1: Properties of the observed and simulated CMDs.

CMD	color	magnitude	N_{obs}	N_{mod}	N_{d}	N_{th}	N_{h}	$f_{\text{obs}}^{\text{mod}}$
$(u - g, g)$	$[-0.2, 2.0)$	$[14.0, 20.5)$	238 724	261 205	43 285	133 603	84 550	1.09
$(g - r, g)$	$[-0.2, 1.2)$	$[14.0, 20.5)$	279 174	312 093	94 590	134 209	83 587	1.12
$(r - i, r)$	$[-0.2, 1.2)$	$[14.0, 20.5)$	479 913	433 533	145 784	183 777	103 955	0.90
$(i - z, i)$	$[-0.2, 0.5)$	$[14.0, 18.5)$	220 144	237 249	97 560	114 468	25 236	1.08

Note: Column 1 lists the color and magnitude of the CMD, columns 2 and 3 list the ranges in color and apparent magnitude, columns 4 and 5 show the total stellar number of data N_{obs} and model N_{mod} for each CMD. The stellar numbers of the three components are listed in columns 6 to 8: N_{d} , N_{th} and N_{h} . The last column is the relative ratio of stellar numbers of the observation to the model.

between CFHTLS and SDSS systems. The mock catalogues of thin and thick disks, halo and of their sum are generated by the Monte-Carlo procedures in different jobs via the Besançon interface. The stellar number of the sum of the three components is therefore not exactly the same as the stellar number of the general simulation.

6.1.1 Photometric conversions

In order to obtain SDSS magnitudes g , r , i and z and colors $u - g$, $g - r$, $r - i$ and $i - z$ from the Besançon model, the photometric system needs to be transformed from u^* , g' , r' , i' and z' filter set using a two-step method. The first step transforms to u' from the special u^* filter. And then the second step transforms to u , g , r , i and z from u' , g' , r' , i' and z' filters.

The transformation in the UV filter is given by (Just & Jahreiß 2008; Tucker et al. 2006)

$$u' = u^* + \sum_{j=0}^3 c_j \cdot (g' - i')^j, \quad (6.1)$$

where the polynomial coefficients c_j are listed in Table 6.2.

The conversion from u' , g' , r' , i' and z' to g , r , i and z follows the transformation in Tucker et al. (2006) and Just & Jahreiß (2008):

$$u = u', \quad (6.2)$$

$$g = g' + c_g[(g' - r') + p_g], \quad (6.3)$$

$$r = r' + c_r[(r' - i') + p_r], \quad (6.4)$$

$$i = i' + c_i[(r' - i') + p_i], \quad (6.5)$$

$$z = z' - c_z[(i' - z') + p_z], \quad (6.6)$$

where the coefficients c_k and p_k are listed in Table 6.3.

Table 6.2: The polynomial coefficients of the transformation in the u band

j	c_j
0	0.1816
1	-0.5293
2	0.3332
3	-0.0556

Note: A quartic polynomial is used to transform u^* to u' . The polynomial coefficients are listed in this table.

Table 6.3: The coefficients of transformation in $griz$ band

k	c_k	p_k
g	0.060	-0.53
r	0.035	-0.21
i	0.041	-0.21
z	-0.030	-0.09

Note: A unified form is used to transfer $u'g'r'i'z'$ into $ugriz$ system. The difference between them is a function of color indexes. The coefficients c_k and p_k are listed in Column 2 and 3.

The color transformations are derived as follows:

$$u - g = u' - g' - 0.060(g' - r') + 0.0318, \quad (6.7)$$

$$g - r = 1.060(g' - r') - 0.035(r' - i') - 0.0245, \quad (6.8)$$

$$r - i = 0.994(r' - i') + 0.001, \quad (6.9)$$

$$i - z = 0.041(r' - i') + 1.03(i' - z') - 0.0113. \quad (6.10)$$

These de-reddened and transformed u , g , r , i and z data with color indexes and absolute magnitudes are used to plot magnitude distributions and CMDs.

6.2 Isochrones

Since the thick disk and the halo are modeled in the Besançon model by simple stellar population with a single age and metallicity ($[\text{Fe}/\text{H}] = -0.78 \pm 0.30$ for thick disk and $[\text{Fe}/\text{H}] = -1.78 \pm 0.50$ for halo), the isochrones can be compared to fiducial sequences of star clusters with corresponding properties. An et al. (2009) presented a detailed analysis of isochrones fitting to fiducial sequences in $ugriz$ filters of globular and open clusters mentioned in An et al. (2008) (see Table 2.2). The authors included a comparison with clusters observed with the CFHTLS-Megacam by Clem et al. (2008). It was found that the cluster M71 with metallicity $[\text{Fe}/\text{H}] = -0.73$ shows a significant offset in $u'g'r'i'z'$ due to a zero-point problem.

The de-reddened magnitude, de-reddened color index, and absolute magnitude are determined in Section 2.2.2.

We plot CMDs using the absolute magnitudes M_g , M_r and M_i in ranges of -3 to 15 and fiducial isochrones of globular clusters in Table 2.2: M5 and M71 are shown in each subplot of the thick disk (left panel of Figure 6.1) from left to right at turn-off; M92, NGC 4147 and M13 are shown in each subplot of the halo (right panel of Figure 6.1) from left to right at turn-off. Therefore a redder turnoff in the data means that the metallicity is higher. Because of a zero-point problem of u band, there is a serious offset of fiducial isochrones and simulating CMDs in top row of Figure 6.1.

CMDs of the thick disk are too blue compared with the fiducial isochrones. The metallicity of cluster M71 is closest to the metallicity of the thick disk adopted in Robin et al. (2003). Isochrones of the thick disk correspond to fiducial isochrones with metallicity below -1.0 (for reasons see discussion of M71 in An et al. 2009).

For the halo (if $[\text{Fe}/\text{H}] > -2$) it is similar. The isochrone of cluster M92 with $[\text{Fe}/\text{H}] = -2.28$ may match the CMD of halo finally.

However, there are no globular clusters with much lower metallicity to cover the blue side of turn-off of models.

Just & Jahreiß (2010), Just et al. (2011) and Gao et al. (2011) show that the population is able to be simulated very well by the single component of globular cluster M13. In contrast, the Besançon model assumes the halo is the one-burst population with much lower metallicity. The shift caused by the unsuited metallicity is shown as the halo subplot of Figure 6.1 (more details in Section 4.2).

6.3 Luminosity function and Hess diagram analysis

We calculated the Hess diagrams of SDSS data and simulations in the same way. Star counts are stacked in each CMD in boxes of (0.05 mag, 0.5 mag) and smoothed in steps of 0.001 mag. Number counts are given in log-scale covering a range of $1 \dots 100$ per deg^2 , 0.1 mag in color and 1 mag in luminosity. The relative differences between the model and the data $(\text{data} - \text{model})/\text{model}$ are smoothed only in luminosity and cover a linear range of $-1.0 \dots +1.0$. We investigate star counts in the four CMDs $(u - g, g)$, $(g - r, g)$, $(r - i, r)$, and $(i - z, i)$. In order to show and compare each stellar population in all CMDs, the color and magnitude ranges are different in the different CMDs (see columns 2 and 3 of Table 6.1).

6.3.1 Luminosity function

Showing the magnitude distributions of different components, and comparing with observations, provide the directions to understand the shortcomings of the models. In Figure 6.2, the simulated photometric data are drawn with the SDSS data over plotted (error bars). The best prediction of the stellar number density for magnitudes fainter than 17^{th} mag is in the i and z band. The model gives good agreement with the data at the mid- and faint end of each band. A few significant discrepancies, however, appear clearly:

- In the u , g , i and z bands, predictions of stellar density are slightly higher than the data. The brighter the magnitudes are, the more obvious these differences are. The thin disk dominates at the bright end where the differences between predictions and data are the largest deviation (0.2 ~ 0.5 dex). At 150 – 450 pc the star counts are dominated by the thin disk. Therefore the thin disk is given a higher estimate of main sequence dwarfs ($Mg = 6^{th} \dots 8^{th}$ mag) by the Besançon model. This over-estimate is caused by the higher local density and larger scale height of the thin disk fitted using nearby stars.
- The contributions of thick disks have reached observed star counts at the bright ends of the u and g bands. This result implies that the prediction of thick disk is overestimated. At about 1 kpc or more, the thick disk population is expected to dominate the star counts. These facts means that giants, specifically luminosity classes III and IV, with absolute magnitudes of $Mg < 1$ mag are overestimated densities (see Section 4.3 on giants).
- The r band matches the data at only $16^{th} \dots 18^{th}$ mag. The model predicts fewer stars at $r > 19^{th}$ mag.

The giants (including sub-giants, giants, bright giants and super-giants) are plotted as open circles in Figure 6.2 to study their contributions. The number density of giants in general is lower than that of all stars of one magnitude or even two magnitudes fainter than 17^{th} mag in the i and z bands. The effect of neglecting giants is less than one-tenth of the contribution of all stars. The Hess diagrams of the giants will be discussed in Chapter 6.4.

6.3.2 Hess diagrams

Firstly we discuss the results in $(g - r, g)$ for a direct comparison with the Just-Jahreiß model (Just & Jahreiß 2010) and the TRILEGAL model (Girardi et al. 2005). The top right panel in Figure 6.4 shows that the relative differences of most regions are less than 50%. There are three regions in the CMD exceeding that level:

- The deep minimum at the lower right corner, where the star count predictions excess (compare middle and left panel in the top row) due to M dwarfs in the thin disk model (lower left panel). It seems that the $(g - r)$ color of the M dwarfs is too blue.
- The F turnoff regimes of the thick disk (lower middle panel) and the halo (lower right panel) are also blue-shifted by ~ 0.1 mag in $(g - r)$ leading to the significant features at $g = 16$ and $g = 20$ mag, respectively, in the difference plot.
- The maximum at the top right corner is a sign of missing K dwarfs in the model.

Differences of data and model arising from deviations of the density profiles in the model compared to the real profiles seem to be at a lower level and cannot be quantified here.

The blue part ($g - r < 0.5$) of SDSS data suggests more faint stars, Schultheis et al. (2006) supposed that these objects are compact faint galaxies or quasars erroneously classified as stars by morphological criteria. The similar problem is presented by Gao et al. (2011) but missed

stars are about 10% to 15% in the Just-Jahreiß model. There is a 85% to 90% star shortage caused by the problem of halo. M13 with $[\text{Fe}/\text{H}] = -1.54$ (Harris 1996) is adopted for the simulation of the halo by Just & Jahreiß (2010). Robin et al. (2003) assumed the halo is a single population with a metallicity of $[\text{Fe}/\text{H}] = -1.78$. The blue-shifts in the Hess diagram of the predicted halo is ~ 0.1 mag (see Section 3.2).

In the TRILEGAL model similar features of blue-shifted isochrones were observed. But in the TRILEGAL model, the deviations due to the parameter choice of the (strongly simplified) density profiles are comparable. Typical deviations between the data and the model are below 50%, slightly smaller than in the Besançon model. In the Just-Jahreiß model with observationally based MS properties the color offset in the Hess diagram does not occur. The model fits much better to the NGP data with typical deviations below 10 per cent.

In $(u - g, g)$ (see Figure 6.3), the deviations between the data and the Besançon model are much larger than in $(g - r, g)$. One reason is that the isochrones are even more blue-shifted by ~ 0.3 mag in $(u - g)$. Additionally the features in the number density distribution in the Hess diagrams are much wider in color in the observations compared to the model.

In $(r - i, r)$ (see Figure 6.5), thin disk dominates for $r - i > 0.8$ while the thick disk dominates for $0.3 < r - i < 0.7$. An interesting result is that the largest significant difference between the model and the observation is located at the connection of the populations of thin and thick disk caused by a gap for $0.75 < r - i < 0.85$ and $20 < r < 20.5$. On the other hand, we found that there is a pronounced gap at $r - i \approx 0.45$ in the MS of the thin disk which has no counterpart in the other colors. Additionally there is a turn-down of the MS in the thin and thick disks leading to missing stars at the bright red edge of the Hess diagram. The Hess diagram of $(i - z, i)$ (Figure 6.6) presents the best fit of the Besançon model and the SDSS data. In most regions of the CMD the difference is less than 30%.

Redder and brighter stars (disk M dwarfs) observed are more than that in the prediction by model. It suggests that the simulating luminosity function of the model has been underestimated (Schultheis et al. 2006).

6.4 Giants

Apart from MS stars, giants with luminosity classes I, II, III and IV (i.e., super-giants, bright giants, giants and sub-giants) provide the second-most important contributions to the number counts in the CMDs. The distribution of giants in the Hess diagrams helps to better understand the underlying stellar populations and age distributions. The top row in Figure 6.7 shows the distribution of giants only predicted by the Besançon model. The giants of thick disk and halo are well separated in luminosity (brighter and fainter than 17^{th} mag, respectively). The populations are clearly dominated by two color regimes: blue sub-giants (= end of F turnoff) and red giants at $(g - r) = 0.4 \dots 0.6$. A comparison to the fiducial sequences of globular clusters in An et al. (2008) shows that there may be a small blue-shift of the isochrones used in the Besançon model consistent with the results above. There are no giants redder than $(g - r) = 1.0$ expected in the metal-poor thick disk and halo components with $[\text{Fe}/\text{H}] < -1.0$. The most probable candidates for the missing stars at the upper right corner are giants of the

thick disk in the metallicity regime $-1.0 < [\text{Fe}/\text{H}] < -0.5$.

The lower row in Figure 6.7 shows the fractional contributions of giants to the total number density in the model. In the $(g-r)$ and $(r-i)$, there are areas exceeding 20% giants over the full luminosity range, which need to be taken into account for a complete model. In $(i-z, i)$, the giants are distributed more smoothly in color, they contribute less than 20% to the total number of stars and are relevant only in the limited color range of $-0.5 < i-z < 0.15$.

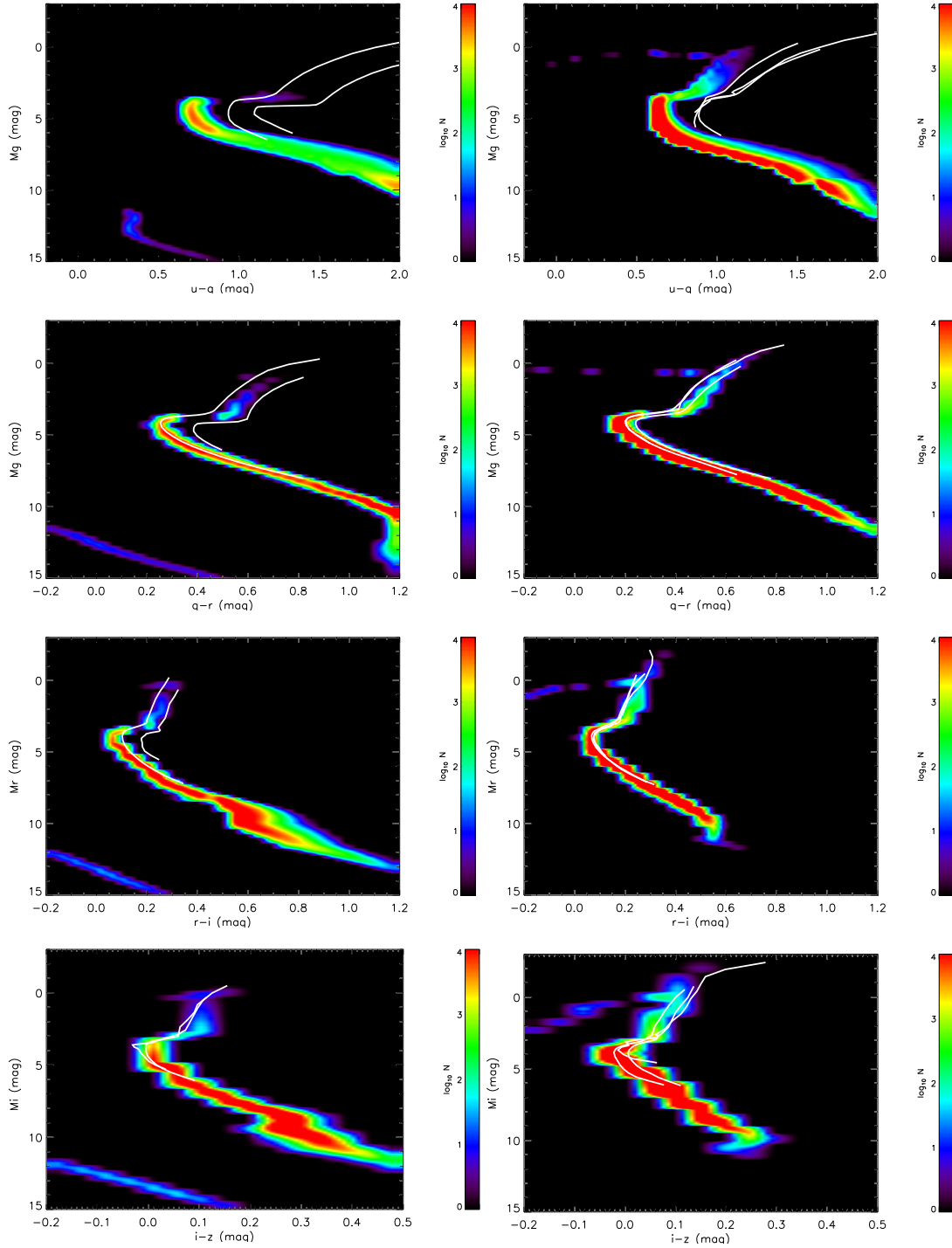


Figure 6.1: The color-absolute magnitude diagrams of thick disk and halo and the fiducial isochrones of globular clusters in $(g-r, Mg)$. The color Hess diagrams are the stellar distributions in $(u-g, Mg)$, $(g-r, Mg)$, $(r-i, Mr)$ and $(i-z, Mi)$ from top to bottom of thick disk (left column) and halo (right column) simulated by the Besançon model. The overplotted thick lines (white) are the An et al. (2008)’s fiducial isochrones based on observations of globular clusters. M5 (left) and M71 (right) are overplotted on the thick disk panels. M92 (left), NGC 4117 (middle) and M13 (right) are overplotted on the halo panels.

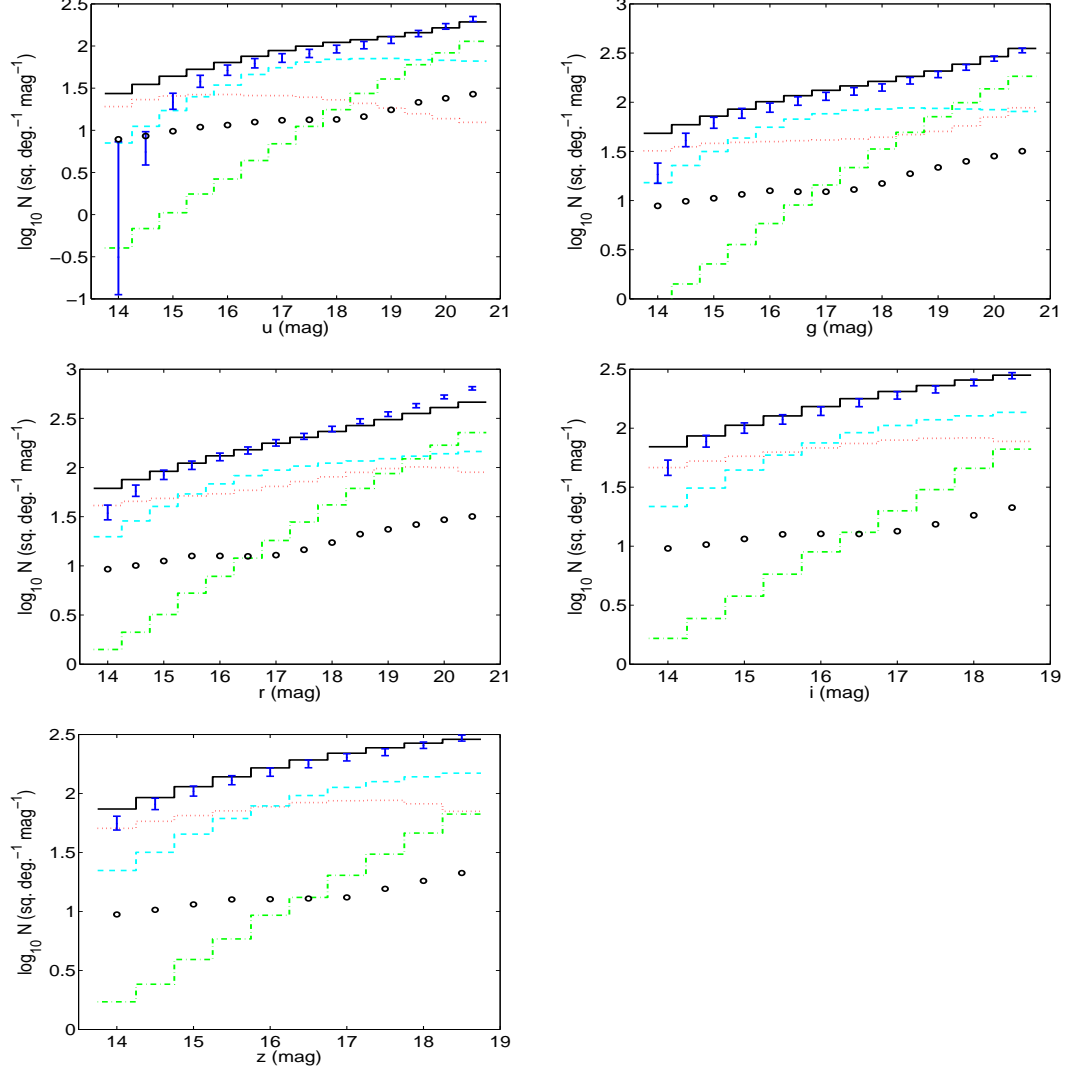


Figure 6.2: The distributions of apparent magnitude in the u , g , r , i and z bands. The thin disk, thick disk and halo are plotted as dotted lines (red), dashed lines (cyan) and dotted dashed lines (green), respectively. The solid lines (black) represent their sums. The open circles (black) stand for all giants in this volume limited by the color and the direction. The error bars (blue) show data from SDSS DR7 for comparisons. The samples of u and z band are limited to the color interval of $-0.2 \leq (u - g) < 2.0$ and $-0.2 \leq (i - z) < 0.5$, respectively. The boundaries of the other bands follow the colors range of the second column in Table 6.1.

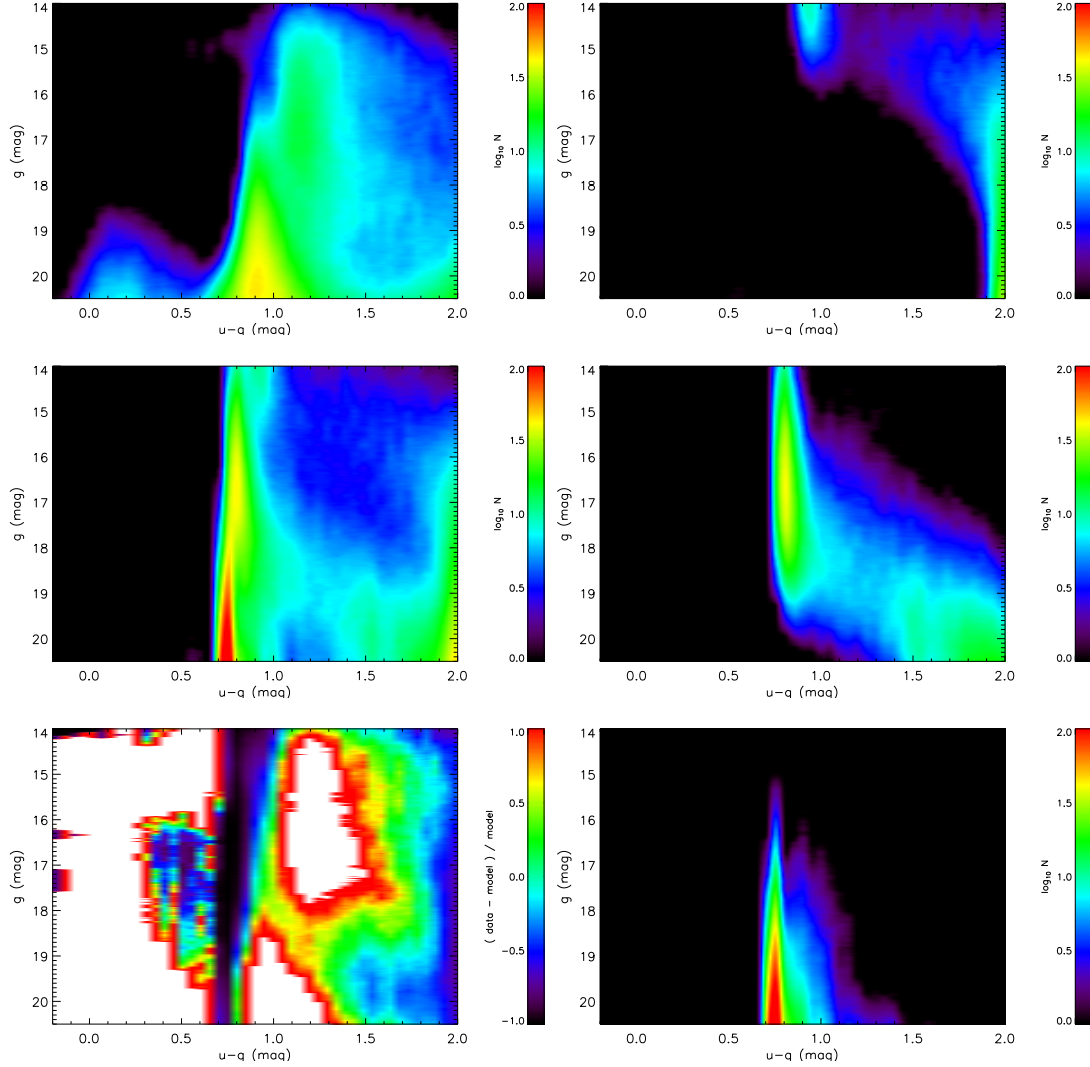
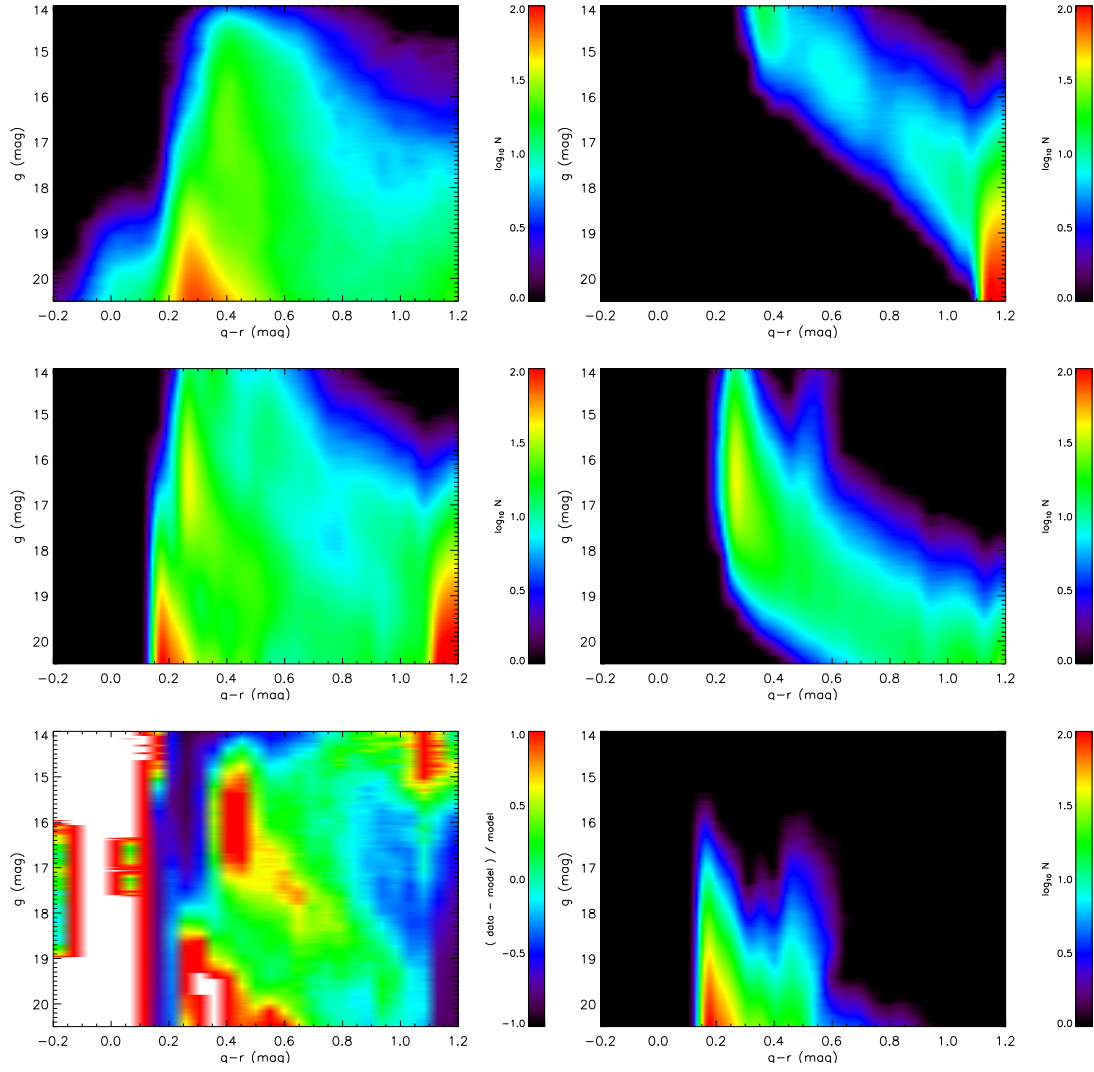


Figure 6.3: Hess diagrams of the Besançon model in $(u - g, g)$. The left three plots show the Hess diagram of the SDSS data, the model and the relative difference between data and model for the same conditions. The right panels show the Hess diagrams of the simulated three components of the Milky Way by the Besançon model from top to bottom: thin and thick disks and stellar halo. The Hess diagram covers the range of stellar density from 0 to 100 (purple to red) per square degree per 1 magnitude and 0.1 color magnitude interval. The difference plot covers the range of relative difference from -100% to 100% (purple to red). The boxes of apparent magnitude and color of these six plots are same (see Column 2 and 3 of Table 6.1).

Figure 6.4: Same as Figure 6.3 but as $(g-r, g)$ diagram.

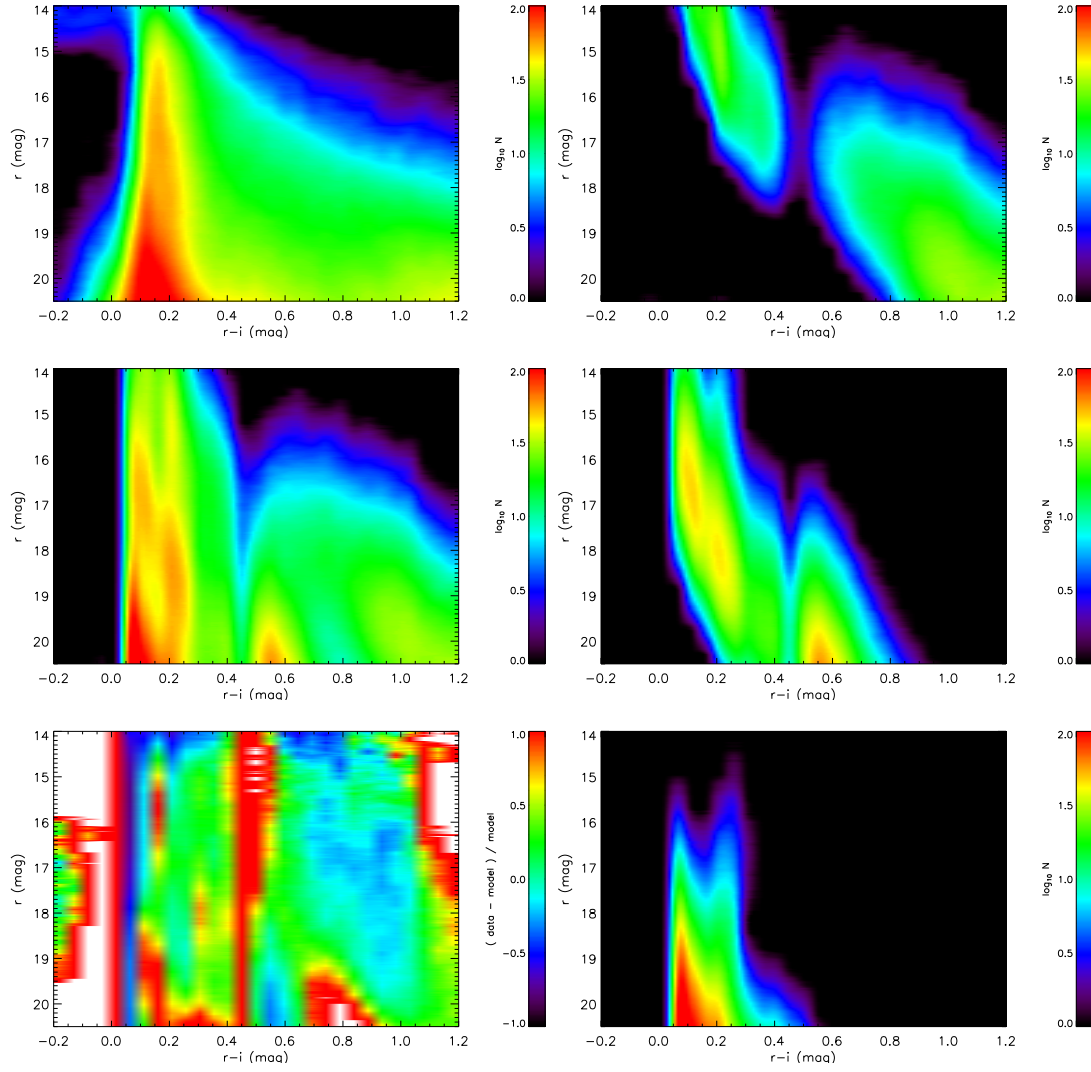
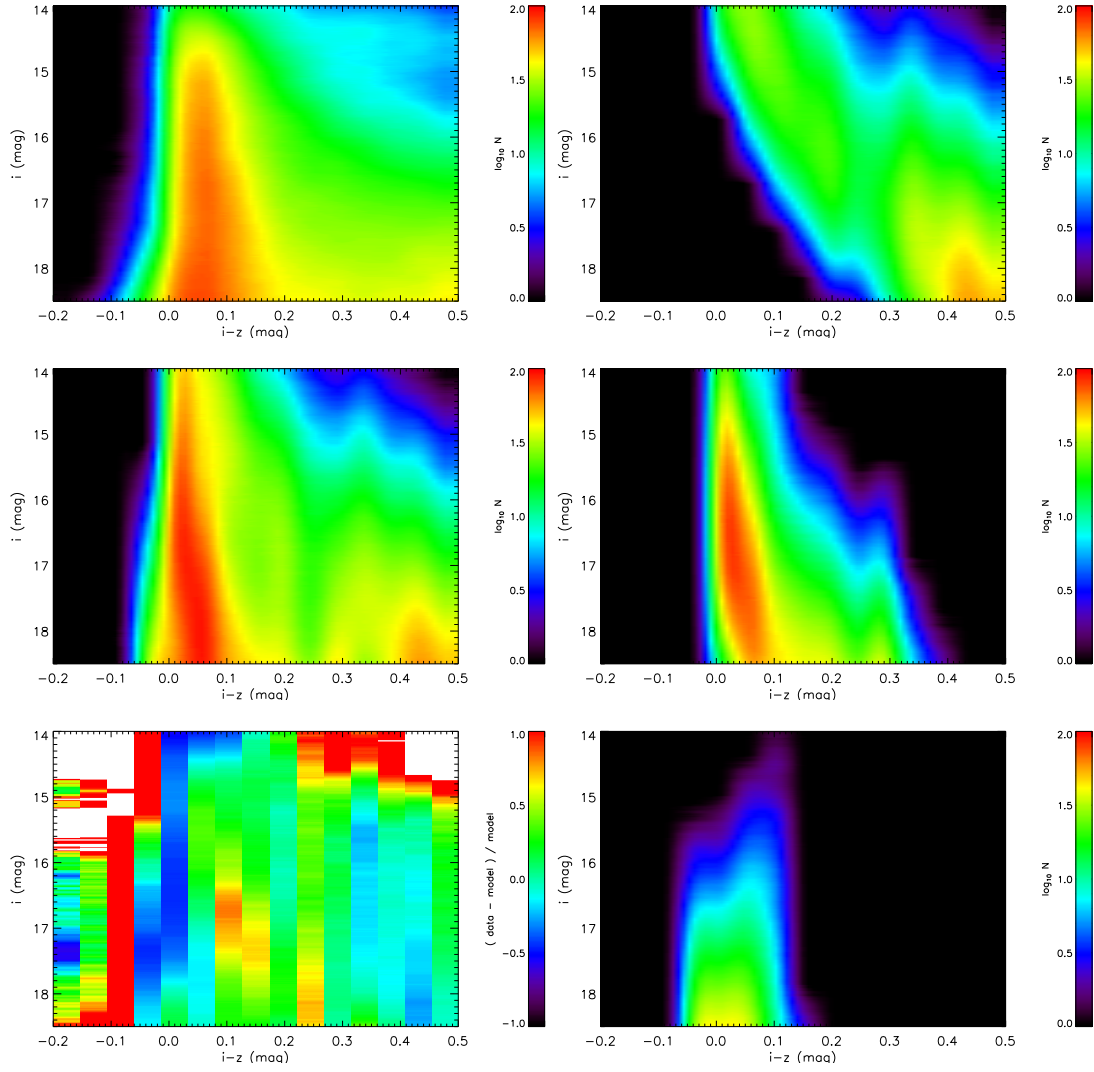


Figure 6.5: Same as Figure 6.3 but as $(r-i, r)$ diagram.

Figure 6.6: Same as Figure 6.3 but as $(i-z, i)$ diagram.

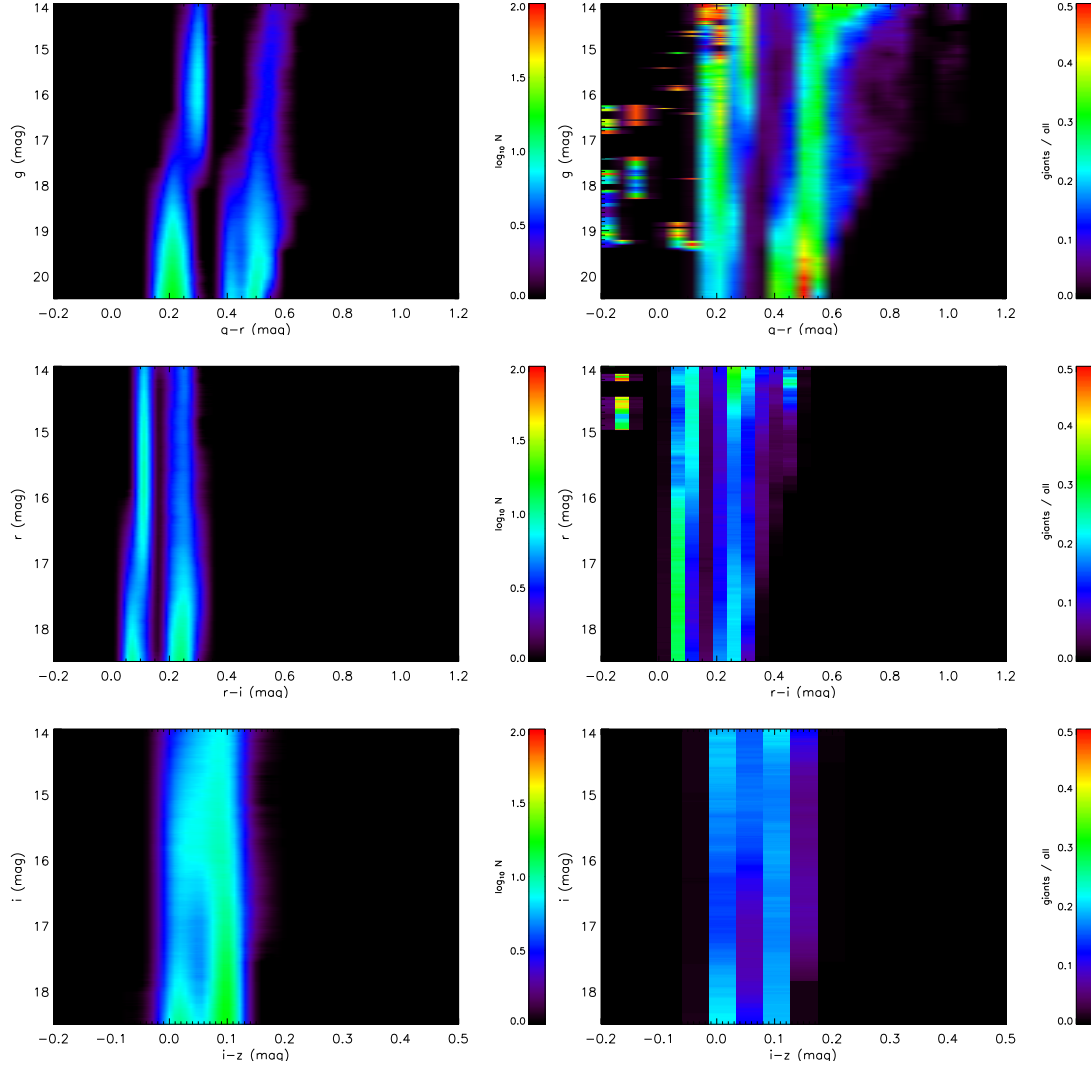


Figure 6.7: Hess diagrams of giants simulated by the Besançon model. The left panels are the Hess diagrams of giants in $(g-r, g)$, $(r-i, r)$, and $(i-z, i)$ respectively. The right panels are the relative ratios of giants to all stars simulated by the Besançon model. In the right panels, the zero values (black) indicate that there are no giant stars in those regions and “0.5” (red) indicates that giants account for a half of the total number of stars. The three color sets $(g-r, g)$, $(r-i, r)$ and $(i-z, i)$ are plotted from top to bottom.

“To command the professors of astronomy to confute their own observations is to enjoin an impossibility, for it is to command them not to see what they do see, and not to understand what they do understand, and to find what they do not discover.”

Galileo Galilei



The lower latitude fields

The longitude-dependent sub-structures and scale lengths of the disks do not need to be considered in the NGP field. The consideration deviations in different directions in the lower latitude fields are required in order to present the complete model. The low latitude disk model calibration is an important step in order to improve the Just-Jahreiß model. For lower latitude fields, more parameters need to be considered. The scale lengths of the disks should be fitted using lower latitude fields. Besides the NGP field, several low latitude fields are considered to test the Just-Jahreiß model and to determine the scale lengths of the disks. The best scale length pair of the disks requires the lower fields, which are able to constrain the over-density (and under-density) in the halo and the sub-structures in the disks.

7.1 The field selection

We planned a strategy to analyze lower latitude fields with a similar method. More comparisons will be done in order to obtain the difference between the models and the data in the detailed profile densities. The target fields are listed in Table 7.1. In order to show the expected over-density in the halo due to the stellar streams observed earlier, the width of the fields is limited to be 30° .

The lower latitude fields are used to test the effects of models. They include 24 mid-latitude small fields between 60° and 80° and a stripe between 20° and 30° . The NGP field plus 24 small fields cover the entire northern cap above $b = 60^\circ$ of the Galaxy. The stripe contains ten blocks located at two sides of the Galactic plane. Only five northern blocks are considered in the current work. The Galactic asymmetry can be investigated by this arrangement.

The small fields among the north Galactic cap are used to determine the best scale length pair of the thin and thick disks. The parameters of these small fields are listed in the first 24 rows of Table 7.1.

We do not select any fields below $b = 20^\circ$ since the reddening and extinction are too large to obtain the meaningful photometric data for our purposes (Figure 7.8).

Table 7.1: The low latitude fields selected for the test of the Just-Jahreiß model

Number	Name of field	b (deg)	l (deg)	Area (deg ²)	$\langle\chi^2\rangle$	$\langle\chi^2\rangle^*$
0	bp900_l0000_db050_d01800	[80, 90]	[0, 360)	313.3625	0.055	1.33
1	bp750_l0000_db050_d0150	[70, 80)	[-15, 15)	77.5472	2.44	2.11
2	bp750_l0300_db050_d0150	[70, 80)	[15, 45)	77.5472	2.50	2.26
3	bp750_l0600_db050_d0150	[70, 80)	[45, 75)	77.5472	2.43	2.38
4	bp750_l0900_db050_d0150	[70, 80)	[75, 105)	77.5472	2.35	2.32
5	bp750_l1200_db050_d0150	[70, 80)	[105, 135)	77.5472	1.87	1.90
6	bp750_l1500_db050_d0150	[70, 80)	[135, 165)	77.5472	1.76	1.77
7	bp750_l1800_db050_d0150	[70, 80)	[165, 195)	77.5472	1.89	1.78
8	bp750_l2100_db050_d0150	[70, 80)	[195, 225)	77.5472	2.42	2.05
9	bp750_l2400_db050_d0150	[70, 80)	[225, 255)	77.5472	1.68	1.55
10	bp750_l2700_db050_d0150	[70, 80)	[255, 285)	77.5472	2.66	2.41
11	bp750_l3000_db050_d0150	[70, 80)	[285, 315)	77.5472	2.47	2.15
12	bp750_l3300_db050_d0150	[70, 80)	[315, 345)	77.5472	2.63	2.22
13	bp650_l0000_db050_d0150	[60, 70)	[-15, 15)	126.6246	3.26	3.29
14	bp650_l0300_db050_d0150	[60, 70)	[15, 45)	126.6246	3.74	2.52
15	bp650_l0600_db050_d0150	[60, 70)	[45, 75)	126.6246	2.75	2.96
16	bp650_l0900_db050_d0150	[60, 70)	[75, 105)	126.6246	2.78	2.83
17	bp650_l1200_db050_d0150	[60, 70)	[105, 135)	126.6246	2.60	2.55
18	bp650_l1500_db050_d0150	[60, 70)	[135, 165)	126.6246	2.40	2.51
19	bp650_l1800_db050_d0150	[60, 70)	[165, 195)	126.6246	2.96	2.90
20	bp650_l2100_db050_d0150	[60, 70)	[195, 225)	126.6246	2.45	2.66
21	bp650_l2400_db050_d0150	[60, 70)	[225, 255)	126.6246	2.91	2.73
22	bp650_l2700_db050_d0150	[60, 70)	[255, 285)	126.6246	3.10	3.23
23	bp650_l3000_db050_d0150	[60, 70)	[285, 315)	126.6246	3.19	3.20
24	bp650_l3300_db050_d0150	[60, 70)	[315, 345)	126.6246	3.34	3.38
25	bp280_l1100_db010_d0010	[27, 29)	[109, 111]	3.5316	10.11	12.75
26	bp260_l1100_db010_d0010	[25, 27)	[109, 111]	3.5950	9.21	12.75
27	bp240_l1100_db010_d0010	[23, 25)	[109, 111]	3.6540	11.90	15.73
28	bp220_l1100_db010_d0010	[21, 23)	[109, 111]	3.7085	23.28	24.12
29	bp200_l1100_db010_d0010	[19, 21)	[109, 111]	3.7586	86.48	77.56

Note: The $\langle\chi^2\rangle$ and $\langle\chi^2\rangle^*$ are calculated using the partial and full range of Hess diagram: $\langle\chi^2\rangle$ is for $0.2 < g - r < 1.2$ and $\langle\chi^2\rangle^*$ is for $-0.2 < g - r < 1.2$. Field 0 stands for the NGP field that offers the contrast with the χ^2 values. Fields 1 to 24 are the 24 small fields used to find the best scale length pair of the disks. The last five rows are the stripe blocks below $b = 30^\circ$.

7.2 The scale lengths

A basic problem in the radial structures of the disks is the scale lengths of the thin and thick disks. In order to determine the scale lengths of the thin and thick disks, more fields with detailed directions are needed.

We select 24 small fields to fit the scale lengths of disks. Including the NGP field, 25 fields are used to fit the scale lengths of the disks. The Model A has been fixed (Chapter 4) as the fiducial parameter set via the fitting of the NGP field. This parameters set is used to calculate the χ^2 value for each scale length pair of the thin and thick disks in the 24 subsets at the lower latitudes. In order to obtain the best scale length pair, a grid of the thin and thick disks scale lengths are defined. Based on this grid, the χ^2 values are calculated for each pair.

The best fit of the local normalization was determined with the NGP field (see Chapter 4) and then the total χ^2 values of all 25 fields are calculated for each pair of scale lengths. The different results simulated by the model are compared with the SDSS data in Hess diagrams. The total χ^2 values are calculated to be the standard of the fits. The best scale length pair is found using the minimum χ^2 value. Figure 7.1 shows the distribution of χ^2 values based on different scale length pairs. The best scale length pair is $(r_d, r_t) = (1.5, 2.8)$ kpc.

The upper boundaries of the scale lengths in Figure 7.1 are not significant. Therefore our best scale length pair provides lower limits for the scale lengths of the disks. The scale length of the thin disk should be larger than our current value.

The best scale length of the thin disk is much smaller than the value in other studies. Many studies have been carried out on this topic. The scale length of thick disk is consistent with the TRILEGAL and Besançon models. The TRILEGAL model adopts the default scale length pair $(2.8, 2.8)$ kpc. The Besançon model uses the values $(2.53 \pm 0.11, 2.5 \pm 0.5)$ kpc. The Jurić model fits the result using $(2.60 \pm 0.52, 3.60 \pm 0.72)$ kpc, which is much larger than our result of the two disks.

We try to fit the scale lengths using the combination of the mid-latitude small fields and five low-latitude blocks. The result is $(r_d, r_t) = (0.8, 1.6)$ kpc, which is not significant because the area of the five blocks is too small to reflect the general structures of the disks. The five blocks are affected by the sub-structures in the disks (discussed in Chapter 7.3.2), which do not allow a reliable determination of the smooth background of the stellar contents.

There have been many attempts to fit the scale lengths using different combinations of the NGP, ring fields and stripe blocks. The determination of the scale lengths is a difficult problem, yet to be adequately resolved by the current fields. More significant results require more low latitude fields, which will be considered in the future.

7.3 Hess diagrams

Similar to the NGP field, we plot the Hess diagrams to show the detailed structures of the disks and halo and will try to improve those discrepancies between models and observations in the Hess diagrams. The χ^2 values in the Hess diagrams are calculated and are listed in the last two columns of Table 7.1.

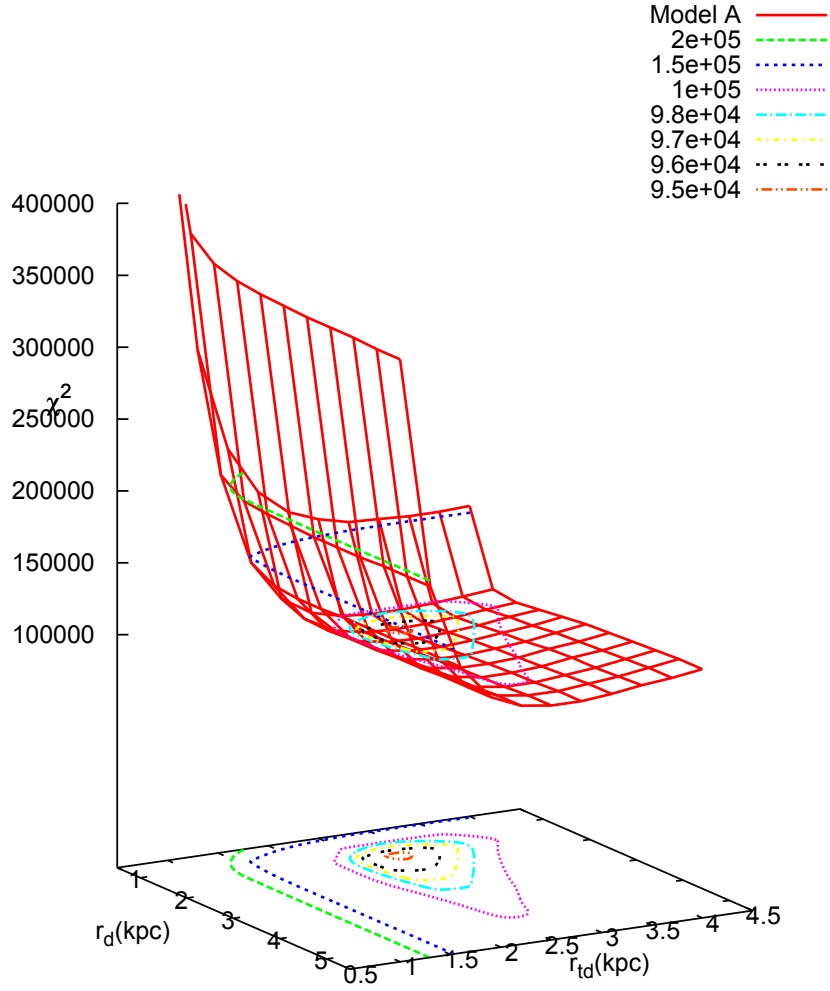


Figure 7.1: The total χ^2 distribution of with the best fit of northern Galactic cap fields. The x- and y-axis are the scale lengths of the thin and thick disks, respectively. The solid lines are the different χ^2 value grids based on the scale length pairs. The contours are plotted using different colors.

7.3.1 The ring fields

These 24 small fields are used to find the best scale length pair of the disks and to focus on the over-densities in the halo. The Hess diagrams of the SDSS data in these fields are plotted in Figures 7.2 and 7.3, which are sorted by the longitudes of the small fields. The Hess diagrams of the model are plotted in Figures 7.4 and 7.5. The star counts change continuously in the Hess diagrams. The Hess diagrams show the patterns that are similar to those in the NGP field, but the densities in the halo and the thick disk are larger than in the NGP. The minimum star counts of the halo are around the regions $l \sim 150^\circ$ for $b = 75^\circ$ and 65° . The maximum star counts of the halo are between $l \sim 330^\circ$ and 0° . That suggests that the axis of symmetry of the halo does not point to the Galactic center but to the direction of $l \sim 150^\circ \sim 330^\circ$.

The relative differences between the data and model for the 24 fields are plotted in Figures 7.6 and 7.7. We fix the parameters including the scale lengths determined in Chapter 7.2 to plot the Hess diagrams of the model for these fields.

There are large over-densities in the halo of the Hess diagrams between $l = 240^\circ$ and 300° (the first three panels in the third rows of Figures 7.6 and 7.7). These positions are affected by the Virgo stellar stream. Duffau et al. (2006) suggest that this stellar stream with a radial velocity excess came from the accretion of a dwarf satellite. Newberg et al. (2002) showed that the peak of the over-densities is at about $(l, b) \sim (279^\circ, 63^\circ)$ and that the stream covers large sky area. Vivas et al. (2001) used RR Lyrae stars to detect the over-density at $(l, b) \sim (314^\circ, 62^\circ)$ and named it the “12.4^h clump”. Duffau et al. (2006) considers this over-density block to be at about ~ 19 kpc from the Sun, which means that the over-density at $g \sim 20$ mag is caused by sub-giants and some turn-off stars, and the MS in the Virgo stream fainter than 21 mag that are located below the bottom edges of our Hess diagrams. The over-densities arise at $l > 225^\circ$ and disappear completely at $l > 315^\circ$, which provides the spatial constraints. Jurić et al. (2008) show the star counts of Virgo stellar stream in the 3-D space using the color-absolute magnitude relationship. Most of MS stars in the over-density locate at $20 < g < 22$ mag.

The large discrepancies at the bright red regimes (white-red corners) are caused by red giants in the disks. Most panels of Figures 7.6 and 7.7 show the discrepancies at the transitions between the thin and thick disks. The Just-Jahreiß model over-estimates the star counts at these ranges. That means that the density decreasing of old thin disk should be steeper.

7.3.2 The stripe 110

According to Figure 7.8, the extinction is very high at lower latitudes. The extinction values in the g band A_g can be 5 mag even more below $b = 10^\circ$. We select the stripe fields above $b = 20^\circ$, where the A_g values are between 1 and 2 mag.

The input parameter set with the scale length pair (2.8, 2.8) kpc is used to fit the other fields such as the stripe blocks since the scale length of the thin disk determined by the 24 smaller fields is not reasonable. The stripe at the Galactic longitude $l = 110^\circ$ and the Galactic latitude b between 20° and 30° is divided into five blocks with the half widths of longitude and latitude 1° (see the last five rows of Table 7.1). We use these five fields to test the effects of the

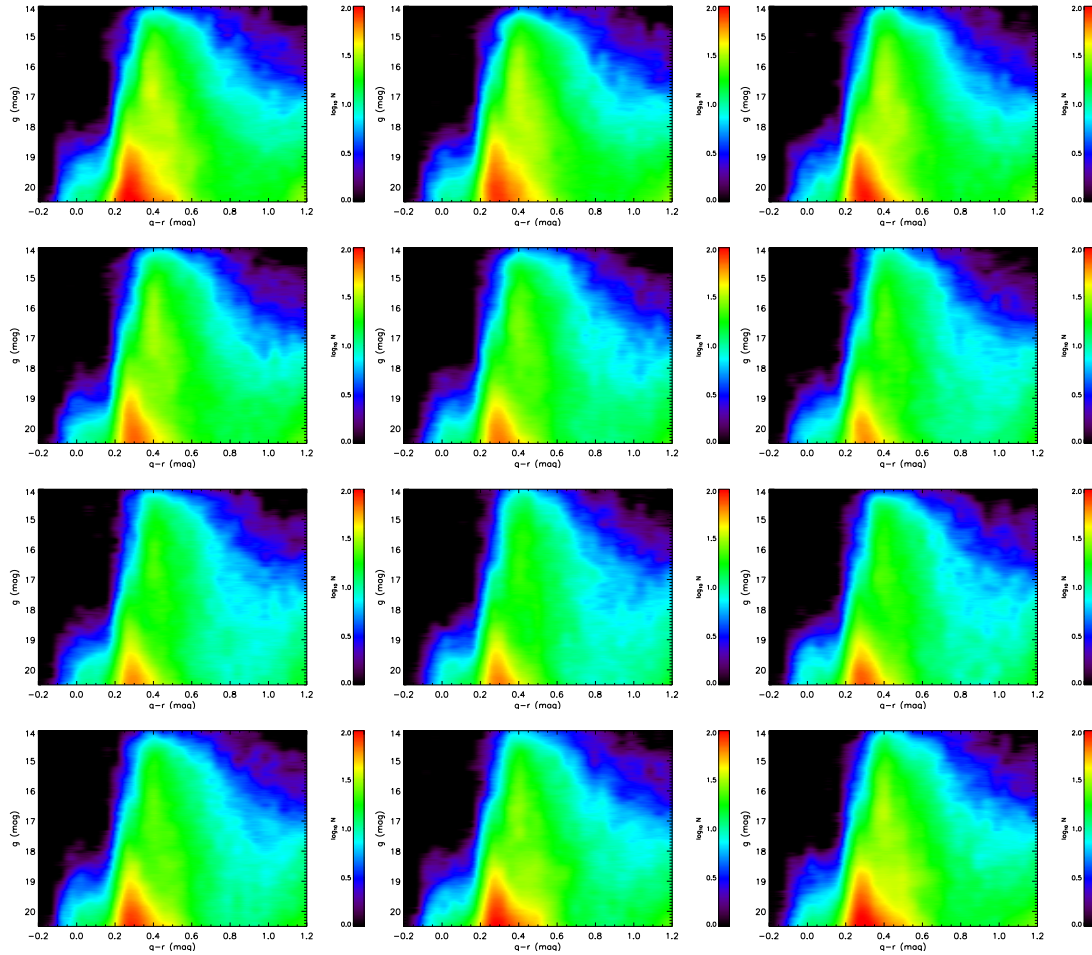


Figure 7.2: The Hess diagrams of the SDSS data for the 12 small fields between $b = 70^\circ$ and 80° . The panels are sorted by increasing longitudes. The middle panels in all rows are the $l = 0^\circ, 90^\circ, 180^\circ,$ and 270° respectively. The four rows point to the four directions from the Galactic center. The color coding and coordinate axis follow Figure 4.3.

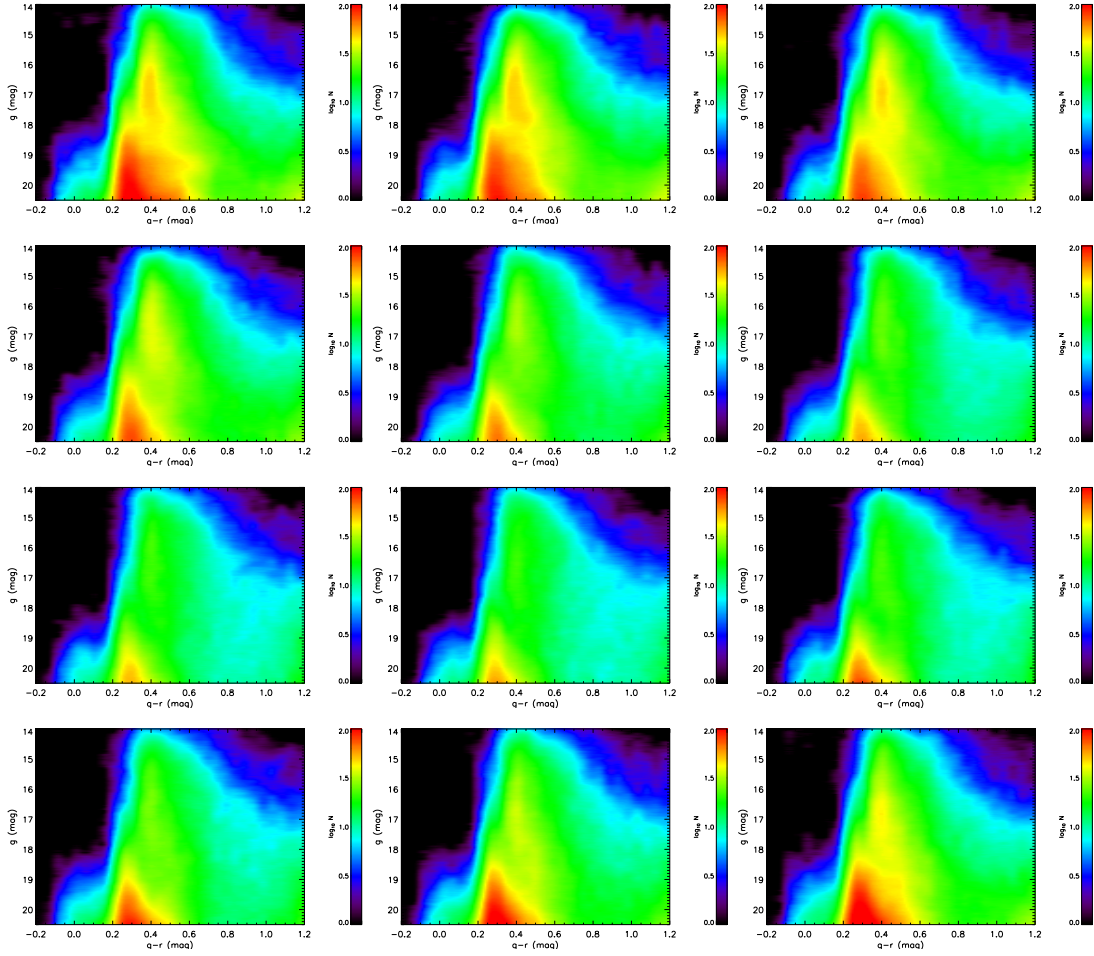


Figure 7.3: Same as Figure 7.2 but for the 12 small fields between $b = 60^\circ$ and 70° .

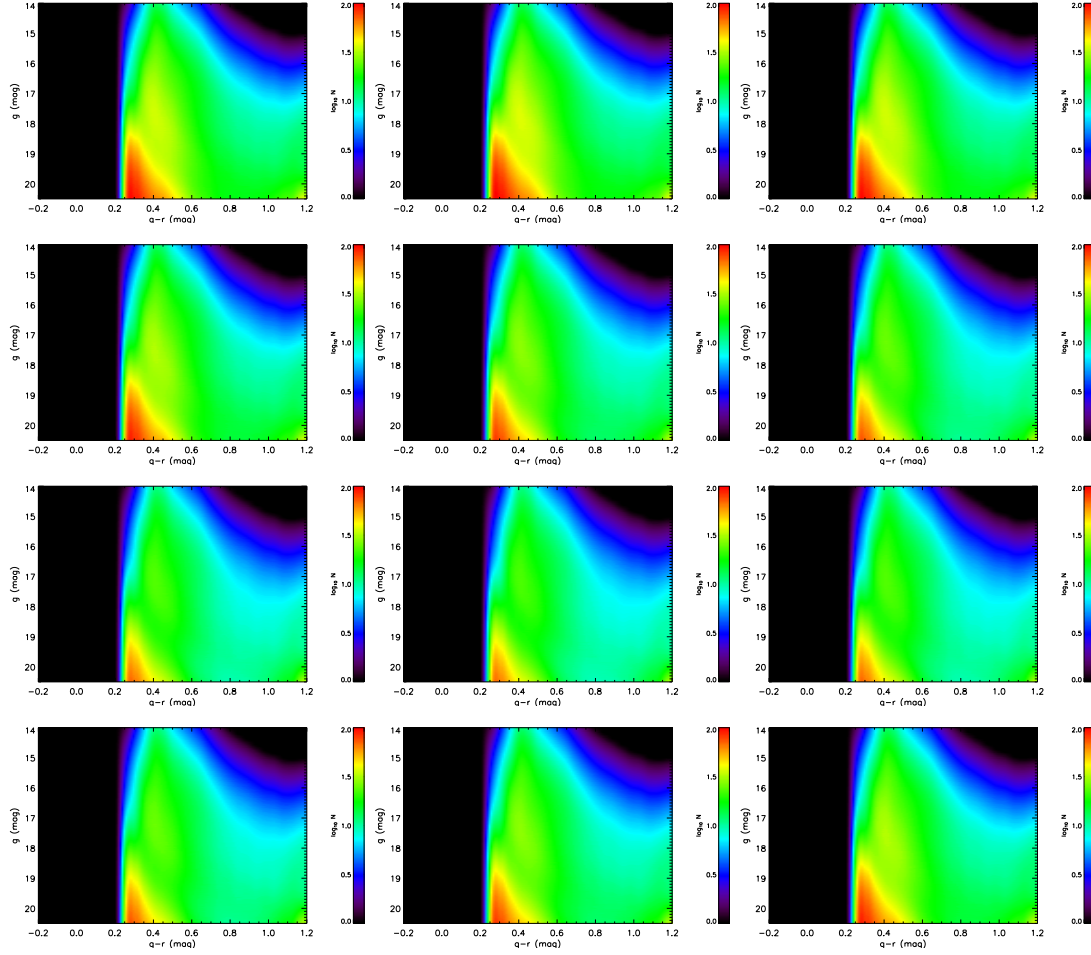


Figure 7.4: The Hess diagrams of the Just-Jahreiß model for the 12 small fields between $b = 70^\circ$ and 80° . The panels are sorted by increasing longitudes. The middle panels in all rows are the $l = 0^\circ, 90^\circ, 180^\circ$, and 270° respectively. The four rows point to the four directions from the Galactic center. The color coding and coordinate axis follow Figure 4.3.

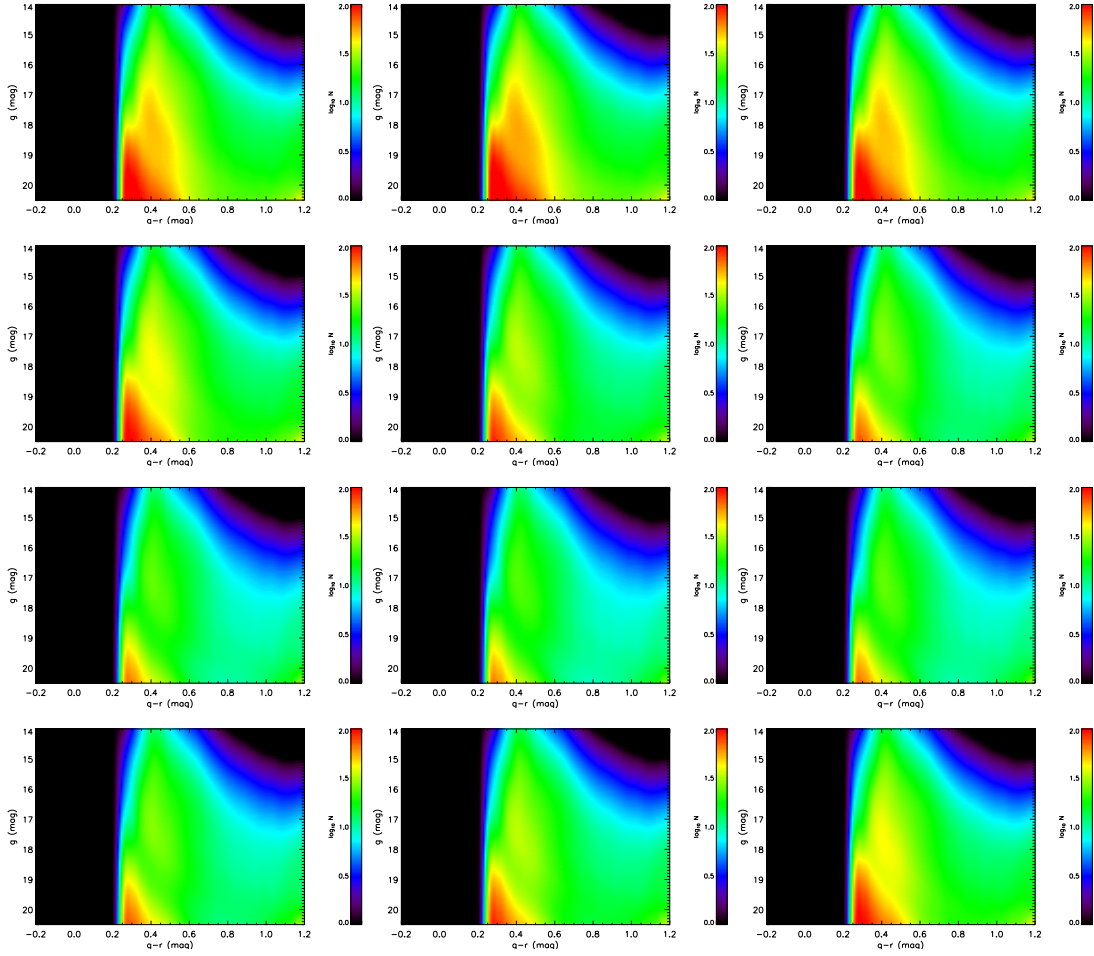


Figure 7.5: Same as Figure 7.4 but for the 12 small fields between $b = 60^\circ$ and 70° .

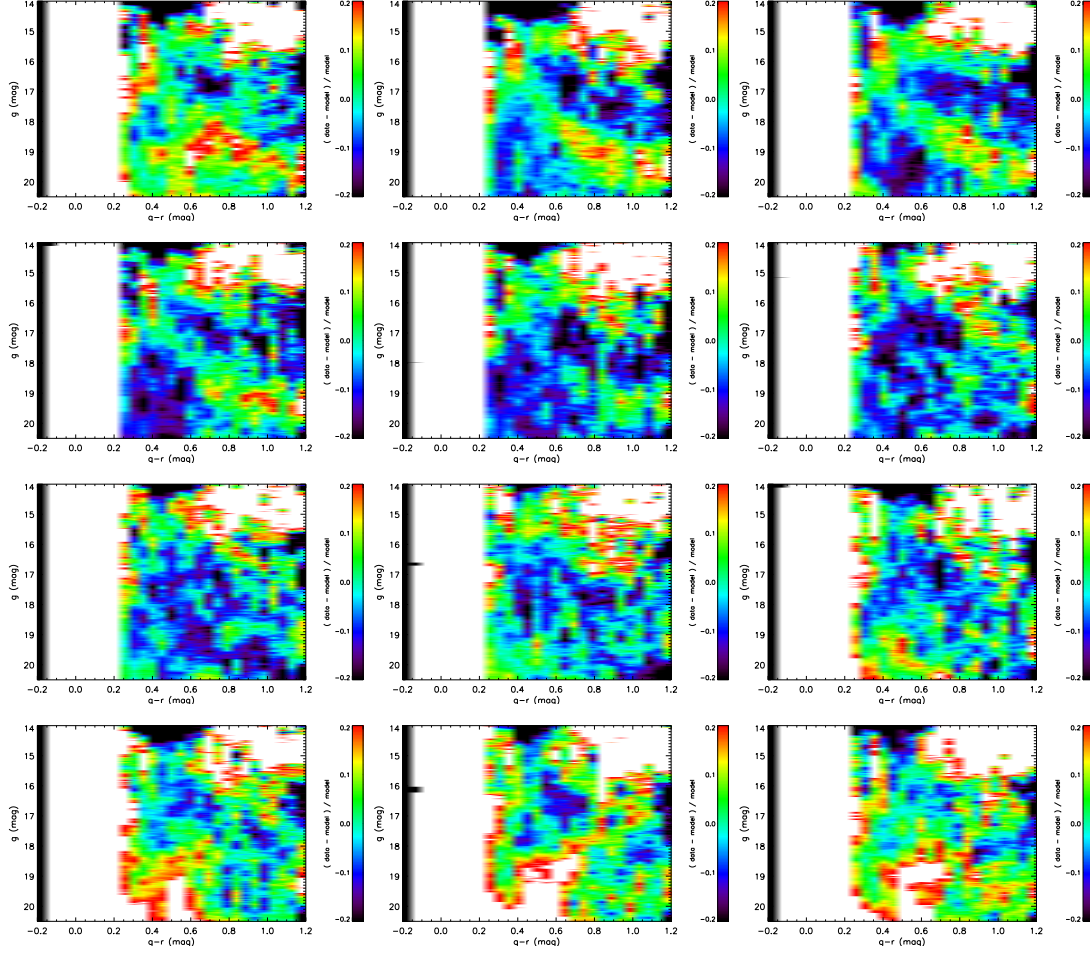


Figure 7.6: The Hess diagrams of the relative differences between the SDSS data and the Just-Jahreiß model for the 12 small fields between $b = 70^\circ$ and 80° . The panels are sorted by increasing longitudes. The middle panels in all rows are the $l = 0^\circ, 90^\circ, 180^\circ,$ and 270° respectively. The four rows point to the four directions from the Galactic center. The color coding and coordinate axis follow Figure 4.3.

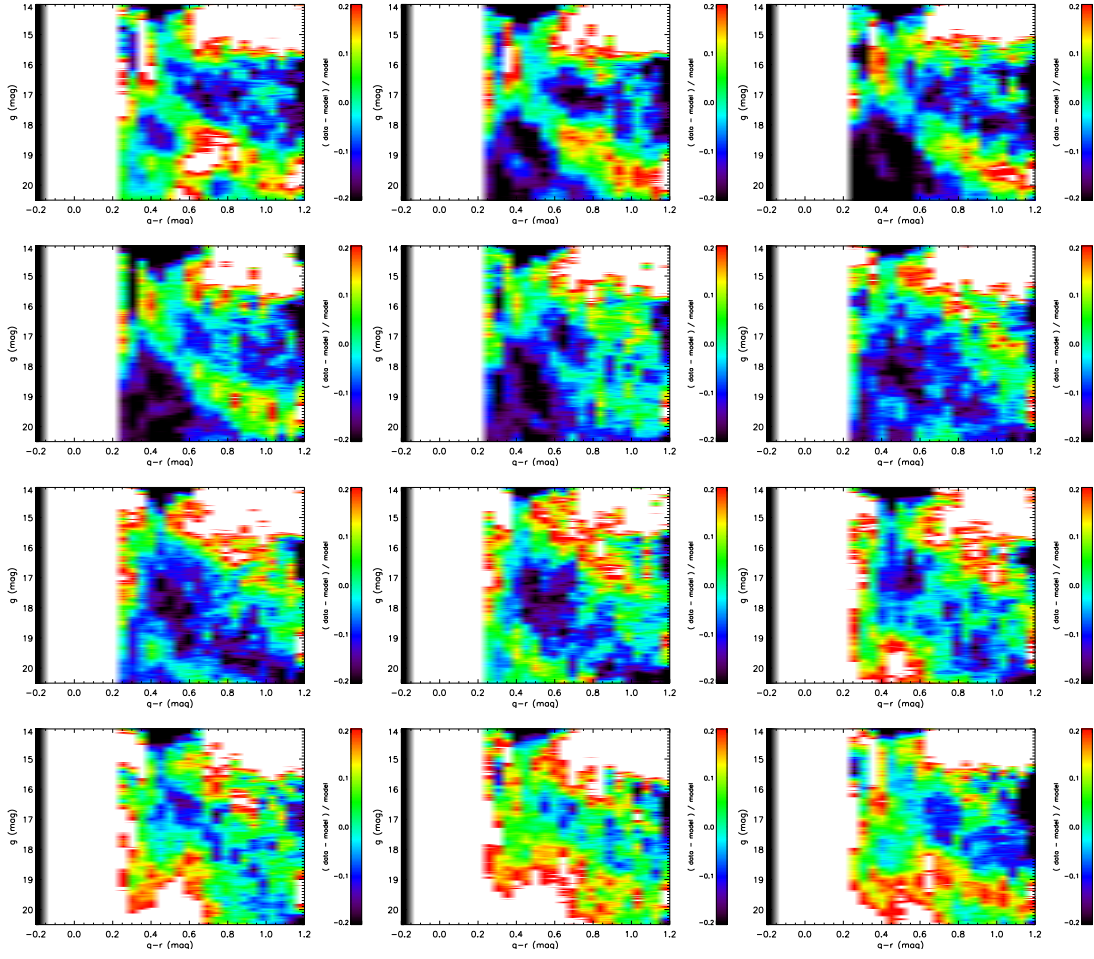


Figure 7.7: Same as Figure 7.6 but for the 12 small fields between $b = 60^\circ$ and 70° .

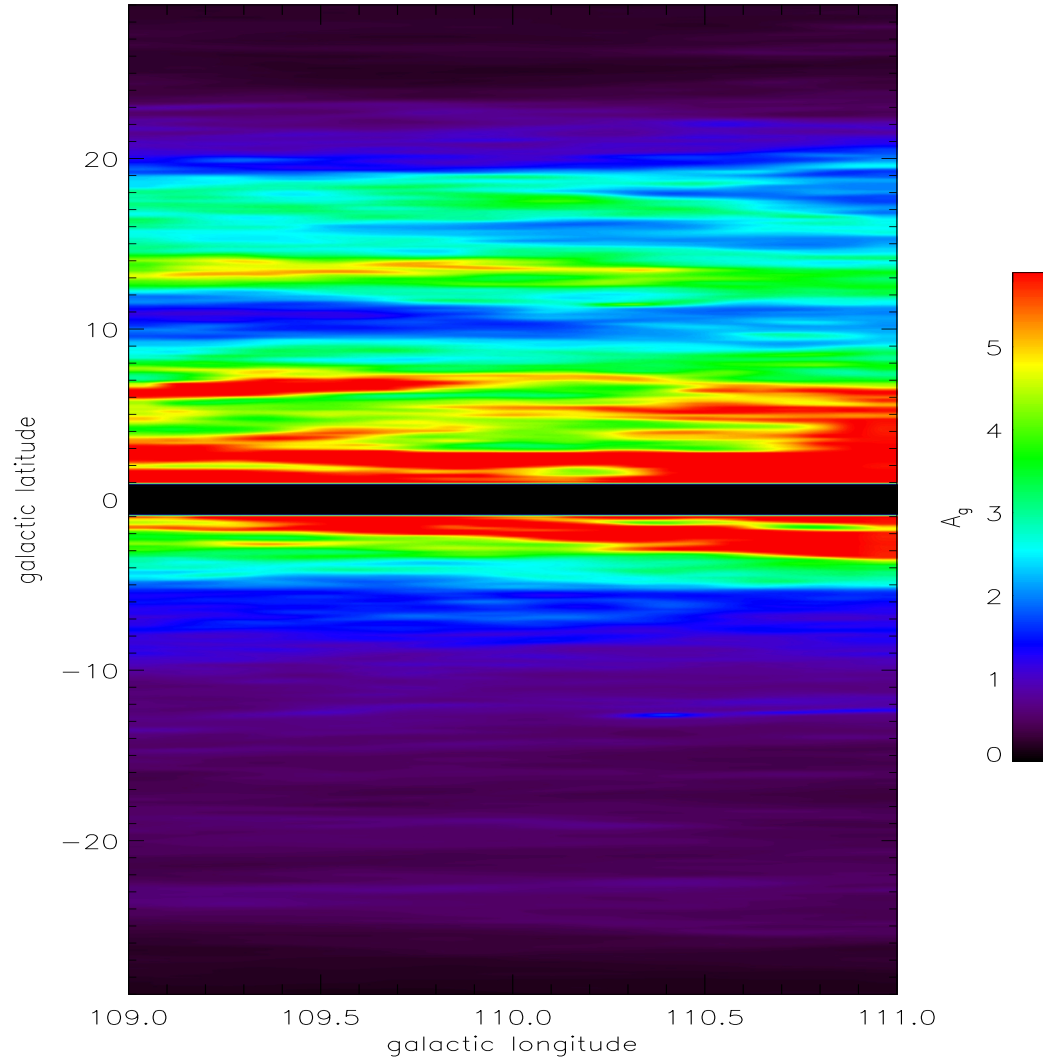


Figure 7.8: The extinction map based on Schlegel et al. (1998) at the low latitude and $l = 110^\circ$ field. The Galactic latitude b is between $+30^\circ$ and -30° and the Galactic longitude l is between 109° and 111° . The black band in the middle of this map around $b = 0^\circ$ is the Galactic mid-plane, where there are no a reasonable extinction data.

Just-Jahreiß model for the low latitude.

The parameters are adopted from the Just-Jahreiß Model A, which fits the NGP field very well. This model does not display a good match with the SDSS data at the stripe fields for all ranges of color. For the regimes dominated by the thick disk and halo the agreements between the model and the data are good.

The star counts at the stripe fields increase by an order of magnitude as compared to at the NGP field. In the Hess diagrams of the data and the models (the first and second columns of Figure 7.9) most of regimes contain more than 10^2 stars per 1 mag, 0.1 color mag, and square degree. The models are underestimated more than $\sim 40\%$ as compared to the data for the $g < 16$ mag. For the low-latitude field, i.e. $b = 27^\circ$, the distances of giants in the thin disk is less than 3 kpc. The apparent magnitudes of giants from 3 kpc away are brighter than 13 mag, which is out of the edges of our Hess diagrams. Therefore the large discrepancies in Figure 7.8 are caused by the giants in the thick disk.

Figure 7.10 shows the contributions of the thin disk, thick disk, and halo in the five stripe fields. The halo in the third column are shown the similar results. The star counts in the halo do not depend on the variation of the latitudes between 20° and 30° . The thin and thick disks in the first and second columns of Figure 7.10 show the continuous variations.

The disk model with the same vertical profiles does not fit the SDSS data in the stripe fields. The model overestimates the star counts in these fields seriously even though the model can be matched in the NGP and ring fields. The χ^2 values in the Hess diagrams of five blocks are listed in Table 7.1. These values are much larger than in the higher fields. They increase with decreasing latitude because the reddening is doubtful in the low latitude fields. We do not select the fields below $b = 20^\circ$ since the extinction cannot be determined very well.

The Hess diagrams of the relative differences between the data in the stripe and the models (see the third column of Figure 7.9) show two results: 1) the discrepancies increase in the Hess diagrams along with the decreasing latitudes, which means that the worse agreements are caused by the sub-structures in the disks, such as the spiral arms and radial variations of the density profiles. 2) the regimes dominated by the halo and the thick disk are relative better to match the data. That suggests that the main shortcomings are from the stellar populations of the thin disk and the transition between the thin and thick disks.

One of large discrepancies in the Hess diagram of $b = 28^\circ$ (the top right panel of Figure 7.9) is located at $0.45 < g - r < 0.75$ and $g \sim 15$ mag.

Correnti et al. (2009) and An et al. (2008) presented the color indices of the red clump with own metallicities in the $g - r$. The metallicity of the thick disk of the Just-Jahreiß model is between that of M71 and Pal5. The corresponding color range of the red clump is from 0.48 to 0.62, which is in the range of the large discrepancies in the Hess diagrams (Figure 7.9). Sarajedini (1999) and Groenewegen (2008) gave the absolute magnitude of the red clump in V and I , $M_V = 0.84$ and $M_I = -0.22$ mag, respectively. For the $b = 28^\circ$ field, the corresponding distance is estimated to be 6.3 kpc and the height above the Galactic mid-plane is about 2.9 kpc. This height belongs to the thick disk due to the volume factor, $z = 2$ to 3 kpc is the range where the maximum contribution along the line of sight is expected.

We test the effects of different scale lengths of the thin disk. The star counts of the thin disk are independent of the scale lengths of the thin disk. For the direction of $l = 110^\circ$ and

$b = 27^\circ$, the Galactocentric distance of a regime dominated by 1 kpc-height thin disk is about 8.9 kpc, which is larger ~ 1 kpc than the solar Galactocenter. The corresponding distance of the thick disk is 3 times larger than that of the thin disk due to the volume factor and the direction. The scale length of the thick disk is much more sensitive than the thin disk for the star counts.

The top right corners of Hess diagrams of stripe 110 (Figure 7.9) show that there should be more stars in the thin disk for the Just-Jahreiß model. The regimes with large discrepancies are larger and larger as the latitudes decrease. The reason is that line-of-sight directions of lower latitudes pass through longer paths in the thin disk, which contain more giants. The discrepancies in the thick disk and halo are larger than those in the NGP and ring fields, but the typical relative differences between the data and the model in stripe 110 fields are less than 30%, which is acceptable considering the unknown sub-structures, such as spiral arms and stellar streams in the disks.

The stripe 110 is the low limit of the significant photometric data in the SDSS filters. The Just-Jahreiß self-consistent model yields good results between $b = 20^\circ$ and 30° , where the average χ^2 values in the Hess diagrams are about ~ 10 in the higher three fields. The relative differences between the SDSS data and the Just-Jahreiß model for these low latitude fields are about $\sim 20\%$.

The sub-structures in the disks will be identified by the comparisons of more fields. The radial variations and the spiral arms need to be modeled by the other models. The southern blocks with the same area are needed to average the star counts at the both sides of the Galactic mid-plane. The average fields can reduce the large discrepancies in the Hess diagrams. The model of the low latitude fields, however, still requires a major improvement of structures of the disks. On the other hand, the photometric data at the low latitude fields are doubtful because of the larger and uncertain extinction. There is no this problem in infrared bands such as *JHK* of 2MASS, which can be used for testing of the Just-Jahreiß model at the lower fields. The further work will focus on the low latitude fields for the Just-Jahreiß model and the other models.

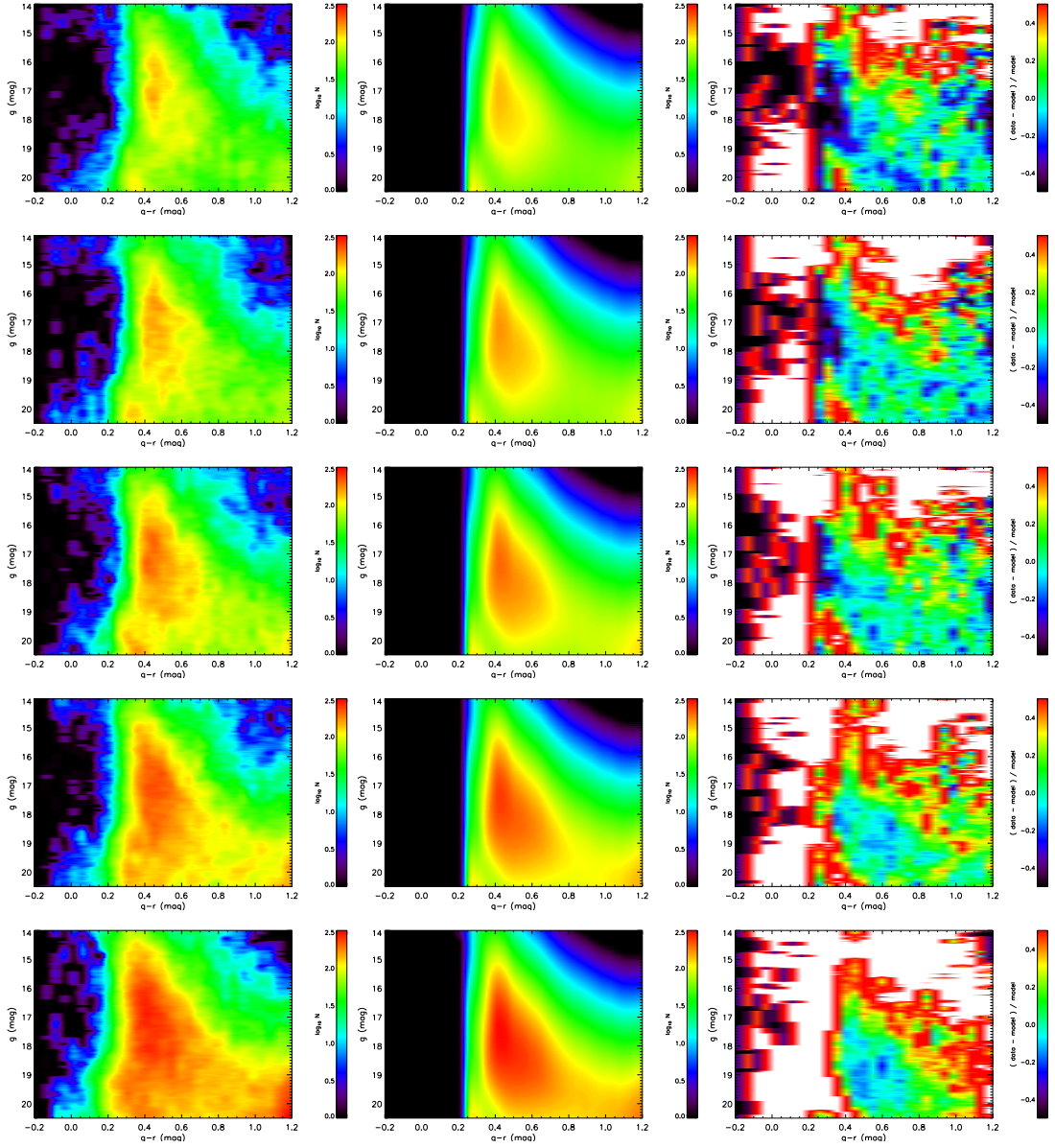


Figure 7.9: The Hess diagrams of the SDSS data, Just-Jahreiß models, and the relative differences between models and the data for the low-latitude fields. The five fields are shown as the five rows. From top to bottom panels the latitudes decrease. The Hess diagrams of the data, models, and relative difference between them are plotted from left to right column, respectively. The color coding and coordinate axis follow Figure 4.6. Notice the scales is different with the other figures. The maximum values (red color) are the logarithmic stellar density of 2.5 per mag per 0.1 color mag per square degree in the left and middle panels. The scales of the right panels are from -50% to $+50\%$.

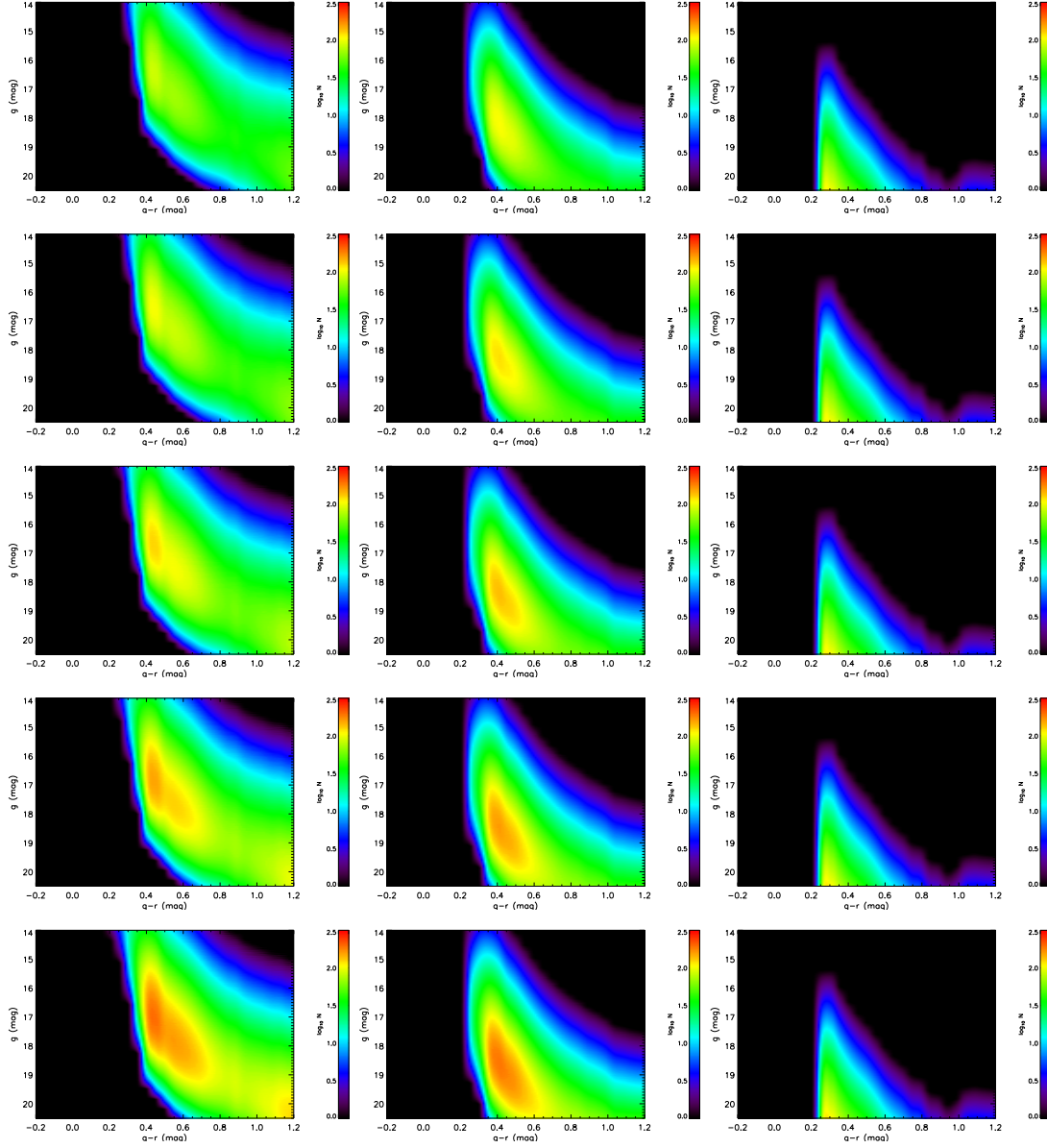


Figure 7.10: The Hess diagrams of three components (the thin and thick disks, and halo) at five different directions. From top to bottom, the Galactic latitudes are from 28° to 20° . The three columns are the thin disk, the thick disk, and the halo respectively. Notice the scales is different with the other figures. The maximum values (red color) are the logarithmic stellar density of 2.5 per mag per 0.1 color mag per square degree.

“I have always believed that astrophysics should be the extrapolation of laboratory physics, that we must begin from the present universe and work our way backward to progressively more remote and uncertain epochs.”

H. Alfvén

8

Summary and outlook

It is very important that comparisons between different Galactic models that never have been compared with SDSS observations are made. Little research has been conducted in applying the isochrones, luminosity functions, and Hess diagrams, to compare with the SDSS photometric data in the Milky Way. The SDSS provides quality stellar photometric data of most area in the Galactic northern hemisphere with different filters from previous systems. The Just-Jahreiß, TRILEGAL, and Besançon models provide the convenient ways to simulate and to predict the star counts at the specified volumes, which include the vertical and horizontal structures of local disk stellar populations. We can learn about the relationships between density profiles of disks and kinematics, the variations of structures in the disks and halo, the effects of different SFHs in the CMDs and luminosity functions, and the methods to test the models with the observed data.

The detailed comparisons help us to improve the models to match the observed data better. And on the other hand, the shortcomings of models allow us to improve our current theories on the stellar populations and the Galactic structures.

8.1 Methods

The main approach that analyzes the models is the comparison between the SDSS photometric data and the star counts simulated by the models in a given volume. The SDSS data are selected from several given fields, where the models simulate the mock stellar photometric catalogue. Isochrones of the thick disk and halo, luminosity functions of three components, and Hess diagrams, are used to present the results of the comparisons between models and actual data. During these processes, some necessary transformations and fits are required.

8.1.1 The data selection

We select several fields to compare the simulations of the models with the SDSS data. Since the NGP field does not reflect the horizontal variations and scale lengths of the disks, it is used to compare with the Just-Jahreiß, TRILEGAL, and Besançon models to show the vertical structures of the disks. The Just-Jahreiß model is calibrated and normalized using the NGP field. Besides the NGP, the 24 small fields in the north Galactic cap and 5 blocks below $b = 30^\circ$ are selected to test the Just-Jahreiß model. These lower latitude fields are adopted to find the

best scale length pair of the thin and thick disks. Some over-density spots and non-MS stars in the disks can be shown in the Hess diagrams of these lower fields.

The sky area simulated by the Just-Jahreiß model is limitless. The sample of data selected can be used for direct comparisons with the Just-Jahreiß model. The Besançon model is able to generate the full large field using given sky area in one single run. The TRILEGAL model only can simulate a sample within 10 deg^2 which forces us to run it many times to accumulate the necessary area of the fields and to reduce the random errors.

We select data from the SDSS DR7 stellar photometric catalogue (Abazajian et al. 2009) and fiducial isochrones of globular clusters (An et al. 2008) as our sample to compare with simulations of the models. The sky field is initially limited to the NGP. Later, other lower-latitude fields are used in Chapter 7. The de-reddened magnitudes *ugriz* of five bands are obtained directly from the catalogue of PSF photometry and the extinction map (Schlegel et al. 1998) at given directions. In order to avoid the affects of the saturation and low SNR, the *g* band is limited between 14 and 20.5 mag. The photometric error of the *g* band is limited within 0.2 mag. And the color index of $g - r$ is selected to range from -0.2 to 1.2 to cover turn-off, MS, and giants in the CMD.

We find that the DR8 updates the star/galaxy distinction and partial photometric data. We analyze the difference between the DR8 and DR7. The DR8 does not provide substantially better photometry and star/Galaxy distinction to improve star count on the CMD.

8.1.2 Transformations

The local density and color distribution used for normalization of different models adopt the *ugriz* photometric system of the SDSS. The isochrones of different components need to be expressed using the *ugriz* system. Based on the transformations by Just & Jahreiß (2008), Girardi et al. (2004), and Tucker et al. (2006), the Just-Jahreiß model and TRILEGAL models can use the entire range of SDSS system that covers a large area of tens of thousands of square degrees to compare with the data.

We generate the simulated catalogue from the Besançon model in the NGP field and transform the CFHTLS-MegaCam u^* , g' , r' , i' and z' to the SDSS u , g , r , i and z . The Besançon model with the SDSS colors is used to compare with the SDSS data. The filter conversions adopt a two-step process to transform the CFHTLS into the SDSS system.

8.1.3 Fits for the TRILEGAL model

The TRILEGAL model applies the simple and fixed density laws for the thin and thick disks and the halo. Either exponential or square hyper secant form with the heating law expressed by a power function can be selected. The Just-Jahreiß, Besançon, and Jurić models have different density profiles, which need to be fitted in order to apply their structural parameters in the forms of the TRILEGAL model.

For the Just-Jahreiß model, the self-consistent density profiles of disks cannot input into the TRILEGAL model directly because the TRILEGAL interface provides only a few specific parameters such as local densities and scale heights. The scale heights and the local densities

of the thin and thick disks are fitted using the exponential and sech^2 respectively. The form with smaller χ^2 is selected to be the input form in the TRILEGAL model.

Robin et al. (2003) showed that the density profile of the thick disk is a function of height z . The piecewise-defined function with the local density and scale height is fitted using two forms of the TRILEGAL respectively. For the thin disk of the Besançon model, seven sub-populations with own age ranges and scale heights, are presented in Robin et al. (2003), which are accumulated using the local densities as the weights and are fitted using the power law of the TRILEGAL to obtain the input parameters for TRILEGAL heating law.

For the halo, the three models adopt power laws with different power indexes as their density profiles. The TRILEGAL model requires an oblate spheroid to input as the density law of the halo. Three different power laws are fitted to become the forms of the oblate spheroid and to input the TRILEGAL model.

8.1.4 The isochrones

An et al. (2008) presented several globular clusters that were observed by the SDSS. We calculated the de-reddened magnitudes for them to determine the absolute magnitudes and intrinsic color indexes using Harris (1996) color excess parameters $E(B - V)$ and the distance modulus. The mean ridges of the sequences in the CMDs stand for the fiducial isochrones of globular clusters with own metallicities, which can compare with stellar populations of models in the CMDs.

The mean ridges of sequences in the CMDs of the globular clusters as the fiducial isochrones provide the standard to compare the simulated stellar populations in the CMDs. We select the different clusters with different metallicities to overplot the populations of models with similar metallicities in the CMDs. The fiducial isochrones of clusters as the standards in the CMDs can show the offsets of the stellar populations simulated by the models. The range of metallicities of 17 clusters is from -0.73 to -2.29, which covers the thick disks and halo of all different models in this thesis.

8.1.5 The luminosity functions and Hess diagrams

In DR7 database we get 274,519 stars following our selection rules in the NGP field. The average stellar density is 9.63 stars per square degree per magnitude and per 0.1 color magnitude in the area of 313.3626 deg^2 .

The apparent magnitude distributions (luminosity functions) of the data and the models are compared. We compare the g and r bands for the Just-Jahreiß and TRILEGAL models, the u , g , r , i , and z bands for the Besançon model. The luminosity functions of the data are limited within the given color range $-0.2 \leq g - r \leq 1.2$. The luminosity functions of the models are divided into three components to show: the thin disk, thick disk, and halo. The total contributions of three components are compared with the SDSS data. The contributions of single components show the ranges that are dominated by the specific populations. The agreements of luminosity functions between the data and the models are used in previous studies, which did not adopt the Hess diagrams to show more fully details of the models.

We plot the Hess diagram using $u - g$, $g - r$, $r - i$, and $i - z$ for the Besançon model, and using $g - r$ for the Just-Jahreiß and TRILEGAL models. The Hess diagrams are useful tools to show the detailed differences between the data and the models in the CMDs with the relative star counts. We plot the Hess diagrams of the data, models, relative difference between the data and models, and the distributions of χ^2 for all models. The shortcomings of the models are shown in the smoothed Hess diagrams. The over-density and under-density in the Hess diagrams show the shortcomings of the models and the sub-structures above the smooth background of the data. The qualities of models are compared with each other using the total χ^2 values in the Hess diagrams. The Hess diagrams are our final standards to evaluate the models.

8.2 Main results

The basic parameters of the Just-Jahreiß, TRILEGAL, and Besançon models are listed in Table 8.1 with their χ^2 values which are determined by the comparisons between observed and simulated Hess diagrams.

The brief conclusions of this thesis can be summarized in this section. In summary, we discuss three Galactic models: the Just-Jahreiß, TRILEGAL, and Besançon models and reference the Jurić model. We compare them with SDSS photometric data at the NGP field using *ugriz* system, respectively. The Just-Jahreiß model has a best fitting presentation “Model A” as our output results. The input sets of the TRILEGAL model are from 5 different sources: the default parameters of web interface, the fits of the Just-Jahreiß model, the fits of the Besançon model, the fits of the Jurić model, and an optimization set with better performance. The Besançon model has fixed input parameters and only can output a result for a given volume of magnitude, color, direction, and area of the field limit. Because of these differences in the structures of the models, we deal with them with different points of approaches.

8.2.1 The Just-Jahreiß model

We have used four different parameter sets for the Just-Jahreiß model with different SFRs of the thin disk, which fit the local kinematics of the MS stars and compared the star count predictions for the NGP field with $b > 80^\circ$ of the SDSS. For the thin disk we applied the absolute magnitudes of the local MS as determined in Just & Jahreiß (2008). A self-consistent isothermal thick disk and a simple stellar halo model are added to complete the contributions of the MS stars to the star counts. We use the local normalization of thin disk, thick disk and halo in each color bin as free parameters and minimize χ^2 in the Hess diagram over a large color-magnitude range in the $(g - r, g)$.

The Just-Jahreiß model has been normalized at the NGP field. All models can match the observed Hess diagram in the F-K stars regime better than $\pm 20\%$. The χ^2 value of “Model A” is the best simulation with only $\pm 5\%$ deviation in the Hess diagrams for the NGP field. The best fitting scale height of the thick disk is 800 pc and the power law $\alpha_t = 1.16$ in the density profile $\text{sech}^{\alpha_t}(z/\alpha_t h_t)$. Based on the fitting of local stellar color distribution, we give

Table 8.1: The comparisons between the basic parameters of the Just-Jahreiß, TRILEGAL, and Besançon models

Parameters	Units	Just-Jahreiß	TRILEGAL-optimizing	Besançon
$\ln < \chi^2 >$	-	-2.9	0.29	2.8
$\rho_{0,d}$	$M_{\odot} \text{pc}^{-3}$	0.037	-	0.0394
$\Sigma_{0,d}$	$M_{\odot} \text{pc}^{-2}$	29.4	50	-
$h_{d,\text{max}}$	pc	670	459	-
$\rho_{0,t}$	$M_{\odot} \text{pc}^{-3}$	0.0022	0.0014	0.00134
$\Sigma_{0,t}$	$M_{\odot} \text{pc}^{-2}$	5.3	4.2	-
h_t	pc	800	750	800
$\rho_{0,h}$	$M_{\odot} \text{pc}^{-3}$	0.00015	0.0001	0.00000932
α_h	-	-1.5	-	-2.44

Note: This table lists the basic parameters including three components of the Just-Jahreiß, TRILEGAL, and Besançon models. The $\ln < \chi^2 >$ values are the logarithmic normalized χ^2 values covering the color range of $0.2 < g - r < 1.2$ in the Hess diagrams in $(g - r, g)$. The $\rho_{0,d}$, $\rho_{0,t}$, and $\rho_{0,h}$ are the local stellar densities of the thin and thick disks and the halo. The $\Sigma_{0,d}$ and $\Sigma_{0,t}$ are the local stellar surface densities of the thin and thick disk. The $h_{d,\text{max}}$ and h_t are the maximum scale height of the oldest sub-population of the thin disk and the scale height of the thick disk. And the α_h is the index of the power law of the halo.

the density profile of each sub-population with its own age. The power law of stellar halo is fitted to get the minimum χ^2 value: The flatness $b = 0.7$ and the power index $\alpha_h/2 = -1.5$.

All models match the observed number densities better than $\pm 20\%$ proving the reliability of the thin disk density profiles by the self-consistent disk models in the range of $|z| < 1$ kpc. The derived local normalization are consistent with the star count data of the CNS4 in the solar neighborhood. The χ^2 analysis shows that Model A is clearly preferred with systematic deviations of a few percent only. The SFR of Model A is characterized by a maximum at an age of 10 Gyr and a decline by a factor of four to the present day value of $1.4 M_{\odot}$ per square pc per Gyr. In the thin disk the current fraction of stars older than 8 Gyr is with 54% significantly higher than for models B, C, and D. Especially Model C with a constant SFR and Model D with a disk age of 10 Gyr can be ruled out. That suggests that a high fraction of old stars in the thin disk are very important to create the better Hess diagram.

The thick disk can be modeled very well by an isothermal single stellar population with older age and higher velocity dispersion than the thin disk. The density profile can be approximated by a $\rho_{t,0} \text{sech}^{\alpha_t}(z/\alpha_t h_t)$ function. For Model A, the power law index of $\alpha_t = 1.16$ is determined from best fitting which is in-between an exponential density function and a squared hyperbolic secant law that corresponds to an isolated isothermal disk. The exponential scale height (the height at $1/e$ density) is $h_t = 800$ pc corresponding to a vertical velocity dispersion of $\sigma_t = 45.3$ km/s. About 6 percent of the stars in the solar neighborhood are thick disk stars. In Jurić et al. (2008) the stellar density distribution in the Milky Way based on SDSS star

counts was fitted by exponential thin and thick disk profiles. The result is 900 pc and is much larger than the Just-Jahreiß model, which balances the flattening of the profile at low z .

The results do not depend significantly on the filter transformations that are tried in Just et al. (2011) for the local MS nor on the smoothing of the data in luminosity. For the future an extension of the model to include turn-off stars in more detail and the contribution of giants as well as a higher resolution in color at the blue end would be very useful. We also plan to apply the model to lower Galactic latitudes in order to determine radial scale lengths of thin and thick disk as well as radial gradients in the stellar populations.

The Just-Jahreiß model is reasonable and credible to predict the star counts in the NGP field in different color and luminosity ranges. The fully self-consistent model with MS stars can match the SDSS data in the NGP very well. The local star counts can be normalized to calculate the stellar fractions of different populations. The population of stars of given color and luminosity can be estimated via the fractional density profiles. The success of the Just-Jahreiß self-consistent model in the NGP field proves that

- The thin disk is approximated by a set of isothermal sub-populations with own ages and velocity dispersions. Our best Model A shows that a star formation peak was at 10 Gyr ago, and the age of the oldest sub-population in the thin disk is about 12 Gyr.
- The thick disk can be modeled very well by an old single population, which is approximated by a $\text{sech}_t^\alpha(z)$ in the vertical direction. This result is different from the isolate isothermal disk with the sech^2 profile.
- A simple power law as the profile of stellar halo can match the NGP field very well except the range redder than $g - r = 0.2$.

We find that there are some shortcomings in the models to show the discrepancies in the Hess diagrams

- The white red corner at the top right of the Hess diagram suggests that the giants cannot be neglected at this regime.
- The over-density at the transition between the thin and thick disks implies that the oldest sub-population in the thin disk should be improved to supply the lack of star counts.
- No model generates enough stars redder than $g - r = 0.2$, where are dominated by the BHB, BS, and mis-classifications of galaxies.

In general the Just-Jahreiß model with 5% relative differences excellently simulates the vertical structures of the disks using the fully self-consistent method. A few discrepancies that are caused by the giants were expected to show in the Hess diagrams.

8.2.2 The TRILEGAL model

In this study we compared star count predictions generated with TRILEGAL of five different models simulating the NGP region to photometric data of this region from the SDSS. We

measured the quality of the fit by a χ^2 determination of the Hess diagrams in $(g-r, g)$, i.e., the star count distribution in the CMD. As a comparison we refer to the Just-Jahreiß model (model A in Just & Jahreiß 2010; Just et al. 2011) with $\langle\chi^2\rangle = 0.055$ corresponding to a typical relative deviation between data and model of 5%.

The web interface of TRILEGAL allows a restricted choice of input parameters and functions for the Galactic components. We compared the default input set (lacking a thick disk component) with best-fit adjustments of three other Galaxy models from the literature, namely the Just-Jahreiß model (Just & Jahreiß 2010), the Besançon model (Robin et al. 2003), and the model of Jurić et al. (2008). We found that the default set reproduces best the luminosity functions in the g and r band. The $\langle\chi^2\rangle = 1.94$ from the Hess diagram analysis is slightly worse than that based on the Jurić model with $\langle\chi^2\rangle = 1.76$. All of these models show a typical discrepancy of $\sim 30\%$ in the Hess diagram, which is significantly larger than the deviations of the Just-Jahreiß model from the NGP data of SDSS.

A comparison of the color-absolute magnitude diagrams of thick disk and halo with the observed fiducial isochrones of globular clusters (An et al. 2008) shows that the main sequences and the F-turnoff regimes of the stellar evolution library are consistent in the g and r filters. However the giant branches show systematic deviations.

Since the parameter space is too large to find the absolute minimum $\langle\chi^2\rangle$ with TRILEGAL we determined the parameters for halo, thick disk, and thin disk sequentially by fitting reduced areas in the CMD.

Finally we found an optimized Set 5 with $\langle\chi^2\rangle = 1.33$. Typical deviations of model and data are still ~ 20 per cent. The parameters of this model are listed in the last column of Table 5.2.

The reason for the larger deviations is mainly the restricted choice for the thin and thick disk parameters and profile shapes.

The TRILEGAL code is a powerful tool to test Milky Way models against star count data. Especially the investigation of star number densities in the CMD (Hess diagrams) are very helpful to separate the effects of different stellar populations.

The TRILEGAL model offers complete parameter adjustments with a range of choices, allowing us to attempt to investigate the effects of the choice of parameters. Finally we obtain an improved input set (Set 5 in Chapter 5). Sets 1 to 4 have χ^2 values of comparisons with observations on Hess diagrams from 1.7 to 2.7. Set 5 has this value $\chi^2 = 1.33$ which adopts a sech^2 law as the density profiles of the thin and thick disks. The scale height of the oldest sub-population in the thin disk is $h_{\text{d,max}} = 459$ pc, the scale height of a single population of the thick disk is $h_t = 750$ pc, and the effective radius of stellar halo is $r_{\text{eff}} = 2.2$ kpc. The local surface density of thin and thick disks and local density of the halo is $50 \text{ M}_\odot\text{pc}^{-2}$, $4.2 \text{ M}_\odot\text{pc}^{-2}$, and $0.0001 \text{ M}_\odot\text{pc}^{-3}$ respectively.

We found a better input set for the TRILEGAL (Set 5), which is an optimization of the other input parameter sets. The TRILEGAL model can predict the star counts at any volume using the SDSS filter system. The relative differences in the Hess diagrams are larger than 20%. The optimization set shows the relative better Hess diagrams, which generate several large discrepancies

- The large over-densities redder than $g - r \sim 1.0$ are caused by the problem of stellar population synthesis.
- The large over-density located at $g - r \sim 0.3$ and $14.5 < g < 18$ mag is caused by the lack of the thick disk stars. But increasing thick disk stars cannot improve the general agreements in the Hess diagram. The structures of the disks are the main problem in the TRILEGAL model.
- The TRILEGAL generates excess stars in the turn-off of the halo because the density profile adopted by the TRILEGAL cannot match the SDSS data in the NGP field perfectly.

Although the relative differences between the SDSS data and the model are larger than 20%, the TRILEGAL model simulates the star counts simply and quickly. As the reference model, the TRILEGAL model is useful to generate the star count roughly.

In general, the luminosity functions of the TRILEGAL model match the SDSS data well. We can use the TRILEGAL model to predict the star counts of different apparent magnitudes.

8.2.3 The Besançon model

We plot the star counts in each band with contributions of three components and giants. The five globular clusters (M71 and M5 for the thick disk, M13, NGC 4147 and M92 for the halo) are adopted and overplotted as fiducial isochrones on CMDs of the model. The cluster with much lower metallicity than the one assumed in the model is expected cover the ridgeline of the CMD of the model. A significant shift of offset in u' is caused by a zero-point problem.

Hess diagrams of the four colors of the data, the model and their differences are plotted. In order to investigate the model features, three components along the vertical direction of the Galactic plane are plotted respectively also. The relative difference between data and the model is from -100% to $+100\%$ on each CMD. Except in $(u - g, g)$, the relative differences in regime of thin disk are less than 50% and ones in regime of thick disk are less than 70%.

The distribution of giants in the CMD is analyzed by the fraction of simulated giants and all stars via the Besançon model. We give the limit regions of the highest concentrations of giants on each CMD to estimate the quality of the Just & Jahreiß (2010) model, which ignores giants. Hess diagrams of giants and their relative number densities in the model are plotted in four colors. Two sub-populations (bluer sub-giants and redder giants) are most obvious in the CMDs. These giants' relative number densities in the total model are around 20% which should not be neglected. Meanwhile, regions without giants are identified on Hess diagrams where they can be simulated by only main sequence disks stars.

We are more concerned about the CMDs of the Besançon model using a variety of colors. This is the first time that the comparison between a Galactic model and the observation using four colors has been analyzed. The comparison of fiducial isochrones suggests that $u - g$ has large shift (~ 0.3 mag) in the CMDs which also causes a large discrepancy on the Hess diagram. The Besançon model reproduces $\sim 50\%$ discrepancies relative to SDSS observations in Hess diagrams of $g - r$, $r - i$, $i - z$. The worst simulations on Hess diagrams are located in the region of the halo population ($0.2 < g - r < 0.5$ and $g > 19$), turn-off ($g - r \sim 0.2$), and

bright-red end ($g - r > 1.1$ and $g < 15$). We select giants from the Besançon model simulating results to show their distribution on Hess diagrams. Two branches can be resolved and the relative density of giants in the model is less than 30% in the specific color ranges.

The luminosity functions of the Besançon models match the SDSS data in all color bands perfectly. The isochrones cannot be matched by the fiducial sequences of clusters with similar metallicities, the color $u - g$ especially. The relative differences of Hess diagrams are about 40%, which is much larger than the Hess diagrams simulated by the Just-Jahreiß and TRILEGAL models.

The luminosity functions cannot reflect the structures of the disks sensitively. The models should be tested by the Hess diagrams even though the luminosity functions of models match those of the data very well. The significant offsets of the MS of the Besançon model are demonstrated in this thesis, which may be caused by filter transformations, or the metallicities of disks. A set of simple profiles of the TRILEGAL model cannot obtain perfect Hess diagrams at the NGP field, which cannot be improved by optimized input parameters. Essentially, the vertical structures of the disks depend on the geometry of the profile law at the z direction.

8.2.4 The lower latitude fields

The Just-Jahreiß model is applied for the lower latitude fields with b between 60° and 80° . The best scale length pair of the thin and thick disks are determined by the NGP and 24 smaller lower fields with the half longitude width of 15° . The best fitted value is $(r_d, r_t) = (1.5, 2.8)$ kpc. The scale length of the thin disk is not reasonable. The upper boundaries of scale lengths are not significant therefore the $(1.5, 2.8)$ kpc are the bottom limits of the best scale lengths.

The relative differences between the data and the Just-Jahreiß model for the 24 small fields show the significant over-density around $l \sim 300^\circ$, which is the known Virgo stream or “12.4^h clump” in the halo. The Galactocentric distance of this clump is estimated to be about ~ 10 kpc.

The result is fixed to simulate five blocks below $b = 30^\circ$. The χ^2 values of the Hess diagrams in the ring fields are larger than in the NGP field. The reduced $\langle \ln \chi^2 \rangle$ values are between 2 and 3. The field with the smallest χ^2 is the Field 9, which points to the $(l, b) = (75^\circ, 240^\circ)$.

The same model is used to simulate the stripe blocks. The model can simulate the star counts in the five blocks below $b = 30^\circ$, the χ^2 values are larger an order of magnitude than in the NGP field. The Hess diagrams of the relative differences show that the worst disagreements are in the regimes dominated by the thin disk. These results imply that the star counts in the disks are the main sources of the discrepancies in the Hess diagrams. The red clumps of the thick disk located at the color range of $g - r \sim 0.6$ with absolute magnitude $M_g \sim 1.29$ mag are estimated to be at the height of ~ 2.6 kpc from the Galactic mid-plane.

The comparisons between the data and the model for the lower latitude fields prove that the Just-Jahreiß model can be used to find the substructures in the halo and the disks. The substructures with the densities higher or lower than the smoothing background are identified by the relative differences between the SDSS data and the simulated star counts. We are expecting to apply these comparisons to more directions.

8.3 Conclusion and Outlook

The TRILEGAL, Besançon, and Just-Jahreiß models were created in the last decade during the accumulation of observational data and the development of automated processing. The TRILEGAL and Besançon models have very good luminosity functions, which are match well with SDSS star counts. The luminosity function of the TRILEGAL model is not as good as the Besançon model but it is reasonable and credible. The isochrones of the thick and halo of the Besançon model are consistent with fiducial sequences determined by globular clusters except for an offset in the u band. This consistency exists in the TRILEGAL model also. In general, the two models can reproduce useful stellar populations in the case of isochrones and luminosity functions.

However Hess diagrams of the TRILEGAL and Besançon models have relative discrepancies larger than 30 per cent and even more. The adjustment and optimizing of input parameters cannot improve that problem on Hess diagrams. This fact suggests that the discrepant structures of the disks do not display the inconsistency on isochrones and luminosity functions. Structures of disks are insensitive to the sequences of MS stars and apparent magnitude distributions. The detailed structures only can be compared by Hess diagrams.

Some more progress may be possible by varying the thin disk parameters further, but the main differences are of a structural nature. In TRILEGAL, the range of input parameters and functions is quite restricted. More freedom for the SFH, for the vertical profile of the thin and thick disk and for the halo profile would be desirable when simulating high Galactic latitude data. Additionally the comparison with fiducial star cluster isochrones has shown the an improvement of the late stages in stellar evolution in the $ugriz$ filter system is desirable.

The launch of Gaia will bring us a more powerful tool to normalize local stellar distribution and to obtain more significant stellar kinematics data. Based on the kinematics data and local normalization, the Just-Jahreiß model have an opportunity to make improvements in the near future. And the contributions of the giants should be researched further which could improve the minor discrepancy in Hess diagrams. The transition between thin and thick disks of the Just-Jahreiß model implies that we need a much steeper profile at the oldest sub-population of the thin disk.

The scale lengths and asymmetries of the thin and thick disks require more and lower fields. Besides the larger ring fields and the stripe 110 we tested, more fields should be considered to compare with the SDSS data. We still do not have credible extinction and reddening laws for the fields below $b = 30^\circ$. The improvements based on the different directions will be done in the future. The TRILEGAL and Besançon models will be compared with the SDSS data for the low latitude fields to reveal more details of the structures of disks.

The discrepancies in the Hess diagrams due to giants in the disks are expected to require deeper study. The contributions of giants are simulated by the Besançon model and are identified in the Hess diagrams, which are our basis and reference for the inclusion of giants in the Just-Jahreiß model.

Bibliography

- Abadi, M. G., Navarro, J. F., Steinmetz, M., & Eke, V. R. 2003, *ApJ*, 597, 21
- Abazajian, K. N., Adelman-McCarthy, J. K., Agüeros, M. A., et al. 2009, *ApJS*, 182, 543
- Adelman-McCarthy, J. K., Agüeros, M. A., Allam, S. S., et al. 2008, *ApJS*, 175, 297
- Aihara, H., Allende Prieto, C., An, D., et al. 2011, *ApJS*, 193, 29
- Allard, F., Hauschildt, P. H., Alexander, D. R., Ferguson, J. W., & Tamanai, A. 2000, in *Astronomical Society of the Pacific Conference Series*, Vol. 212, *From Giant Planets to Cool Stars*, ed. C. A. Griffith & M. S. Marley, 127
- Allende Prieto, C., Sivarani, T., Beers, T. C., et al. 2008, *AJ*, 136, 2070
- An, D., Johnson, J. A., Clem, J. L., et al. 2008, *ApJS*, 179, 326
- An, D., Pinsonneault, M. H., Masseron, T., et al. 2009, *ApJ*, 700, 523
- Aumer, M. & Binney, J. J. 2009, *MNRAS*, 397, 1286
- Bahcall, J. N. 1984a, *ApJ*, 276, 169
- Bahcall, J. N. 1984b, *ApJ*, 276, 156
- Bahcall, J. N. & Soneira, R. M. 1980a, *ApJL*, 238, L17
- Bahcall, J. N. & Soneira, R. M. 1980b, *ApJS*, 44, 73
- Bahcall, J. N. & Soneira, R. M. 1984, *ApJS*, 55, 67
- Bailer-Jones, C. A. L. 2009, in *IAU Symposium*, Vol. 254, *IAU Symposium*, ed. J. Andersen, J. Bland-Hawthorn, & B. Nordström, 475–482
- Bensby, T., Zenn, A. R., Oey, M. S., & Feltzing, S. 2007, *ApJL*, 663, L13
- Bertelli, G., Bressan, A., Chiosi, C., Fagotto, F., & Nasi, E. 1994, *A&AS*, 106, 275
- Bessell, M. S., Castelli, F., & Plez, B. 1998, *A&A*, 333, 231
- Bok, B. J. 1956, *AJ*, 61, 309
- Bok, B. J. & Connolly, J. K. 1954, *AJ*, 59, 384
- Caldwell, J. A. R. & Ostriker, J. P. 1981, *ApJ*, 251, 61
- Castelli, F., Gratton, R. G., & Kurucz, R. L. 1997, *A&A*, 318, 841
- Chabrier, G. 2001, *ApJ*, 554, 1274
- Chabrier, G., Baraffe, I., Allard, F., & Hauschildt, P. 2000, *ApJ*, 542, 464

- Chen, A. B.-C., Lu, P. K., Méndez, R. A., & van Altena, W. F. 2003, *AJ*, 126, 762
- Chonis, T. S. & Gaskell, C. M. 2008, *AJ*, 135, 264
- Chu, Y. & Zhao, Y.-H. 1998, in *IAU Symposium*, Vol. 179, *New Horizons from Multi-Wavelength Sky Surveys*, ed. B. J. McLean, D. A. Golombek, J. J. E. Hayes, & H. E. Payne, 131
- Clem, J. L., Vanden Berg, D. A., & Stetson, P. B. 2008, *AJ*, 135, 682
- Correnti, M., Bellazzini, M., & Ferraro, F. R. 2009, *MNRAS*, 397, L26
- de Vaucouleurs, G. 1948, *Annales d'Astrophysique*, 11, 247
- Dehnen, W. & Binney, J. 1998, *MNRAS*, 294, 429
- Dierickx, M., Klement, R., Rix, H.-W., & Liu, C. 2010, *ApJL*, 725, L186
- Duffau, S., Zinn, R., Vivas, A. K., et al. 2006, *ApJL*, 636, 97
- Eggen, O. J., Lynden-Bell, D., & Sandage, A. R. 1962, *ApJ*, 136, 748
- Einasto, J. 1979, in *IAU Symposium*, Vol. 84, *The Large-Scale Characteristics of the Galaxy*, ed. W. B. Burton, 451–458
- Finley, D. S., Koester, D., & Basri, G. 1997, *ApJ*, 488, 375
- Fioc, M. & Rocca-Volmerange, B. 1997, *A&A*, 326, 950
- Fioc, M. & Rocca-Volmerange, B. 1999, *ArXiv Astrophysics e-prints*, arXiv:astro-ph/9912179
- Fluks, M. A., Plez, B., The, P. S., et al. 1994, *A&AS*, 105, 311
- Fuhrmann, K. 2008, *MNRAS*, 384, 173
- Gao, S., Jiang, B.-W., & Zhao, Y.-H. 2007, *ChJAA*, 7, 111
- Gao, S., Just, A., & Grebel, E. 2011, *A&A*
- Gilmore, G. 1984, *MNRAS*, 207, 223
- Gilmore, G. & Reid, N. 1983, *MNRAS*, 202, 1025
- Gilmore, G., Wyse, R. F. G., & Jones, J. B. 1995, *AJ*, 109, 1095
- Gilmore, G. F., de Boer, K. S., Favata, F., et al. 2000, in *Society of Photo-Optical Instrumentation Engineers (SPIE) Conference Series*, Vol. 4013, *Society of Photo-Optical Instrumentation Engineers (SPIE) Conference Series*, ed. J. B. Breckinridge & P. Jakobsen, 453–472
- Girardi, L. 1996, PhD thesis, , Universidade Federal do Rio Grande do Sul, Porto Alegre, Brazil, (1996)

- Girardi, L., Bertelli, G., Bressan, A., et al. 2002, *A&A*, 391, 195
- Girardi, L., Grebel, E. K., Odenkirchen, M., & Chiosi, C. 2004, *A&A*, 422, 205
- Girardi, L., Groenewegen, M. A. T., Hatziminaoglou, E., & da Costa, L. 2005, *A&A*, 436, 895
- Gliese, W. 1988, *Stand. Star Newsl.* 13, 13, 13, 13
- Groenewegen, M. A. T. 2008, *A&A*, 488, 935
- Groenewegen, M. A. T., Girardi, L., Hatziminaoglou, E., et al. 2002, *A&A*, 392, 741
- Gunn, J. E., Carr, M., Rockosi, C., et al. 1998, *AJ*, 116, 3040
- Gustafsson, B., Edvardsson, B., Eriksson, K., et al. 2008, *A&A*, 486, 951
- Hall, P. B., Osmer, P. S., Green, R. F., Porter, A. C., & Warren, S. J. 1996, *ApJS*, 104, 185
- Harris, W. E. 1996, *AJ*, 112, 1487
- Hauschildt, P. H., Allard, F., & Baron, E. 1999, *ApJ*, 512, 377
- Hess, R. 1924, in *Probleme der Astronomie. Festschrift für Hugo v. Seeliger.* (Berlin: Springer), 265
- Ibukiyama, A. & Arimoto, N. 2002, *A&A*, 394, 927
- Ivezić, Ž., Sesar, B., Jurić, M., et al. 2008, *ApJ*, 684, 287
- Jahreiß, H. & Wielen, R. 1997, in *ESA Special Publication, Vol. 402, Hipparcos - Venice '97*, 675–680
- Jordan, S. 2008, *Astronomische Nachrichten*, 329, 875
- Jordi, K., Grebel, E. K., & Ammon, K. 2006, *A&A*, 460, 339
- Jurić, M., Ivezić, Ž., Brooks, A., et al. 2008, *ApJ*, 673, 864
- Just, A., Gao, S., & Vidrih, S. 2011, *MNRAS*, 411, 2586
- Just, A. & Jahreiß, H. 2008, *Astronomische Nachrichten*, 329, 790
- Just, A. & Jahreiß, H. 2010, *MNRAS*, 402, 461
- Kaiser, N. & Pan-STARRS Team. 2002, in *Bulletin of the American Astronomical Society*, Vol. 34, American Astronomical Society Meeting Abstracts, 122.07
- Kapteyn, J. C. & van Rhijn, P. J. 1920, *ApJ*, 52, 23
- Kapteyn, J. C. & van Rhijn, P. J. 1922, *ApJ*, 55, 242

- Kroupa, P. 2001, *MNRAS*, 322, 231
- Kuijken, K. & Gilmore, G. 1989, *MNRAS*, 239, 651
- Kurucz, R. L. 1992, in *IAU Symposium*, Vol. 149, *The Stellar Populations of Galaxies*, ed. B. Barbuy & A. Renzini, 225
- Larson, R. B. 1986, *MNRAS*, 218, 409
- Lee, Y. S., Beers, T. C., Allende Prieto, C., et al. 2011, *AJ*, 141, 90
- Lee, Y. S., Beers, T. C., Sivarani, T., et al. 2008a, *AJ*, 136, 2022
- Lee, Y. S., Beers, T. C., Sivarani, T., et al. 2008b, *AJ*, 136, 2050
- Lindgren, L. 2010, in *IAU Symposium*, Vol. 261, *IAU Symposium*, ed. S. A. Klioner, P. K. Seidelmann, & M. H. Soffel, 296–305
- Liu, C., Hu, J., Newberg, H., & Zhao, Y. 2008, *A&A*, 477, 139
- Lu, P. K., Mendez, R., van Altena, W., et al. 2000, in *Bulletin of the American Astronomical Society*, Vol. 32, *American Astronomical Society Meeting Abstracts #196*, 709
- Lupton, R., Gunn, J. E., Ivezić, Z., Knapp, G. R., & Kent, S. 2001, in *Astronomical Society of the Pacific Conference Series*, Vol. 238, *Astronomical Data Analysis Software and Systems X*, ed. F. R. Harnden Jr., F. A. Primini, & H. E. Payne, 269
- Mendez, R. A. 1995, PhD thesis, Yale University.
- Newberg, H. J., Yanny, B., Grebel, E. K., et al. 2004, in *Astronomical Society of the Pacific Conference Series*, Vol. 317, *Milky Way Surveys: The Structure and Evolution of our Galaxy*, ed. D. Clemens, R. Shah, & T. Brainerd, 264
- Newberg, H. J., Yanny, B., Rockosi, C., et al. 2002, *ApJ*, 569, 245
- Oort, J. H. 1932, *BAIN*, 6, 249
- Oort, J. H. 1952, *ApJ*, 116, 233
- Osmer, P. S., Kennefick, J. D., Hall, P. B., & Green, R. F. 1998, *ApJS*, 119, 189
- Prandoni, I., Wichmann, R., da Costa, L., et al. 1999, *A&A*, 345, 448
- Press, W. H., Teukolsky, S. A., Vetterling, W. T., & Flannery, B. P. 1992, *Numerical recipes in FORTRAN. The art of scientific computing* (Cambridge University Press)
- Robin, A. & Creze, M. 1986, *A&AS*, 64, 53
- Robin, A. C., Reyl  , C., Derri  re, S., & Picaud, S. 2003, *A&A*, 409, 523

- Rocha-Pinto, H. J., Maciel, W. J., Scalo, J., & Flynn, C. 2000, *A&A*, 358, 850
- Rodgers, C. T., Canterna, R., Smith, J. A., Pierce, M. J., & Tucker, D. L. 2006, *AJ*, 132, 989
- Roskar, R. 2010, PhD thesis, University of Washington
- Salpeter, E. E. 1955, *ApJ*, 121, 161
- Sarajedini, A. 1999, *AJ*, 118, 2321
- Schlegel, D. J., Finkbeiner, D. P., & Davis, M. 1998, *ApJ*, 500, 525
- Schmidt, M. 1956, *BAIN*, 13, 15
- Schönrich, R. & Binney, J. 2009, *MNRAS*, 399, 1145
- Schultheis, M., Robin, A. C., Reylé, C., et al. 2006, *A&A*, 447, 185
- Searle, L. & Zinn, R. 1978, *ApJ*, 225, 357
- Sesar, B., Jurić, M., & Ivezić, Ž. 2011, *ApJ*, 731, 4
- Sharma, S., Bland-Hawthorn, J., Johnston, K. V., & Binney, J. 2011, *ApJ*, 730, 3
- Siebert, A., Williams, M. E. K., Siviero, A., et al. 2011, *AJ*, 141, 187
- Sills, A., Pinsonneault, M. H., & Terndrup, D. M. 2000, *ApJ*, 534, 335
- Skrutskie, M. F., Cutri, R. M., Stiening, R., et al. 2006, *AJ*, 131, 1163
- Smith, M. C., Ruchti, G. R., Helmi, A., & Wyse, R. F. G. 2006, in *IAU Joint Discussion*, Vol. 13, IAU Joint Discussion
- Smolinski, J. P., Lee, Y. S., Beers, T. C., et al. 2011, *AJ*, 141, 89
- Steinmetz, M., Zwitter, T., Siebert, A., et al. 2006, *AJ*, 132, 1645
- Stoughton, C., Lupton, R. H., Bernardi, M., et al. 2002, *AJ*, 123, 485
- Tucker, D. L., Kent, S., Richmond, M. W., et al. 2006, *Astronomische Nachrichten*, 327, 821
- van der Kruit, P. C. & Freeman, K. C. 2011, *ArXiv e-prints*, arXiv:astro-ph/1101.1771
- Vazdekis, A., Sánchez-Blázquez, P., Falcón-Barroso, J., et al. 2010, in *IAU Symposium*, Vol. 262, IAU Symposium, ed. G. Bruzual & S. Charlot, 65–68
- Vivas, A. K., Zinn, R., Andrews, P., et al. 2001, *ApJL*, 554, L33
- Vyssotsky, A. N. 1963, *Spectral Surveys of K and M Dwarfs* (the University of Chicago Press), 192

Weinberg, M. D. 2004, in *Astronomical Society of the Pacific Conference Series*, Vol. 317, *Milky Way Surveys: The Structure and Evolution of our Galaxy*, ed. D. Clemens, R. Shah, & T. Brainerd, 129

Weinberg, S. 1977, *The first three minutes. A modern view of the origin of the universe* (Basic Books)

Wyse, R. F. G. & Gilmore, G. 1995, *AJ*, 110, 2771

York, D. G., Adelman, J., Anderson, Jr., J. E., et al. 2000, *AJ*, 120, 1579

Young, P. J. 1976, *AJ*, 81, 807

Zaggia, S., Hook, I., Mendez, R., et al. 1999, *A&AS*, 137, 75

Acknowledgements

I always keep on asking myself these two questions:

What is astronomy? What is an astronomer?

I am not sure I know answers of these questions. I learned a sentence from a German historian: *If you cannot see stars because the place you live in is not dark enough.* I believe that there is always something that we do not know, there is always something beyond our imaginations.

As a PhD student, I was sent to Germany by the Chinese government for the ongoing higher education program. I was lucky but I have to keep my mind on the knowledge that I did not grasp. The difficulty of the study (lack of knowledge and poor language) and an independent life, however, made me exhausted in the early years.

Even so, these days in Heidelberg are still the most important for me. I got new feelings, thoughts, knowledge and methods which will greatly help for a long period in the future. I have been familiar with the smell, personality, habits and virtues of Heidelberg. To Miss Heidelberg and the people I met here will be a necessity in my life.

I would like to appreciate Professor Eva K. Grebel, my supervisor, for her many suggestions and constant supports during my study. Without her help I would not be here for my doctoral program and life in Heidelberg. Her temperament and the effort are the definition to distinguished scientists. I am also thankful to Dr. Andreas Just for his guidance through the early years of chaos and confusion. His comprehensive knowledge on astronomy makes me always to keep deep thinking on specific issues. During this period I learned new contents from their points and work, which I used to think that they have been mastered. Prof. Grebel and Dr. Just are extremely careful to read and check my reports and papers. A lot of problems have been learnt and corrected.

Professor Biwei Jiang expressed her attention and interest in my work during these years. After my master degree study, she always looked forward to receiving the news of my progress. Meanwhile, we are expecting to work together in the future.

I should also mention that my graduate studies in Germany were supported by the China Scholarship Council (CSC). Dr. Xuan Liu (刘轩), Yang Zheng (郑阳) and unknown financial officers working at the Chinese General Consulate in Frankfurt are responsible for my living expenses and daily consultation in Germany. Be grateful for them together here.

Of course, I wish to thank the following: Mr. Zheng Huang (黄征), Dr. Shuo Li (李硕), Ms. Li Kong (孔丽), Ms. Hui Chen (陈辉), Ms. Wei Chen (陈伟) for their friendships during this beautiful time; Mr. Lei Liu (刘磊), Ms. Wenshan Wang (汪文姗), Ms. Jingsi Shi (史静思) for their supports and encouragements; Grebel's group (for their academic discussions); Within so many colleagues, Dr. Chao Liu (MPIA), Chentao Yang (BNU) and Hao Tian (BNU) shared me more than once their new ideas in a wide range of astronomical problems.

So many people provide more or less assistants to this work. Mr. Raoul Haschke and Mr. Johannes Ludwig help translate the abstract into German. Ms. Diana Schwalbe and Ms. Saskia Mayer help manage the funding for the academic travel. Dr. Peter Schwekendiek and Dr. Gernot Burkhardt help adjust the computers and printers many times.

My family always supports me to do everything that I like. They are thousands of miles away to worry about me. Finally, I am grateful to my wife Ms. Chun Li for her patience and *love*. Without her this work would never have come into existence.

I am afraid that someone who should be mentioned is missed in this page. Please forgive me and thank you.

Heidelberg
Shuang Gao
September 2, 2011